MOLECULES ROTATING IN ELECTRIC FIELDS BY QUANTUM AND SEMI-QUANTUM MECHANICS

A Dissertation

Presented to the Faculty of the Graduate School

of Cornell University

in Partial Fulfillment of the Requirements for the Degree of

Doctor of Philosophy

by

William W. Kennerly

August 2005

MOLECULES ROTATING IN ELECTRIC FIELDS BY QUANTUM AND SEMI-QUANTUM MECHANICS

William W. Kennerly, Ph.D.

Cornell University 2005

The quantum and semi-quantum mechanics of rigid molecules rotating in static electric and intense nonresonant laser fields have been studied. Basic quantum features including energy level correlation diagrams, eigenfunctions, alignment, orientation, and time-dependent wave functions propagated under pulsed fields are calculated. Energy level nearest neighbor spacing disributions are the primary semi-quantum approach, but Husimi distributions, periodic orbits, and monodromy diagrams are also investigated. We have elucidated these facets of the quantum-classical correspondence in this important rotational model, which is classically nonscaling with mixed phase space.

BIOGRAPHICAL SKETCH

William W. Kennerly was born in Philadelphia, Pennsylvania, in 1978. He first attended Penn Christian Academy (Norristown, Pennsylvania) and graduated salutatorian in 1992. He then transferred into the local public system to attend Plymouth-Whitemarsh High School, from which he graduated in 1996. He was admitted to Worcester Polytechnic Institute (Worcester, Massachusetts) as a chemistry major but spent much time in pure math and physics classes. He won awards for analytical chemistry research and mathematical modeling in the COMAP competition. He graduated with a B.S. in Chemistry, with distinction, in 2000. He immediately entered the Ph.D. program in the Department of Chemistry and Chemical Biology at Cornell University (Ithaca, New York) and soon started working with Greg Ezra to obtain fundamental understanding of quantum mechanics. After two years of teaching introductory chemistry, he won the departmental teaching assistant award. Later that year he helped persuade the Cornell graduate student body to not unionize. He earned the M.S. degree at the end of 2002 and finished his Ph.D. research in the summer of 2005. He then moved to Albany, New York, to pursue further opportunities.

Kennerly enjoys backpacking and bowling. In the spring of 2005, he was captain of the Alpha Chi Sigma bowling team, and they did not occupy last place in the league.

ACKNOWLEDGEMENTS

It is a pleasure to acknowledge the enduring patience of Greg Ezra, who has explained group theory to me many times, among other mathematical and physical topics. Also, Carlos Arango has been very helpful by providing results corresponding to the present work but entirely within classical and semi-classical mechanics. Finally, Ben Widom and Paul Houston served well on my committee, making sure I knew something about avoided crossings and the supersonic nozzle (respectively).

The department of Chemistry and Chemical Biology has been a wonderful host, providing funding and a great research community.

TABLE OF CONTENTS

LIST OF FIGURES

LIST OF TABLES

Chapter 1

Elements of the Tilted Field Problem by Quantum Mechanics

Here the tilted fields problem, rigid rotating molecules in tilted static electric and intense nonresonant laser fields, is introduced. The Hamiltonian matrix elements are discussed, with lengthy derivations relegated to Appendix B. All modeling assumptions are stated.

1.1 Motivation

Chemists want to control molecules. Specifically, we study in detail how small molecules interact so we can manipulate chemical reactions at the molecular level. First we need to control single molecules. Then we can adjust collision parameters and carefully monitor the products. While all facets of molecular motion—vibrations, rotations, and translations—need to be understood, the present paper covers rotations only.

The simplest way one might try to control molecular rotation is with a static electric field, if the molecule has a permanent dipole. But at room temperature, the rotational state is a broad distribution of high angular momentum J states. Such quickly rotating molecules are impossible to control with an experimentally feasible static electric field. This simple fact stymied physical chemists until almost 1990, when a supersonic nozzle was first put into a static electric field. This creates a beam of molecules in *pendular states* at temperature near 1 K. [8] Loesch, [9] and separately Friedrich and Herschbach, [10] demonstrated this effect: *brute force*

orientation of molecular dipoles using strong static electric fields.

Several years later, Friedrich and Herschbach [11] developed a simple model of a molecule interacting with a nonresonant intense laser that explained an experiment from the literature, where carbon monoxide was aligned with the laser plane polarization axis. The model uses the inherent polarizability of any molecule coupled to the electric field component of the intense laser. This interaction is only capable of molecular alignment along the polarization axis, leaving the dipole to point either up or down the axis. Nevertheless, this study sparked a lot of work in molecular alignment. [12]

Then in 1999, Friedrich and Herschbach [4] predicted that combining a static electric field with an intense nonresonant laser permitted great improvement in orientation (the desired effect) with relatively weak static fields. The intense laser aligns the molecule along an axis, and the parallel static field picks a preferred orientation by preferentially stabilizing one axial direction over the other. Minemoto *et. al.* [13] observed this effect for OCS and HCl in 2003.

I have developed software that calculates all of the relevant quantities for combined static electric and intense nonresonant laser fields acting on a dipolar, polarizable molecule. In addition, my program models symmetric and asymmetric rotors in these fields, as well as linear rotors in these fields *tilted* at an arbitrary angle from each other.

Chapter 1 covers the various model Hamiltonians for these systems and all modeling assumptions are stated and justified. Relevant physical parameters are listed. The potential energy surfaces are illustrated and discussed. Finally, the Hamiltonian matrix structure is expounded. Chapter 2 shows correlation diagrams of energy, alignment, and orientation as the field parameters change. Also, wave

functions are plotted. They display the basic time-independent physics of the rotor-in-fields problems and are dutifully discussed. Chapter 3, on the other hand, is for quantum dynamics. Wave functions are propagated under the time-dependent Schrödinger equation simulating linear rotors in an intense nonresonant pulsed laser.

I have also implemented several semi-quantum techniques, which have had little role previously in analyzing rotational problems. Chapter 4 has level spacing distributions which use quantum energy level spacings to predict to what extent the corresponding classical phase space is chaotic. Chapter 5 shows off several conceptual items of the quantum-classical correspondence: monodromy, scarring periodic orbits, and Husimi phase space distributions.

1.2 Kinetic Energy

The rigid rotator kinetic energy is a staple in angular momentum textbooks, notably Zare. [14] Here we state the kinetic energy for linear, symmetric, and asymmetric rotors along with relevant quantum numbers.

Rotors are distinguished by their rotational constants A, B, C about three orthogonal axes (or equivalently by three moments of inertia, with $B = 1/2I_z$). The simplest case is a linear rotor, where one rotational constant is zero and the other two are equal and called B. The kinetic energy is simply

$$\text{linear rotor} \qquad T = B\boldsymbol{J}^2, \tag{1.1}$$

where $\boldsymbol{J}$ is angular momentum. In quantum theory, linear rotor eigenstates are specified by two good integer quantum numbers, J and M. Each energy eigenstate

is $2J+1$-fold degenerate and further delineated by the eigenvalue M:

$$\boldsymbol{J}^2 \left|JM\right\rangle = J(J+1)\hbar^2 \left|JM\right\rangle \qquad J = 0, 1, 2, \ldots$$
$$J_Z \left|JM\right\rangle = M\hbar \left|JM\right\rangle \qquad -J \leq M \leq +J.$$

The quantum number M is the lab frame Z component of angular momentum (in multiples of $\hbar$).

A symmetric rotor has two rotational constants equal and one other nonzero: if $A = B > C$ it is *prolate*; if $A > B = C$ it is *oblate*. The "extra" mass away from the symmetry axis adds a squared angular momentum component to the kinetic energy:

$$\text{prolate rotor} \qquad T = B\boldsymbol{J}^2 + (A-C)J_z^2 \tag{1.2a}$$
$$\text{oblate rotor} \qquad T = B\boldsymbol{J}^2 + (C-A)J_z^2. \tag{1.2b}$$

The z axis is a different molecular axis in each case. It is associated with A for the prolate rotor and with C for the oblate rotor; the distinguishable axis is singled out.

The symmetric rotor eigenstates have one additional quantum number over linear rotors, K:

$$J_z \left|JMK\right\rangle = K\hbar \left|JMK\right\rangle \qquad -J \leq K \leq +J. \tag{1.3}$$

The quantum number K is the molecular frame z component of angular momentum $\boldsymbol{J}$ (in multiples of $\hbar$).

Thus, for example, the energy of a free prolate symmetric rotor in the state $\left|JMK\right\rangle$ is $BJ(J+1) + (A-C)K^2$ (in multiples of $\hbar^2$). For given J and K, each energy is $2 \times (2J+1)$ degenerate: 2 for $\pm K$ degeneracy and $2J+1$ for the various M values.

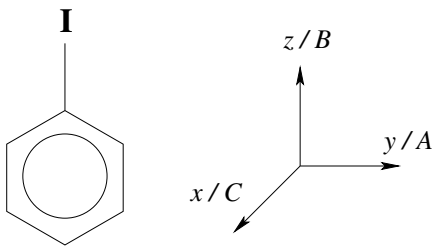

Figure 1.1: Asymmetric rotor iodobenzene with molecular frame definition and our unconventional assignment of rotational constants to the molecular axes.

Note that a linear rotor, by definition, cannot have any angular momentum about its (z) axis. Thus setting $K = 0$ for a symmetric rotor recovers exactly the linear rotor case.

Asymmetric rotors have three distinct rotational constants. The normal convention defines $A > B > C$ and sets the molecular frame with $ABC \leftrightarrow yzx$, associating the intermediate rotational constant B with the molecular z axis which best exhibits the asymmetry. However, we are foremost concerned with rotor electrical properties, and we define the dipole moment as the molecular z axis and B as the associated rotational constant. Likewise, y is the in-plane axis orthogonal to z, and y is associated with A; x is the out-of-plane axis associated with C.* Figure 1.1 illustrates the convention. Thus, for any asymmetric rotor, the dipole axis is defined as z and the association of molecular axes with rotational constants follows ($ABC \leftrightarrow yzx$). This does not necessarily reflect rotational constant asymmetry, since $A, B,$ or C may be the intermediate one.

All that being said, the kinetic energy of an asymmetric rotor is

$$T = AJ_y^2 + BJ_z^2 + CJ_x^2.$$

*This arrangement is possible only for sufficiently symmetric asymmetric rotors, such as those with C_{2v} symmetry. We only model such molecules. This is further discussed in Section 1.3, where our convention keeps the potential energy simplest.

With some simple algebra, the kinetic energy can be written

$$T = \frac{1}{2}(A+C)\boldsymbol{J}^2 + \frac{1}{2}(A-C)\left[J_y^2 + \kappa J_z^2 - J_x^2\right], \qquad \kappa = \frac{2B-(A+C)}{A-C}. \quad (1.4)$$

The asymmetry parameter is normally restricted to $|\kappa| \leq 1$, but our unusual rotational constant convention allows κ to take any value. Under both conventions, $\kappa = -1$ corresponds to a prolate symmetric rotor and $\kappa = +1$ an oblate symmetric rotor.[†]

1.3 Potential Energy

Classically, the potential energy of an electric dipole $\boldsymbol{d}$ in an electric field $\boldsymbol{E}$ is the projection of one vector onto the other, $-\boldsymbol{E}\cdot\boldsymbol{d}$. But an ideal permanent dipole does not accurately model a real molecule; the dipole itself is affected by electric fields. A better model includes a contribution proportional to the electric field in each direction. This is written as the proportionality constants $\boldsymbol{\alpha}$ contracted with the electric field, added to the permanent dipole moment $\boldsymbol{\mu}$:

$$\boldsymbol{d} = \boldsymbol{\mu} + \frac{1}{2}\boldsymbol{\alpha}\cdot\boldsymbol{E}. \quad (1.5)$$

The *polarizability tensor* $\boldsymbol{\alpha}$ determines how an electric field linearly induces dipole moments in the molecule. Nonlinear effects (hyperpolarizabilities) are ignored because they are very small compared to the linear response of the dipole for the fields and molecules we are modeling.[‡] Thus the potential energy is

$$V = -\boldsymbol{\mu}\cdot\boldsymbol{E} - \frac{1}{2}\boldsymbol{E}\cdot\boldsymbol{\alpha}\cdot\boldsymbol{E}. \quad (1.6)$$

[†]The symmetric top convention previously stated forbids $A = C$, so the asymmetry parameter is always defined.

[‡]The first hyperpolarizability coefficients are about 10^{-10} (mks units) of the polarizibility coefficients. Bogaard and Orr [15] provide background, some calculation notes, and applications to nonlinear optics.

The dipole moment and polarizability are a vector and tensor written in the molecular frame, while an external electric field is a vector in the lab frame. The molecule rotates relative to the lab frame, so to calculate the potential energy we must convert one cartesian frame to the other. *Euler angles* ϕ, θ, χ parameterize how a molecular frame xyz is rotated from a lab frame XYZ. We use the convention shared by Zare [14], Kroto [7], Brink and Satchler [16], and several other — but not all — authors. The transformation matrix that actively rotates lab fixed vectors to the angle parameterized by ϕ, θ, χ is

$$\mathsf{C} = \begin{pmatrix} \cos\phi\cos\theta\cos\chi - \sin\phi\sin\chi & -\sin\phi\cos\theta\cos\chi + \cos\phi\sin\chi & -\sin\theta\cos\chi \\ -\cos\phi\cos\theta\sin\chi - \sin\phi\cos\chi & -\sin\phi\cos\theta\sin\chi + \cos\phi\cos\chi & \sin\theta\sin\chi \\ \cos\phi\sin\theta & \sin\phi\sin\theta & \cos\theta \end{pmatrix} \tag{1.7}$$

where $\mathsf{C}_{iI} = \hat{f}_i \cdot \hat{\ell}_I$, $i \in x, y, z$, $I \in X, Y, Z$.

Mainly we use electric fields in one direction, either a static field or a plane polarized laser. Then the field direction is taken as $\hat{\ell}_Z$ and $\boldsymbol{E} = E\hat{\ell}_Z$.

Static electric field-permanent dipole potential energy

The molecular z axis labels the orientation of a rotating molecule, and we need to know how electric charge in the molecule is distributed with respect to this axis so we can write down the Hamiltonian. We always define the permanent dipole moment vector as the molecular z axis. A linear molecule's dipole moment is along the internuclear axis which is labeled z. Symmetric rotors have at least a third order rotation axis, which by symmetry must be the permanent dipole axis and is labeled z Asymmetric rotors, in general, can have permanent dipoles in any direction relative to any symmetry axis. However, sufficiently symmetric asymmetric molecules must have their permanent dipole moment aligned along

a symmetry axis, for example, the C_2 axis of the C_{2v} point group (water). We restrict our study to these cases, where the permanent dipole moment is $\boldsymbol{\mu} = \mu \hat{f}_z$.

When one of these simple molecules is in a static electric field, the model potential energy is proportional to $\hat{f}_z \cdot \hat{\ell}_Z = \mathsf{C}_{zZ}$, thus

$$\text{static electric field} \qquad V(\theta) = -\mu E_S \cos\theta. \tag{1.8}$$

Laser field-induced dipole potential energy

In addition to static electric fields we model molecules rotating in a laser beam. The laser is modeled classically, as an oscillating electric field in the lab-fixed Z direction $\boldsymbol{E_L}(t) = E_L \cos\omega t\, \hat{\ell}_Z$. But if we only use a very high frequency laser, then any permanent dipole could never be carried in phase with the oscillating field simply because it oscillates too quickly. The permanent dipole is anchored by heavy atoms and cannot respond. On average, there is no interaction of a permanent dipole with a high frequency oscillating field. However, an induced dipole created by the extremely fast response of electrons can be influenced by the high frequency field. The induced dipole then interacts with the laser field, practically instantaneously. This requires analyzing the molecular *polarizability.*[§] The results derived here can be found in the literature. [4, 5]

We disregard the orthogonal oscillating magnetic field since interaction with the magnetic dipole is negligible.

The potential energy of an induced dipole in a high frequency laser is $-\frac{1}{2}\boldsymbol{E_L} \cdot \boldsymbol{\alpha} \cdot \boldsymbol{E_L}$. The polarizability tensor is written in the molecular frame and has three nonzero elements on the diagonal. (This implicitly assumes the the frame which

[§]Near infrared light at 10^{14} Hz satisfies the high frequency condition, since molecules rotate with frequency 10^{10}–10^{12} Hz depending on the molecule and angular momentum state.

diagonalizes the inertial tensor and the polarizability tensor are the same. This is true for sufficiently symmetric molecules, such as C_{2v} asymmetric rotors and all symmetric rotors, and we will only model such molecules.) The polarizability tensor for an asymmetric rotor is thus $\hat{f}_x\alpha_{xx}\hat{f}_x + \hat{f}_y\alpha_{yy}\hat{f}_y + \hat{f}_z\alpha_{zz}\hat{f}_z$. Symmetric rotors must have $\alpha_{xx} = \alpha_{yy}$. Linear rotors are given the special notation $\alpha_{zz} = \alpha_\parallel$ for the polarizability parallel to the molecular axis, and $\alpha_{xx} = \alpha_{yy} = \alpha_\perp$ for the polarizability perpendicular to the molecular axis.

The laser-induced dipole potential energy for any type of rotor is found by a generic tensor calculation:

$$\begin{aligned} V &= -\frac{1}{2}\boldsymbol{E_L}\cdot\boldsymbol{\alpha}\cdot\boldsymbol{E_L} \\ &= -\frac{1}{2}(E_I\hat{\ell}_I)(\hat{f}_i\alpha_{ij}\hat{f}_j)(E_J\hat{\ell}_J) \\ &= -\frac{1}{2}E_IE_J\alpha_{ij}(\hat{\ell}_I\cdot\hat{f}_i)(\hat{f}_j\cdot\hat{\ell}_J) \\ &= -\frac{1}{2}E_IE_J\alpha_{ij}\mathsf{C}^T_{Ii}\mathsf{C}_{jJ} \\ &= -\frac{1}{2}E_IE_J\alpha_{ij}\mathsf{C}_{iI}\mathsf{C}_{jJ}. \end{aligned}$$

This nine term sum has six zero terms, since the electric field is parallel to the Z direction ($I = J = Z$ must hold in nonzero terms) and the polarizability tensor is diagonal ($i = j$ must hold in nonzero terms). Thus

$$\begin{aligned} V &= -\frac{1}{2}E_Z^2\alpha_{ii}\mathsf{C}_{iZ}^2 \\ V(\theta,\chi) &= -\frac{1}{2}E_Z^2\left[\alpha_{xx}\sin^2\theta\cos^2\chi + \alpha_{yy}\sin^2\theta\sin^2\chi + \alpha_{zz}\cos^2\theta\right]. \end{aligned}$$

As a brief aside, recall that the laser magnitude is time dependent since $E_Z^2 \equiv \boldsymbol{E}_L\cdot\boldsymbol{E}_L = E_L^2\cos^2\omega t$. We assumed that the laser frequency ω is very high compared to rotational frequency. The rotor does not feel the effect of the passing minima and maxima of the laser field cosine. The effective interaction is governed by the

square magnitude $\cos^2 \omega t$ averaged over one period, which is $1/2$. Thus $E_Z^2 = E_L^2/2$.

For the various rotors (linear, symmetric, asymmetric) the potential energy simplifies. Strategically adding and subtracting terms inside the parentheses provides

$$\begin{aligned} V &= -\frac{1}{4}E_L^2 \left[\sin^2\theta \left(\alpha_{xx}\cos^2\chi + \alpha_{yy}\sin^2\chi + \alpha_{xx}\sin^2\chi - \alpha_{xx}\sin^2\chi\right) + \alpha_{zz}\cos^2\theta\right] \\ &= -\frac{1}{4}E_L^2 \left[\sin^2\theta \left(\Delta\alpha^{yx}\sin^2\chi + \alpha_{xx}\right) + \alpha_{zz}\cos^2\theta\right] \\ &= -\frac{1}{4}E_L^2 \left[\Delta\alpha^{yx}\sin^2\theta\sin^2\chi + \alpha_{zz}\cos^2\theta + \alpha_{xx}\sin^2\theta + \alpha_{xx}\cos^2\theta - \alpha_{xx}\cos^2\theta\right] \\ &= -\frac{1}{4}E_L^2 \left[\Delta\alpha^{yx}\sin^2\theta\sin^2\chi + \Delta\alpha^{zx}\cos^2\theta + \alpha_{xx}\right] \end{aligned}$$

where the polarizability differences $\Delta\alpha^{zx} := \alpha_{zz} - \alpha_{xx}$ and $\Delta\alpha^{yx} := \alpha_{yy} - \alpha_{xx}$ are used. Of course, the constant term can be omitted, which leaves the final form of the potential energy of a molecule in a laser, within our modeling approximations:

$$V(\theta,\chi) = -\frac{1}{4}E_L^2 \left[\Delta\alpha^{yx}\sin^2\theta\sin^2\chi + \Delta\alpha^{zx}\cos^2\theta\right] \tag{1.9}$$

This is the least complicated form for asymmetric rotors. For symmetric and linear rotors, this simplifies more since $\alpha_{yy} = \alpha_{xx}$ leaving

$$\text{symmetric rotor} \qquad V(\theta) = -\frac{1}{4}E_L^2\Delta\alpha^{zx}\cos^2\theta \tag{1.10}$$

$$\text{linear rotor} \qquad V(\theta) = -\frac{1}{4}E_L^2\Delta\alpha\cos^2\theta \tag{1.11}$$

where conventially $\Delta\alpha := \alpha_\parallel - \alpha_\perp$ for a linear rotor. All the $\Delta\alpha$ parameters defined here are assumed positive, so that the laser-molecule interation is purely attractive. Certainly this is reasonable for linear molecules, as the electrons are distributed along the molecular axis, and a field applied in this direction shifts electrons towards other positively charged nuclei. A perpendicular field cannot as easily polarize the charge distribution off the molecular axis (away from all

nuclei), so $\alpha_\parallel > \alpha_\perp$ holds. However, $\Delta\alpha^{zx}, \Delta\alpha^{yx} > 0$ does not necessarily hold for all symmetric and asymmetric rotors, but we only model such molecules. For instance, iodobenzene satisifies this since iodine is highly polarizable, is on the z axis, and is not bonded to an atom off this axis.

Tilted, combined static and laser fields

When both static and laser fields are on and in the same direction, the potential energy is simply the sum of terms indicated above. However, we want to study the nonlinear dynamics of rotors in noncollinear fields, which we call *tilted* fields.

Some subtle effects are explicitly ignored. These include any dipole induced by the static field interacting with either field and the laser-induced dipole interacting with the static field. There are only two interactions: the permanent dipole with the static electric field, and the laser-induced dipole with the time-averaged laser field.

The new coordinate system uses the laser field polarization direction as the lab frame Z axis, so the induced dipole potential energy derived above remains valid. However, the static field is tilted away from $+Z$ by the *tilt angle* β in the XZ plane, in the $+X$ direction, so that $\boldsymbol{E_S} = E_S(\sin\beta, 0, \cos\beta)$ in the lab frame. Figure 1.2 illustrates tilted fields superimposed on the coordinate system. Previously we demanded the permanent dipole be parallel to $\hat{f}_z$, which in the lab frame is $(\mathsf{C}_{zX}, \mathsf{C}_{zY}, \mathsf{C}_{zZ})$ read from the bottom row of the direction cosine matrix (1.7). Thus the potential energy of the permanent dipole with the static field is

$$\begin{aligned} V(\theta,\phi) &= -\mu E_S(\sin\beta, 0, \cos\beta)\cdot(\cos\phi\sin\theta, \sin\phi\sin\theta, \cos\theta) \\ &= -\mu E_S(\sin\beta\sin\theta\cos\phi + \cos\beta\cos\theta). \end{aligned} \tag{1.12}$$

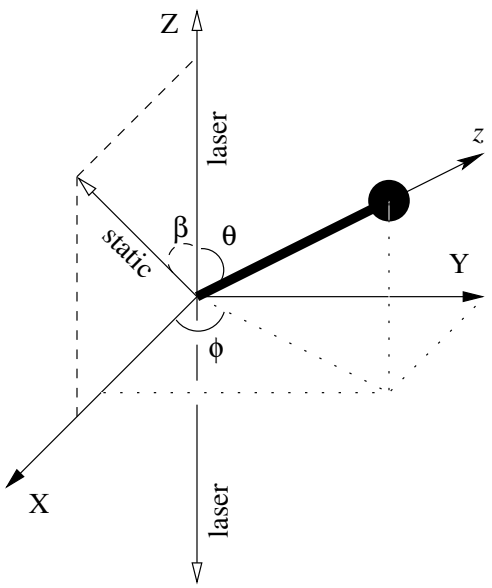

Figure 1.2: Coordinate system for linear rotor in tilted fields. Laser is parallel to lab fixed Z with static field tilted at angle β in the XZ plane. xyz is the molecular frame rotated by Euler angles ϕ, θ, χ from the lab frame XYZ.

The salient difference is the new variable ϕ, since the static field has a new component in the space fixed $+X$ direction.

1.4 Dimensionless Units and Practical Conversions

The experimental parameters used above need to be modified for two reasons. First, they are not used in practice. Experimentalists use different quantities, such as laser intensity instead of electric field amplitude. Second, the parameters are tied to a given experimental setup and specific molecule. Switching to dimensionless parameters allows many physically identical experiments to be modeled with one calculation. The dimensionless parameters will be related to the common experimental parameters.

Dimensionless parameters are obtained by dividing the entire Hamiltonian by

$B\hbar^2$. The quantum-mechanical squared angular momentum operator implicitly carries a $\hbar^2$ factor (its eigenvalues are $\hbar^2 J(J+1)$), so define $\boldsymbol{j}^2 := \boldsymbol{J}^2/\hbar^2$. Thus, a typical quantum Hamiltonian for a linear rotor in collinear static and laser fields, from Equations (1.8) and (1.11), is (still omitting the constant shift $\alpha_\perp$)

$$\begin{aligned} \hat{H} &= BJ^2 - \mu E_S \cos\theta - \frac{E_L^2 \Delta\alpha}{4} \cos^2\theta \\ \hat{h} &= j^2 - \omega \cos\theta - \Delta\omega \cos^2\theta \end{aligned} \tag{1.13}$$

with $\hat{h} := \hat{H}/B\hbar^2$, $\omega := \mu E_S/B\hbar^2$, and $\Delta\omega := E_L^2 \Delta\alpha/4B\hbar^2$. The dimensionless parameter ω sets the permanent dipole-static field interaction strength and likewise $\Delta\omega$ for the laser-induced dipole and laser field interaction strength. The Hamiltonian $\hat{h}$ is explicitly dimensionless.

The dimensionless constants are currently expressed in terms of experimental parameters in SI (mks) units, which experimentalists never use. For example, rather than amplitude of the laser field electric component E[N/C], they use laser field intensity I[W/cm^2]. The conversions are (recall that a N = J/m, a V = J/C, and a W = J/s):

$$\begin{aligned} B[\mathrm{cm}^{-1}] &= B[\mathrm{J}] \times \frac{1}{\mathrm{c}}[\mathrm{s/cm}] \times \frac{1}{\mathrm{h}}[1/(\mathrm{J{\cdot}s})] \\ \varepsilon_S[\mathrm{kV/cm}] &= E_S[\mathrm{N/C}] \times 10^{-2}[\mathrm{m/cm}] \times 10^{-3}[\mathrm{kV/V}] \\ \mu[\mathrm{D}] &= 2.999 \times 10^{29}[\mathrm{D}/(\mathrm{C{\cdot}m})] \times \mu[\mathrm{C{\cdot}m}] \\ \alpha[\mathrm{\AA}^3] &= \alpha[\mathrm{C^2{\cdot}m^2/J}] \times (1 \times 10^{10})^3[\mathrm{\AA}^3/\mathrm{m}^3] \times \frac{1}{4\pi\varepsilon_0}[\mathrm{J{\cdot}m/C^2}] \\ I_L[\mathrm{W/cm^2}] &= E_L^2[\mathrm{N^2/C^2}] \times \varepsilon_0[\mathrm{C^2/J{\cdot}m}] \times \frac{1}{2}\mathrm{c}[\mathrm{m/s}] \times 10^{-4}[\mathrm{m^2/cm^2}] \end{aligned}$$

Table 1.1: Physical and dimensionless parameters for linear molecules. Each datum is from the most recent one of [1, 2, 3]. Values in parentheses were copied from [4, Table 3]; other values from that reference have been independently verified (and slightly modified).

molecule	B [cm^{-1}]	μ [D]	$\Delta\alpha$ [Å^3]	ω [30 kV/cm]	$\Delta\omega$ [10^{12} W/cm^2]
CsF	0.1844	7.884	(3.0)	21.54	170
KCl	0.1286	10.269	(3.1)	40.22	250
ICl	0.1142	1.24	9.23	5.47	853.
DCl	5.449	(1.18)	2.13	0.109	4.12
DI	3.253	0.38	1.69	0.059	5.48
NO	1.672	0.159	1.28	0.0479	8.08
CO	1.931	0.10	(1.0)	0.026	5.5
N_2O	0.4190	0.161	2.27	0.194	57.2
OCS	0.2029	0.79	(4.1)	2.0	210
ClCN	0.1992	2.833	3.29	7.164	174.
ICN	0.1076	3.71	(7.)	17.4	700
HCN	1.478	2.985	2.00	1.017	14.3
HCCCl	0.1896	0.44	4.07	1.2	226.
HCCCN	0.1517	3.6	(6.0)	12.	420

which lead to these equations [4] for the dimensionless parameters:

$$\omega = 0.01679 \frac{\mu[\mathrm{D}]\varepsilon_S[\mathrm{kV/cm}]}{B[\mathrm{cm}^{-1}]}$$

$$\Delta\omega = 1.055 \times 10^{-11} \frac{I_L[\mathrm{W/cm}^2]\Delta\alpha[\mathrm{Å}^3]}{B[\mathrm{cm}^{-1}]}.$$

Parameter values for various linear molecules are listed in Table 1.1. Since asymmetric rotors have additional unique rotation constants and an extra polarizability parameter, the physical constants for iodobenzene and pyridazine are separately listed in Table 1.2. Typically for linear rotor calculations, we use $\omega = 30$ and $\Delta\omega = 120$ since these are realistic values, and their magnitudes and ratio $\omega/\Delta\omega = 1/4$ provide adequate well depth and asymmetric double well structure for complex behavior.

Table 1.2: Physical and dimensionless parameters for asymmetric rotors iodobenzene [5] and pyridazine. [6] The reduced rotational constants are $a = A/B$ and $c = C/B$.

molecule	A	B [cm^{-1}]	C	μ [D]	$\Delta\alpha^{zx}$ [Å^3]	$\Delta\alpha^{yx}$ [Å^3]
iodobenzene	0.0250	0.1891	0.0221	1.888	11.3	5.1
pyridazine	0.199	0.208	0.102	4.14	4.51	4.45

	a	c	ω [30 kV/cm]	$\Delta\omega^{zx}$ [10^{12} W/cm^2]	$\Delta\omega^{yx}$ [10^{12} W/cm^2]
iodobenzene	0.1323	0.1168	5.027	630.1	284.4
pyridazine	0.957	0.490	10.0	229.	226.

Polarizability data is difficult to find. The CRC Handbook [1] lists the average polarizability $\alpha = \frac{1}{3}\left(\alpha_\parallel + 2\alpha_\perp\right)$ for about fifty linear molecules (many with no permanent dipole). However, even this most recent source notes discrepencies between its references. Averaging polarizability dismisses its truly directional nature, so Herschbach [4] uses a rule of thumb for linear molecules (excepting diatomic hydrides): $\alpha_\parallel/\alpha_\perp = 2$, which implies $\Delta\alpha/\alpha = 0.75$.

Hirschfelder [3] lists the polarizability components for about fifteen molecules. He also lists components for *bond* polarizabilities and argues that $\alpha_\parallel$ and $\alpha_\perp$ can be well estimated by simply adding the individual bond data together. (Simple trigonometry is used for nonlinear molecules.) It is noted that this method does not work well when the molecule has "resonance structures." However, it seems this idea cannot be applied to diatomics, by either adding or averaging atomic polarizabilities to estimate molecular polarizability.

No comprehensive source for polarizability anisotropy data is available. However, if one needs data for a specific molecule, modern electronic structure software

Table 1.3: Hamiltonians of linear, symmetric, and asymmetric rotors in laser, static, and tilted fields with their symmetry groups. The full group is the direct product group of "lab frame"⊗"molecular frame" independent symmetry groups.

Hamiltonian		Lab Frame	Mol. Frame
free linear	$\boldsymbol{j}^2$	$SO(3)$	$D_{\infty h}$
+laser	$-\Delta\omega\cos^2\theta$	$D_{\infty h}$	$D_{\infty h}$
+static	$-\omega\cos\theta$	$C_{\infty v}$	$C_{\infty v}$
+tilted	$-\omega(\sin\beta\sin\theta\cos\phi+\cos\beta\cos\theta)$+laser	C_s	$C_{\infty v}$
free symmetric	$\boldsymbol{j}^2+(a-c)j_z^2$	$SO(3)$	$D_{\infty h}$
+laser	$-\Delta\omega^{zx}\cos^2\theta$	$D_{\infty h}$	$D_{\infty h}$
+static	$-\omega\cos\theta$	$C_{\infty v}$	$C_{\infty v}$
+tilted	(as linear)	C_s	$C_{\infty v}$
free asymmetric	$aj_y^2+j_z^2-cj_x^2$	$SO(3)$	D_2
+laser	$-\Delta\omega^{yx}\sin^2\theta\sin^2\chi-\Delta\omega^{zx}\cos^2\theta$	$D_{\infty h}$	D_2
+static	$-\omega\cos\theta$	$C_{\infty v}$	C_2
+tilted	(as linear)	C_s	C_2

can predict polarizability anisotropy. The user must be sufficiently skilled with these calculations to predict accurate values, however. It is not a trivial task.

1.5 Hamiltonian Symmetry

The Hamiltonians have now been derived and the dimensionless parameters defined. Table 1.3 displays all of the relevant Hamiltonians with corresponding symmetry. The symmetry is useful for understanding fully the wave function structure, determining which quantum numbers are "good" under different perturbation, and for defining symmetrized basis sets for each listed symmetry group that allow Hamiltonian matrix size reductions.

1.6 The Potential Energy Surface

The various potential energy surfaces are different, but they all share high field (low energy) and low field (high energy) limits. At low fields and high energy, the molecule is practically a free rigid rotor and has the corresponding energies and wave functions. At high fields and low energies, the system resembles a harmonic oscillator. The rotors-in-fields systems all have these analytically soluble limits.

Linear rotors

At intermediate field strengths, the potential energy surface is dominated by a double well in the polar angle θ.

For initial simplicity, assume the fields are parallel ($\beta = 0$). If the static field is off ($\omega = 0$) the PES is a symmetric double well of depth $\approx \Delta\omega$ and barrier centered at $\theta = \pi/2$. If the static field is on, the barrier shifts right to $\theta \approx \arccos(-\omega/2\Delta\omega)$ and one well deepens (left) as the other becomes shallow (right). If $\omega \gtrsim 2\Delta\omega$ then the system reverts to a single well between $\theta = 0$ and $\pi/2$. If the fields are antiparallel ($\beta = \pi$) then the stable and unstable wells are swapped in this discussion.

If $\Delta\omega = 0$ the PES is a cosinusoidal single well. Thus the double well potential disappears, and many interesting effects go with it; similarly if $\omega \gtrsim 2\Delta\omega$. Thus these regimes are not studied, except as limiting cases.

The above quantitative results are only approximate since they come from extremizing the potential energy $V(\theta) = -\omega\cos\theta - \Delta\omega\cos^2\theta$. Rather, the effective

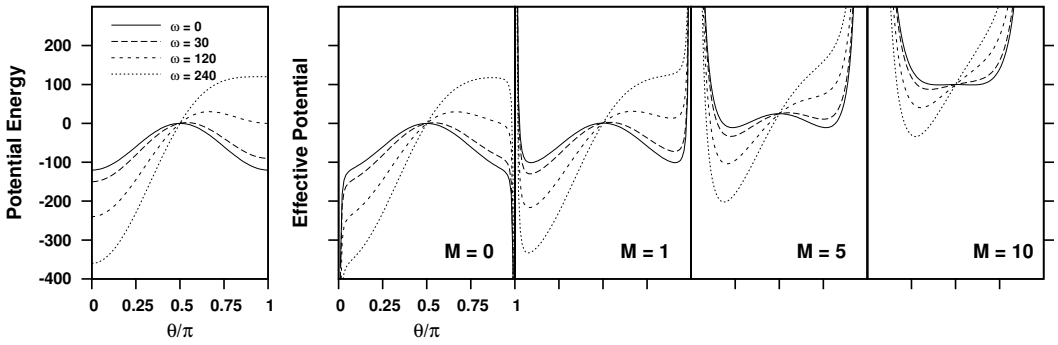

Figure 1.3: Comparison of V (left) and V_{eff} (right) for $M = 0, \Delta\omega = 120$ and several values of ω. Effective potential energy for other M is also shown.

potential¶

$$V_{\text{eff}}(\theta) = \frac{M^2 - \frac{1}{4}}{\sin^2\theta} - \frac{1}{4} + V(\theta) \tag{1.14}$$

should be extremized. This does not yield simple formulas for well depth and barrier position, while V does. However, V is a reasonable approximation to V_{eff} if M is small and θ is not near 0 and π. Figure 1.3 compares them at $M = 0$ for several parameter values. The effective potential energy introduces repulsive infinite barriers at $\theta = 0, \pi$ for $M > 0$ and infinite attractive wells if $M = 0$.

When the fields are tilted ($\beta \neq 0$), the system loses cylindrical symmetry, but the double well motif prevails. The system is still symmetric about the $\phi = \pi$ plane. The barrier becomes a potential energy peak centered near $\theta = \pi/2, \phi = \pi$ with strong shoulders still separating the θ wells. Figure 1.4 shows relevant pictures.

¶The "extra" 1/4 terms appear naturally when splitting out the ϕ dependence from the two DOF Schrödinger equation and absorbing the polar Jacobian $\sin\theta$ into the effective wave function. The classical effective potential is just $m^2/\sin^2\theta + V(\theta)$, leaving a qualitative difference between classical and quantum results for $M = 0$.

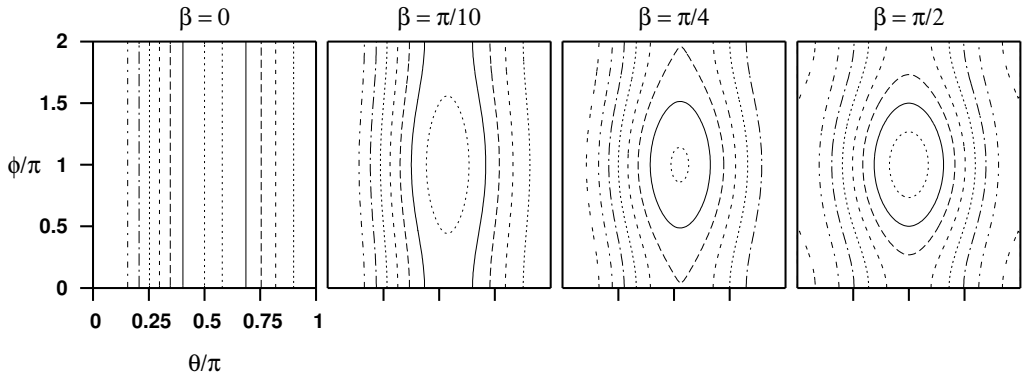

Figure 1.4: Tilted field potential energy contour plots (ϕ, θ plane) for $\omega = 30, \Delta\omega = 120$ and, from left to right, tilt angle $\beta = 0$, $\pi/10$, $\pi/4$, $\pi/2$.

Nonlinear rotors

The potential energy surface for symmetric rotors in fields is very similar to the linear rotor case. The asymmetric double well motif remains. Certainly, for $K = 0$ the symmetric rotor reduces to a linear rotor. The only difference between linear and symmetric rotors is a a new source of angular momentum which only affects the kinetic energy. Determining what conditions on M and K (good quantum numbers that appear in the effective potential) set up a single well versus a double well PES is more complicated.

Asymmetric rotors have three distinct polarizabilities in the molecule frame, rather than two for linear and symmetric rotors, and have a more complicated PES. For collinear fields, the potential energy function is

$$V(\theta, \chi) = -\omega \cos\theta - \Delta\omega^{zx} \cos^2\theta - \Delta\omega^{yx} \sin^2\theta \sin^2\chi.$$

Once again, the asymmetric double well picture reigns for $V(\theta, \chi)$ as illustrated in Figure 1.5. The well minima are at at the poles: $V(\theta = 0) = -\Delta\omega^{zx} - \omega$ and $V(\theta = \pi) = -\Delta\omega^{zx} + \omega$, much like the linear and symmetric rotors. Similiarly, the barrier

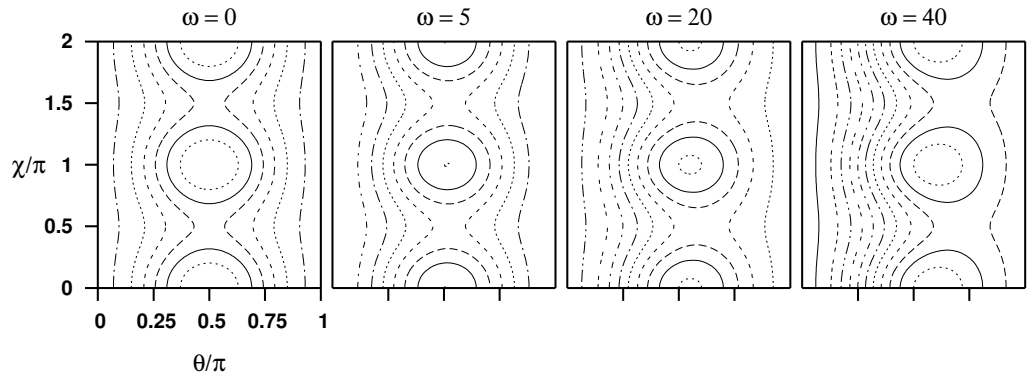

Figure 1.5: Potential energy surfaces for an asymmetric rotor in collinear fields $\Delta\omega^{zx} = 63$, $\Delta\omega^{yx} = 28.4$ (appropriate for iodobenzene) and $\omega = 0, 5, 20, 40$.

is near the equator $\theta = \pi/2$ (and shifts to the south pole as ω increases). However the χ dependence provides two isolated minima $V(\theta = \pi/2, \chi = \pi/2\text{or}3\pi/2) = -\Delta\omega^{yx}$ on the equator. Between these minima on the equator at $\theta = \pi, 2, \chi = 0, \pi$ are maxima. Of course, we have disregarding the effective potential energy dependence on M and K. As these increase, the low-lying PES structure is washed out in a complicated way described elsewhere. [17]

The extra polarizability term provides an extra handle for the nonresonant laser to attract the molecule. There is competition between the molecular z and y axes for alignment with the lab Z axis, and we expect decreased alignment.

1.7 The Hamiltonian Matrix

Apparently it is impossible to analytically solve Schrödinger's equation with any of these Hamiltonians. However, it easy to find a numerical solution by matrix diagonalization. This requires choosing basis functions for the matrix, calculating the matrix elements by evaluating the appropriate integrals, and using a standard ma-

trix diagonalization routine (`rsm` in EISPACK) to calculate eigenvalues (quantum energies) and eigenvectors (energy eigenstates).

Linear rotors

Spherical harmonics $Y_J^M(\theta, \phi) \equiv \langle \theta\, \phi | JM \rangle$ form a useful basis. First, they are the exact energy eigenstates in the field-free limit, so relatively few basis functions will be needed to get a good approximate wave function when fields are on. Second, spherical harmonics have a well known structure that can be used to construct the Hamiltonian matrix and related quantities.

The spherical harmonics have recurrence relations which allow explicit formulas for the several types of matrix elements we need. [18] The relevant properties are reviewed in Appendix A.1.

The matrix elements in the spherical harmonics basis are derived in Appendix B.1. A brief overview of their stucture is nevertheless useful here. The field free Hamiltonian $\boldsymbol{j}^2$ contributes only a diagonal element $J(J+1)$, meaning the kinetic energy operator only "connects" basis states with quantum number differences $\Delta J = 0$, $\Delta M = 0$. Each term in the Hamiltonian carries such *selection rules*. The static electric field (1.8) induces selection rules $\Delta J = \pm 1$, $\Delta M = 0$, which is familiar from the elementary perturbation theory approach to the Stark effect. The laser field (1.11) has selection rules $\Delta J = 0, \pm 2$, $\Delta M = 0$, which is reminiscient of the rotational Raman effect. Combined collinear fields have exactly the same selection rules, although the matrix is pentadiagonal. Lastly, when the fields are tilted (1.12) an azimuthal angle ϕ term is introduced causing M mixing. This term induces $\Delta J = \pm 1$, $\Delta M = \pm 1$ selection rules.

Nonlinear rotors

The symmetric top eigenstates $\langle \phi\, \theta\, \chi | JMK \rangle$ form the useful basis for symmetric and asymmetric tops in fields, for the same reasons spherical harmonics are used for linear rotors. The basis functions use the *Jacobi polynomials* (alternatively, the *reduced Wigner rotation matrix elements*), which have well-known structure described in Appendix A.3. The corresponding matrix elements are derived in Appendix B.3.

Briefly, the symmetric top kinetic energy is, of course, diagonal in this basis. There are three quantum numbers to consider, so the kinetic energy (1.2) selection rule is $\Delta J = 0$, $\Delta M = 0$, $\Delta K = 0$. Changes in K occur when the potential energy includes the Euler angle χ, which does not happen for symmetric tops, as seen in Table 1.3. Thus $\Delta K = 0$ holds for all symmetric top matrix elements. The static electric field has the selection rule $\Delta J = 0, \pm 1$ and the laser $\Delta J = 0, \pm 1, \pm 2$. When the fields are tilted, the same static field J selection rule applies but M is not strictly conserved; instead $\Delta M = \pm 1$.

The asymmetric rotor kinetic energy (1.4) is not diagonal in the symmetric top basis; the selection rule is $\Delta J = 0$, $\Delta K = 0, \pm 2$. The static field element is as for symmetric rotors, $\Delta J = 0, \pm 1$ with no change in M or K. But the laser field (1.9) now has an extra component $\sin^2\theta \sin^2\chi$ due to the completely anisotropic polarizability tensor, and this term induces changes in K. This term has selection rules $\Delta J = 0, \pm 1, \pm 2$, $\Delta K = 0, \pm 2$ while the $\cos^2\theta$ term sets $\Delta J = 0, \pm 1, \pm 2$, $\Delta K = 0$ as with symmetric tops. For tilted fields, since the static field-dipole configuration has not changed, the selection rule is still $\Delta J = 0, \pm 1$, $\Delta M = \pm 1$.

Just as a note, the asymmetric top kinetic energy separation (1.4) was historically done to allow efficient tabulation of asymmetric rotor energy levels [2, App.

IV]. We use it to separate the kinetic energy into easy and hard pieces. The easy piece is $\boldsymbol{j}^2$, which is diagonal in the symmetric top eigenstate basis. The hard part is $j_y^2 + \kappa j_z^2 - j_x^2$, which is not diagonal in the symmetric top eigenstate basis: $\Delta J = 0, \Delta K = 0, \pm 2$ is the selection rule.

In all cases the Hamiltonian matrix is real and symmetric. It does not have banded structure, but is very sparse due to the selection rules. The `rsm` ("real symmetric matrix") routine in EISPACK most efficiently diagonalizes such Hamiltonians.

Chapter 2

Correlation Diagrams and Wave Functions

2.1 Correlation Diagrams: Energy, Alignment, and Orientation

Correlation diagrams reveal basic properties of rotor states in various field configurations. For linear rotors in the fields discussed previously, the energy levels are functions of three dimensionless field parameters: static field strength ω, laser field intensity $\Delta\omega$, and mutual field tilt angle β. Mapping out the energy levels as these three parameters vary yields complicated structure; indeed, one needs only two parameters for the existence of "diabolical points" [19] where "accidental" degeneracies can occur in an energy spectrum. Of course, avoided crossings are rife, as usual when just one free parameter exists. Discovering the new structures found with three free parameters is a weighty task and not attempted here. However, several two dimensional slices of the four dimensional energy-parameter space are shown in this section.

Also, the alignment and orientation of eigenstates as functions of the field parameters show how well external fields restrict rotational motion. Alignment is $\langle\cos^2\theta\rangle$ and orientation is $\langle\cos\theta\rangle$ measured relative to the lab-fixed Z axis. The geometrical distinction is that alignment measures only how parallel the rotor and lab axes are on average, while orientation goes one step further and picks a preferred direction as would a compass needle. In our context, we expect high alignment and no orientation for a very intense laser and high alignment with high

orientation for a very strong static electric field.

Alignment and orientation in these correlation diagrams can be interpreted by the Hellmann-Feynman theorem. [20] As either field strength parameter is changed, the rate of energy level increase is equal to the average Hamiltonian derivative in that state:

$$\frac{\partial E_n}{\partial \omega} = \left\langle n \left| \frac{\partial \hat{h}}{\partial \omega} \right| n \right\rangle = -\left\langle n \left| \cos\theta \right| n \right\rangle$$
$$\frac{\partial E_n}{\partial \Delta\omega} = \left\langle n \left| \frac{\partial \hat{h}}{\partial \Delta\omega} \right| n \right\rangle = \left\langle n \left| \cos^2\theta \right| n \right\rangle \tag{2.1}$$

for dimensionless Hamiltonian (linear rotor in collinear fields) $\hat{h} = \boldsymbol{j}^2 - \omega\cos\theta - \Delta\omega\cos^2\theta$. Thus the energy correlation diagram curves can only decrease when laser intensity $\Delta\omega$ increases, and is dependent on the sign of $\langle n\,|\cos\theta|\,n\rangle$ in the n^{th} state when static field strength ω increases. The change in an energy correlation diagram is linked to the eigenstates' alignment and orientation behavior.

Linear rotors in collinear fields

As a first step, Figure 2.1 shows energy, alignment, and orientation correlation diagrams for $M = 0$ states as the static field strength ω increases from 0 to 30. In each panel, the heavy black line is the ground state and the various dashed lines correspond between the panels as the second, third, and so on energy states as seen at top.

On the left, the laser is turned off ($\Delta\omega = 0$). The energies evolve from the field-free eigenvalues $J(J+1)$ to the exact Stark eigenenergies. Note that as the Hellmann-Feynman theorem allows, the higher states initially increase in energy due to being localized on the unstable side of the potential energy surface ($\theta = \pi$). The lowest panel directly corresponds since the orientation of these states all tend

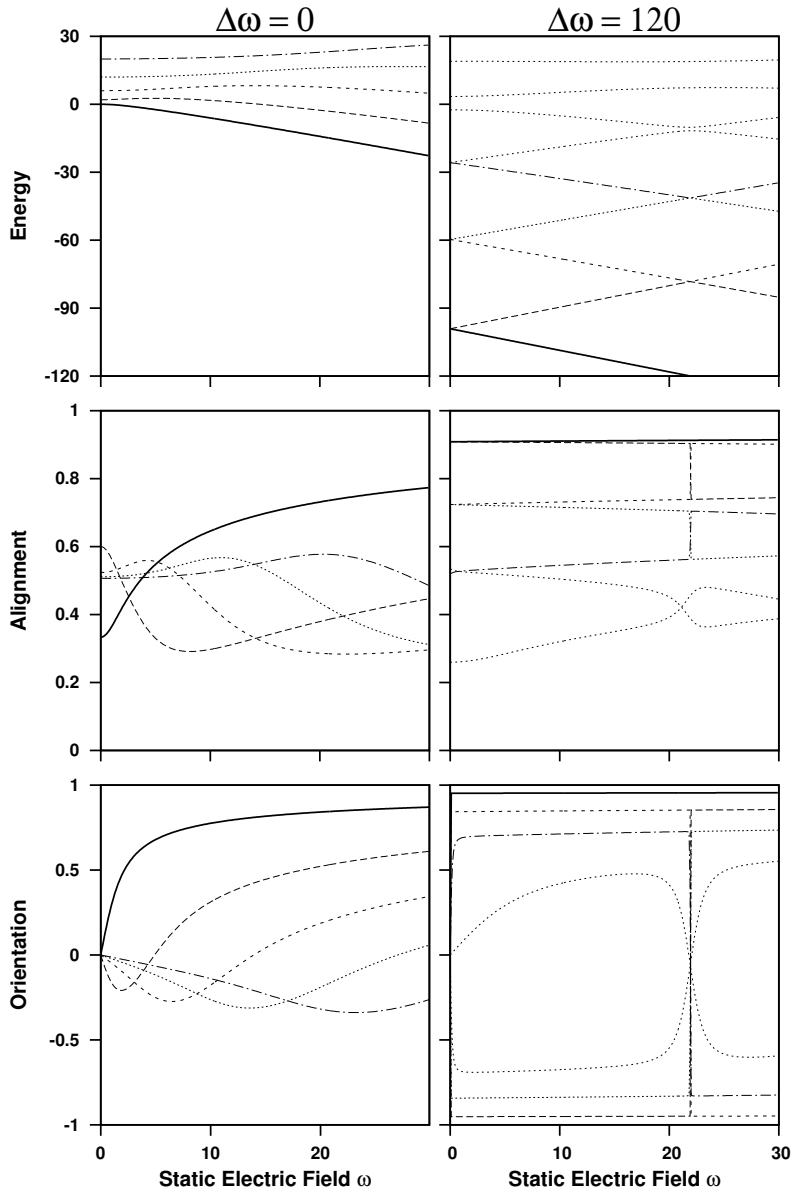

Figure 2.1: Energy (dimensionless), alignment $\langle \cos^2 \theta \rangle$, and orientation $\langle \cos \theta \rangle$ of a linear rotor in a (left) static electric field as $\omega = 0 \rightarrow 30$ and (right) collinear static and laser fields, with laser intensity fixed at $\Delta\omega = 120$ as $\omega = 0 \rightarrow 30$. Only $M = 0$ states are shown. The five lowest states are shown on each side, with four extra on the right which highlights a clear avoided crossing between the sixth and seventh. The ground state is marked with heavy line.

negative, indicating the dipole is oriented somewhat anti-parallel with the applied static field. However, as ω increases, the lower energy states get flipped around one by one and are trapped in the stable well. The ground state evolves monotonically, as it always will. The alignment correlation is not too interesting, except to note that the field-free eigenstates have alignment ($M = 0$) $1/3$ for $J = 0$, $3/5$ for $J = 1$, and approach $1/2$ from below as $J = 2, 3, 4, \ldots$. The alignment for field-free states is analytically given by the matrix element Equation (B.2c).

On the right of Figure 2.1, the laser intensity is moderately strong at $\Delta\omega = 120$ for various static field strengths. At $\omega = 0$, the low-energy rotor states appear to be doubly degenerate because the laser potential is a symmetric double well, which produces closely spaced pairs of levels with nearly identical probability distribution. As ω increases, these pairs split apart since one well is increasing in energy at the same magnitude the other well is decreasing in energy. At sufficiently high energy, near the laser potential barrier at zero energy, levels are no longer paired because the states are not bound.

At $\omega = 22$ the energy curves apparently cross. Actually the lower two pairs undergo sharply *avoided crossings*; the third pair clearly avoids crossing on this scale. The curves do not actually intersect as could be seen with more exact calculation around this point. The avoided crossing is manifested in the alignment and orientation correlations by sudden jumps. The two states involved in the avoiding crossing quickly exchange character, thus the alignment and orientation values exchange as well. The states in the clear avoided crossing undergo more gradual property exchange. Avoided crossings are discussed in more detail in Section 4.1.

Physically, the significant consequence of combining a strong laser field $\Delta\omega =$

120 with a weak static electric field $\omega = 1$ is that strong orientation occurs with a much weaker electric field than otherwise possible. Comparing the middle and bottom panels of Figure 2.1 reveals that the alignment and orientation for the lowest few states at right are much higher than any pure static field result shown at left. This effect was first theoretically proposed in 1999 [4] and experimentally verified in 2003. [13]

Figure 2.2 shows correlation diagrams as the laser intensity $\Delta\omega$ increases from 0 to 120. On the left, the static field is off ($\omega = 0$). The energy levels start at free rigid rotor energies $J(J+1)$ and then pair up as the laser intensity increases. The eventual degeneracies are the result of the deepening symmetric double well, which can bind more and more nearly degenerate pairs as $\Delta\omega \to \infty$. Usually one thinks the energy levels must repel, as with avoided crossings. But the selection rule for the laser-induced dipole interaction is $\Delta J = 0, \pm 2$ leaving no mechanism for the bottom two states (adiabatically correlated to field free $J = 0$ and $J = 1$) no way to couple and repel—that would require a $\Delta J = \pm 1$ matrix element. At high field, these adjacent even/odd pairs become almost identical, except for an additional node in the odd J member. Note that the energies are everywhere decreasing, as demanded by the Hellmann-Feynman theorem (2.1). The energy level pairing shows in the alignment diagram, as well. The orientation correlation is identically zero for all states since the symmetric double well does not favor a direction; either pointing up or down is equally well allowed leaving the average at zero.

The right side of Figure 2.2 shows the effect of a collinear static field $\omega = 30$ as the laser intensity $\Delta\omega$ increases $0 \to 120$. The pair structure from the left has been broken, but at even higher $\Delta\omega$ the static field will be overcome and the symmetric well reemerges. Three avoided crossings are clearly present, as seen in

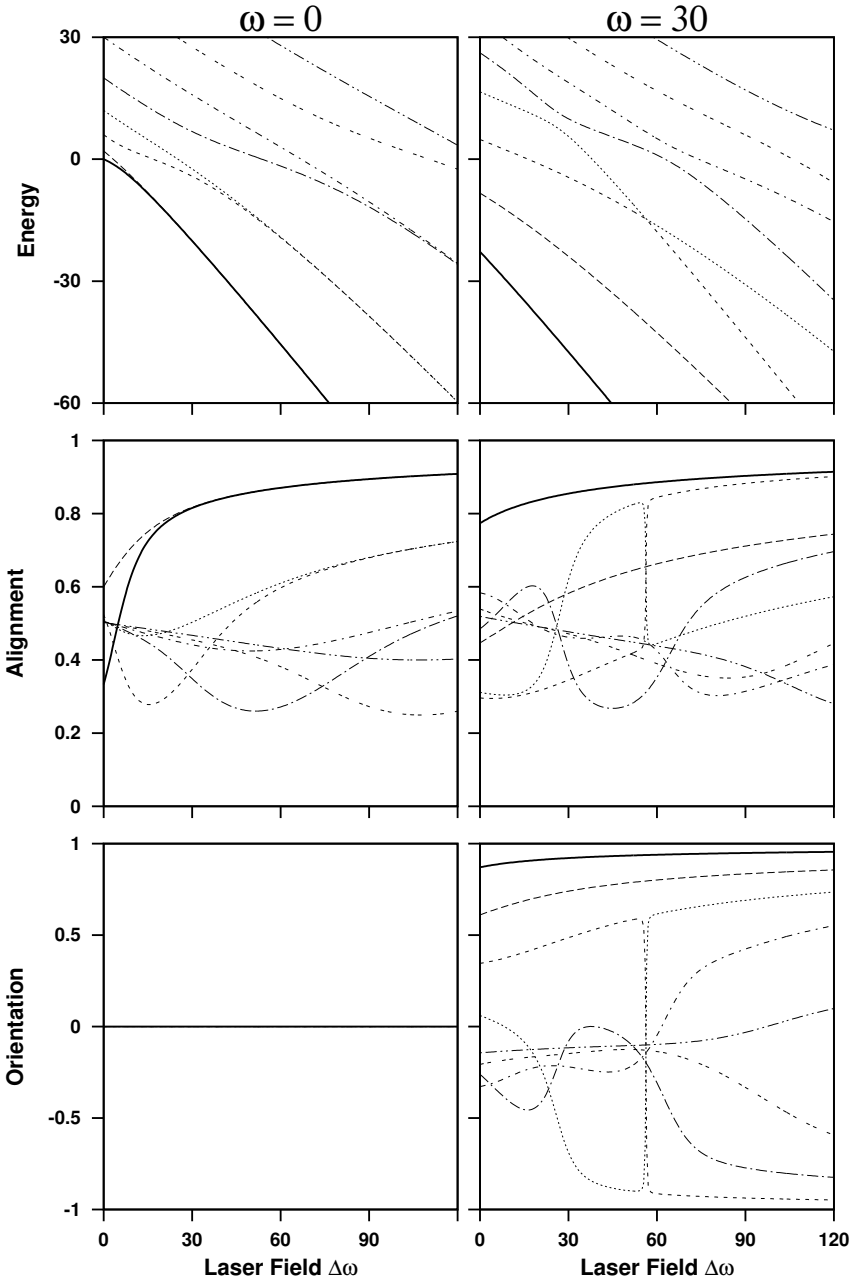

Figure 2.2: Energy (dimensionless), alignment, and orientation of a linear rotor in a (left) laser field as $\Delta\omega = 0 \rightarrow 120$ and (right) collinear static and laser fields, with static field strength fixed at $\omega = 30$ as $\Delta\omega = 0 \rightarrow 120$. The eight lowest $M = 0$ states are shown. The ground state is marked with heavy line.

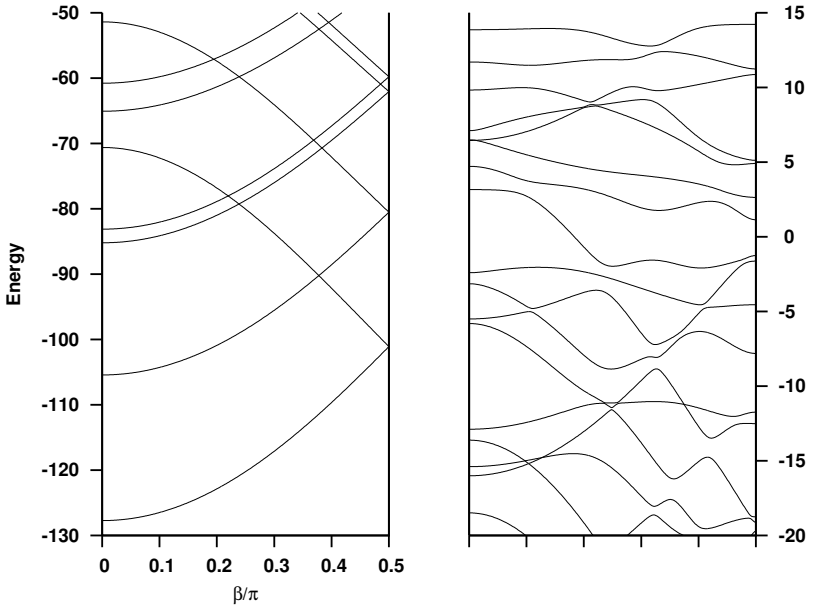

Figure 2.3: Energy correlation diagram with tilt angle β, tilting fields $\omega = 30$, $\Delta\omega = 120$ for parity= $+1$ linear rotor eigenstates. At left are the lowest eight states; at right about fifteen states at intermediate energies near barriers.

the alignment and orientation diagrams.

Linear rotors in tilted fields

Changing the tilt angle β between static and laser fields introduces many features, as seen in Figure 2.3 for $\omega = 30$ and $\Delta\omega = 120$. The lowest energy states on the left have simple structure. Several states are widely separated in collinear fields but pair up in perpendicular fields $\beta = \pi/2$. These two states have the same nodal structure but localized on opposite poles of the sphere. The states become almost degenerate as the tilting field brings the wells to the same depth $-\Delta\omega$. The states become closely split pairs, each state localized in both wells. The intermediate energy states on the right are qualitatively different. Here many of the avoided

crossings are widely avoided, instead of very closely avoided. There are even some regions where three states are interacting, suggesting the wave functions are very delocalized. Some states seem to pair up at $\beta = \pi/2$ and others do not. Such wild behavior will be linked to underlying classical chaotic dynamics in Chapter 4.

2.2 Wave Functions

Each energy eigenstate is calculated as a linear superposition of basis states; matrix diagonalization yields the superposition coefficients. Probability distribution pictures show where the wave function is localized and how many nodes it has. This requires calculating the basis functions over a coordinate grid, which is explained in Appendix A.1 for spherical harmonics and Appendix A.3 for symmetric top eigenstates.

Linear rotors

A physically significant quantity derived from the wave function is the reduced probability distribution. Given a wave function $\psi(\theta, \phi)$ the full probability distribution $\psi^*\psi \sin(\theta)$ is reduced by integrating out the (often trivial) ϕ dependence. The remaining function tells how the rotor is distributed in the polar angle θ irrespective of ϕ.

Figure 2.4 shows the twelve lowest $M = 0$ energy eigenstates for a linear rotor in collinear fields $\omega = 30$, $\Delta\omega = 120$. Clearly the ground state (Energy $= -127$) is strongly localized in the stable well. The next highest state (-85) is also in the stable well, but with one node. The third state (-71) is high enough to be localized in the higher lying well and has no nodes. The progression continues gaining additional nodes in states localized in alternating wells. Finally the eighth

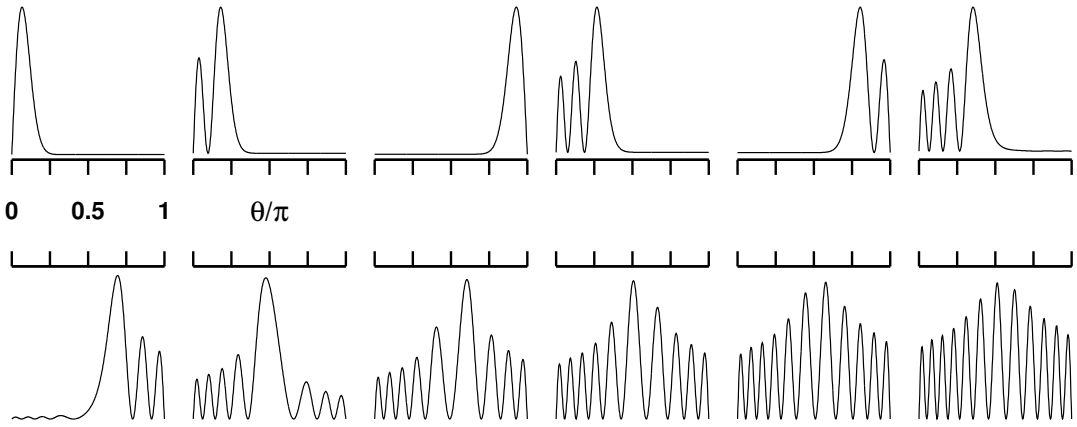

Figure 2.4: Reduced probability distributions v. θ of a linear rotor in collinear fields $\omega = 30$, $\Delta\omega = 120$, and $M = 0$. The twelve lowest energy eigenstates are shown, with ground state at top left and increasing energy to the right, and down.

state (Energy = +7) is above the barrier and freely rotates; it is delocalized over both wells. The higher states all have this behavior but gain one node for each step up.

When the fields are tilted, the wave function dependence on ϕ is no longer uniform. Figure 2.5 shows full probability distributions for several eigenstates in tilted fields $\omega = 30$, $\Delta\omega = 120$ as before but tilt angle $\beta = \pi/4$. The figure shows the distribution contours for the ground state (Energy = -120) the 28th state (+8) and the 47th state (+40) of the A' symmetry class.* The ground state is still very well oriented, despite only partial assistance from the static field. The middle state is just below the highest barrier, but above the low-lying barriers so some free rotation is evident. The highest state is well above the barrier and has regular nodal structure, indicating it is near the integrable field-free limit.

*Recall Table 1.3: the linear rotor in tilted fields Hamiltonian is conserved by reflection plane symmetry in the lab XZ plane, which supports the simple point group C_s. See Appendix B.2.

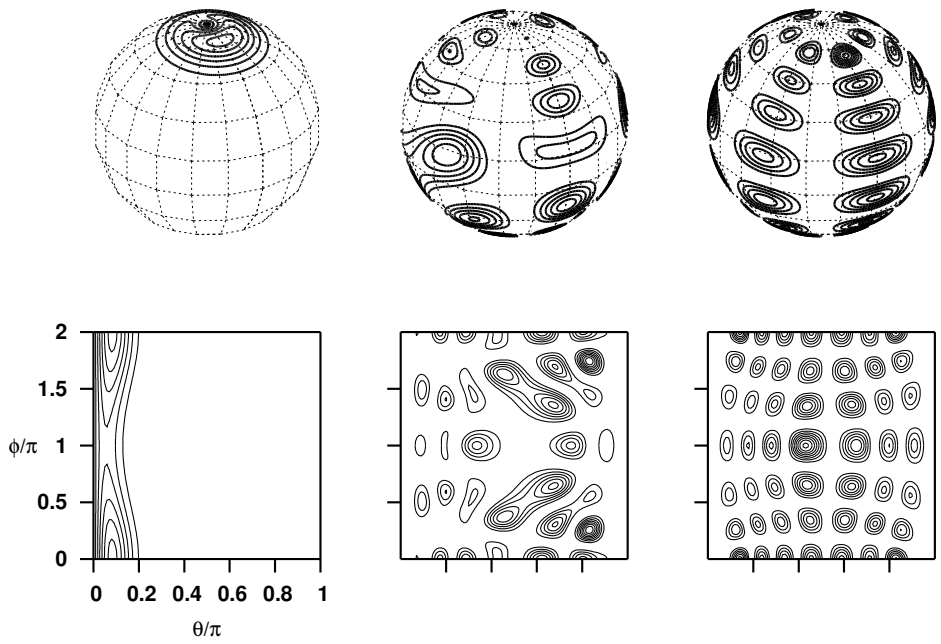

Figure 2.5: Probability distribution for three eigenstates of a linear rotor in tilted fields $\omega = 30$, $\Delta\omega = 120$, $\beta = \pi/4$. Ground, 28th and 47th eigenstates of A' symmetry. The bottom row shows the distribution contours projected on a rectangular (θ, ϕ) grid. The top row shows the distribution accurately represented on a spherical surface, with the viewier looking just to the left of the $\phi = 0$ vertical plane.

Note that the spherical wave function plots in the figure are most accurate but are cumbersome. They hide half of the distribution on the backside of the sphere. From now on the square grid pictures are used to show off the entire wave function.

Chapter 3

Quantum Propagation

The previous chapter covered static properties of rigid rotating molecules in various field types and configurations. But to take advantage of the enhanced orientation possible using collinear laser and static fields, a field-free system must first evolve to the desired pendular state. The details of how the free molecule enters the field can drastically change the final state, and in this chapter these details are elucidated.

First, results for static Hamiltonians are presented, showing how non-stationary states evolve under constant applied fields. Then the dynamics of rotors subject to pulsed laser fields, governed by the laser-induced dipole model used previously, are illustrated. This has become a popular proposal, with some experimental verification, for aligning molecules along a space-fixed axis without a field being present. This sub-field has recently been reviewed by Stapelfeldt and Seideman. [12]

The numerical integration algorithm is discussed in Appendix C. We use symplectic integration, which should help guard against long time instabilities, as explained in the appendix.

3.1 Preliminaries

We use the dimensionless time dependent Schrödinger equation (TDSE), formed as follows. Divide the TDSE

$$\mathrm{i}\hbar \frac{\mathrm{d}}{\mathrm{d}t} |\psi(t)\rangle = \hat{H}(t) |\psi(t)\rangle$$

by $B\hbar^2$, since this energy scale is present in all rotational Hamiltonians we use (Section 1.4), and use dimensionless time $\tau = B\hbar t$. The new variable τ roughly measures time in multiples of the $J = 1$ state field-free rotational period $T = \pi/B\hbar$.* The TDSE becomes

$$\mathrm{i}\,\frac{\mathrm{d}}{\mathrm{d}\tau}\,|\psi(\tau)\rangle = \hat{h}(\tau)\,|\psi(\tau)\rangle \tag{3.1}$$

using dimensionless Hamiltonian $\hat{h} = \hat{H}/B\hbar^2$.

As shown later, the rotational dynamics is governed by the field-free rotational period. Table 3.1 displays various rotational parameters of several linear rotors. Also shown is the dimensionless temperature at 1 K and 298 K, implying an average J value from a statistical mechanical calculation to determine the rotational period. The calculation is just the canonical average of J given the dimensionless temperature Y, over linear rotor eigenstates:

$$\langle J\rangle = \frac{1}{Q}\sum_{J=0}^{\infty} J(2J+1)\mathrm{e}^{-J(J+1)/Y} \tag{3.2}$$

with Q the canonical partition function and $J(J+1)$ the eigenenergies of the $(2J+1)$ degenerate eigenstates. The average angular momentum as a function of dimensionless temperature Y is plotted in Figure 3.1.

Here is how the dimensionless temperature and related parameters are calculated, considering units in detail. The basic parameters are

$$\begin{aligned}
\text{rotational temperature} \qquad & \theta_{\mathrm{rot}}[\mathrm{K}] = B[\mathrm{J}] \times \frac{1}{k}[\mathrm{K/J}] \\
\text{dimensionless temperature} \qquad & Y = k[\mathrm{J/K}] \times T[\mathrm{K}] \times \frac{1}{B}[1/\mathrm{J}] \\
\text{rotational period} \qquad & T_{\mathrm{rot}}[\mathrm{ps}] = \pi \times 10^{12}[\mathrm{ps/s}] \times \frac{1}{B}[\mathrm{J\,s^2}] \times \frac{1}{\hbar}[1/\mathrm{J\,s}] \times \frac{1}{J}[1]
\end{aligned}$$

*Rotational period: the classical Hamiltonian in action-angle variables (q_j, j) is $H = Bj^2$. By Hamilton's equation, $\dot{q}_j = 2Bj$. Since one rotational period is parameterized by $q_j = 0 \to 2\pi$ as $t = 0 \to T$, integrating yields $T = \pi/Bj$. In quantum terms, $T = \pi/B\hbar J$, where J is a dimensionless quantum number.

Table 3.1: Rotational constant B, rotational temperature $\theta_{\rm rot}$, dimensionless temperature Y and corresponding rotational period $T_{\rm rot}$ for several linear molecules. The latter two are linked since any given temperature fixes an average angular momentum, which affects the rotational period.

molecule.	B [cm^{-1}]	$\theta_{\rm rot}$ [K]	Y [1 K]	$T_{\rm rot}$ [ps, $J=1$]	Y [298 K]	$T_{\rm rot}$ [ps, $J=25$]
CsF	0.1844	0.2653	3.770	90.45	1123.	3.618
KCl	0.1286	0.1850	5.405	129.7	1611.	5.188
ICl	0.1142	0.1643	6.086	146.0	1814.	5.842
DCl	5.449	7.840	0.1276	3.061	38.01	0.1224
DI	3.253	4.680	0.2137	5.127	63.67	0.2051
NO	1.672	2.406	0.4157	9.975	123.9	0.3990
CO	1.931	2.778	0.3599	8.637	107.3	0.3455
N_2O	0.4190	0.6028	1.659	39.80	494.3	1.592
OCS	0.2029	0.2919	3.426	82.20	1021.	3.288
ClCN	0.1992	0.2866	3.490	83.73	1040.	3.349
ICN	0.1076	0.1548	6.460	155.0	1925.	6.200
HCN	1.478	2.127	0.4703	11.28	140.1	0.4514
HCCCl	0.1896	0.2728	3.666	87.97	1092.	3.519
HCCCN	0.1517	0.2183	4.582	109.9	1365.	4.398

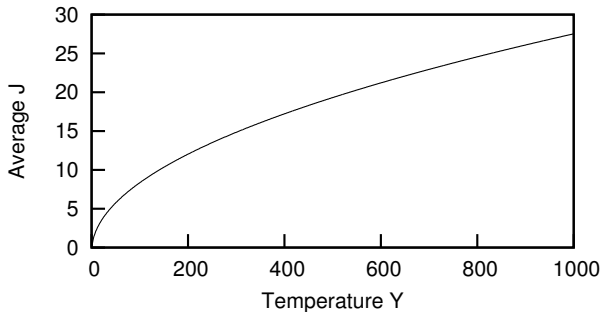

Figure 3.1: Average angular momentum quantum number $\langle J \rangle$ vs dimensionless temperature Y for a linear rotor, as determined by canonical statistical mechanics.

where J in the last formula is the dimensionless angular momentum quantum number, and k is Boltzmann's constant. The rotational constant B can usefully come in several different units. Typically it is given in wavenumbers [cm^{-1}], as in Table 3.1. But other useful dimensions are

$$B[1/\mathrm{J\,s}^2] = \frac{1}{2\pi} B[\mathrm{cm}^{-1}] \times c[\mathrm{cm/s}] \times \frac{1}{\hbar}[1/\mathrm{J\,s}]$$
$$B[\mathrm{J}] = 2\pi B[\mathrm{cm}^{-1}] \times c[\mathrm{cm/s}] \times \hbar[\mathrm{J\,s}].$$

The point is to figure out the rotational period for rotating molecules. The conditions of the experiments described here are typically around 1 K, which averaged over the molecules in Table 3.1 corresponds to $Y = 2.9$. Figure 3.1 links this Y to an average quantum number $\langle J \rangle = 1$, corresponding to rotational period $T_{\mathrm{rot}} = 69$ ps. For other temperatures, the rotational period is:

$$\begin{array}{rclcrclcrcl}
T & = & 1\ \mathrm{K} & \rightarrow & Y & = & 2.86 & \rightarrow & J & = & 1 & \rightarrow & T_{\mathrm{rot}} & = & 69\ \mathrm{ps} \\
T & = & 10\ \mathrm{K} & \rightarrow & Y & = & 28.6 & \rightarrow & J & = & 4 & \rightarrow & T_{\mathrm{rot}} & = & 17\ \mathrm{ps} \\
T & = & 100\ \mathrm{K} & \rightarrow & Y & = & 286 & \rightarrow & J & = & 14 & \rightarrow & T_{\mathrm{rot}} & = & 4.9\ \mathrm{ps} \\
T & = & 298\ \mathrm{K} & \rightarrow & Y & = & 854 & \rightarrow & J & = & 25 & \rightarrow & T_{\mathrm{rot}} & = & 2.8\ \mathrm{ps.}
\end{array}$$

3.2 Static Hamiltonian Propagation

The most basic calculation is propagating an initial state with a time-independent Hamiltonian. Figure 3.2 shows the interesting quantities. Here the spherically symmetric state $J = 0$ is propagated subject to static and laser fields at various tilt angles. Pictured, at two different laser intensities $\Delta\omega = 120$ and 500, are the autocorrelation function, alignment $\langle \cos^2\theta \rangle$, and orientation $\langle \cos\theta \rangle$.

Experimentalists are interested in high alignment and orientation, and the figure shows that simply raising the laser intensity is not enough to provide either.

Since the initial state is the isotropic extreme, the sudden application of intense fields only causes the evolving wave function to be a widely distributed superposition of field eigenstates, containing more above-barrier eigenstate spherical character than low-energy eigenstate aligned character. Thus the alignment is never high; it fluctuates around 0.6 for all tilt angles. This is the same as the most aligned field-free state, the $J = 1, M = 0$ spherical harmonic (p_z orbital); that is, not very aligned at all.

The orientation shown in Figure 3.2 is negligible. While all spherical harmonics have exactly zero orientation, the present propagation merely fluctuates around zero, never attaining useful orientation despite the high field strengths. (When $\beta = \pi/2$ the orientation is exactly zero by symmetry.)

Certainly alignment and orientation are improved by picking a different initial state. If the rotor started near the ground state of the full strength (time-independent) fields, then the alignment and orientation would be high and constant, since energy eigenstates are stationary.

3.3 Field-free Alignment

A booming application of the laser-induced dipole interaction is aligning molecules without a field present: they are hit with a laser pulse, and after the pulse leaves the molecules are well aligned at recurring times. The potential energy is

$$V(\theta, \tau) = -\Delta\omega \mathrm{e}^{-\tau^2/\sigma^2} \cos^2\theta,$$

the previously derived polarizability term multiplied by a gaussian time τ envelope of FWHM $\approx \frac{5}{3}\sigma$. One hopes to align molecules without an external field present, which would allow new experiments using rotationally restricted but electrically

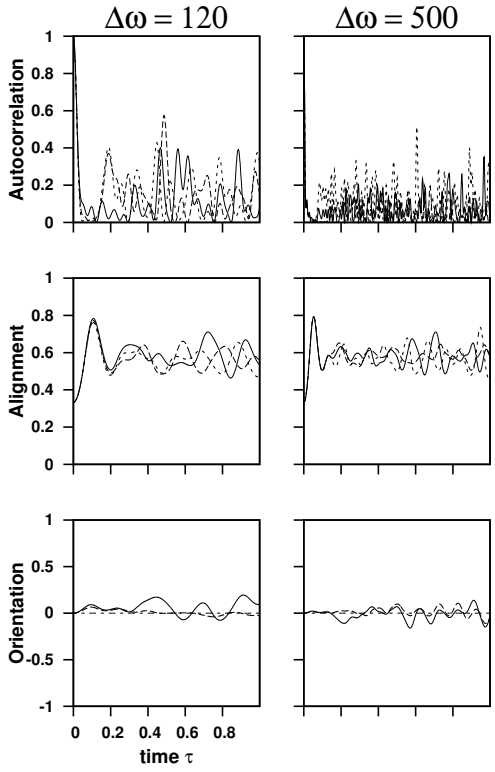

Figure 3.2: Time-independent Hamiltonian propagations, linear rotor in fields $\omega = 30$, (left) $\Delta\omega = 120$ and (right) 500 with tilt angle (solid) $\beta = 0$, (long dashes) $\pi/4$, and (short dashes) $\pi/2$. From top to bottom: autocorrelation function (initial state is $J = 0$ spherical harmonic, a s orbital), alignment $\langle\cos^2\theta\rangle$, and orientation $\langle\cos\theta\rangle$.

unperturbed molecules.

The key is that the alignment $\langle\cos^2\theta\rangle$ can change after the laser pulse has gone by, when the Hamiltonian has no potential energy term. This is, apparently, a purely quantum effect. The wavefunction $\psi(t)$ changes because each coefficient in the spherical harmonic superposition has a time-dependent phase:

$$|\psi(t)\rangle = \sum_J \mathrm{e}^{-\mathrm{i}J(J+1)\tau} c_J \, |JM\rangle \,. \qquad \text{(field free conditions)} \tag{3.3}$$

Here the autocorrelation function $|\langle\psi(0)|\psi(\tau)\rangle|^2$ is constant since the time dependent complex exponential phase factors cancel. But the alignment is still time

dependent, even after the pulse:

$$\left\langle \psi(t) \left| \cos^2\theta \right| \psi(t) \right\rangle = \sum_{J'J} \mathrm{e}^{\mathrm{i}[J'(J'+1)-J(J+1)]\tau} c^*_{J'} c_J \left\langle J'M' \left| \cos^2\theta \right| JM \right\rangle . \tag{3.4}$$

It turns out that the post-pulse alignment highly depends on the width σ and intensity $\Delta\omega$, as first discovered by Ortigoso *et. al.* [21] There are three distinct pulse regimes: nonadiabatic, intermediate, and adiabatic. Figure 3.3 shows the alignment of a linear rotor before, during and after various width pulses illustrating the full range of behavior.

The nonadiabatic regime ($\sigma \ll 1$) is marked by a pulse so fast relative to the rotational period that maximum alignment occurs *after* the pulse has gone by. The induced rotational wavepacket quickly oscillates and even attains greater alignment well after the pulse than the first maximum.

Using the analytic *sudden approximation* helps quantify what maximum width σ guarantees a non-adiabatic process. The sudden approximation posits a pulse so short that the lowest order propagator provides accurate results for post-pulse quantities. (See Appendix C.6.) Figure 3.4 compares the numerical propagation (as used to calculate all previous results) to the sudden approximation. The post-pulse autocorrelation function is shown for several short pulses. At $\sigma = 0.01$ the match is near-perfect. Width $\sigma = 0.03$ reveals a slight discrepancy at higher laser intensities. However, $\sigma = 0.05$ must be past the non-adiabatic limit since there are major differences between the methods at moderately high laser intensity.

The adiabatic regime ($\sigma \gg 1$) is marked by maximum alignment when the pulse is at maximum intensity. When the width is much greater than the rotational period, the pulse gently carries the field-free initial state to the instantaneous Hamiltonian eigenstate and back down to the initial state. There is little, if any, field-free alignment.

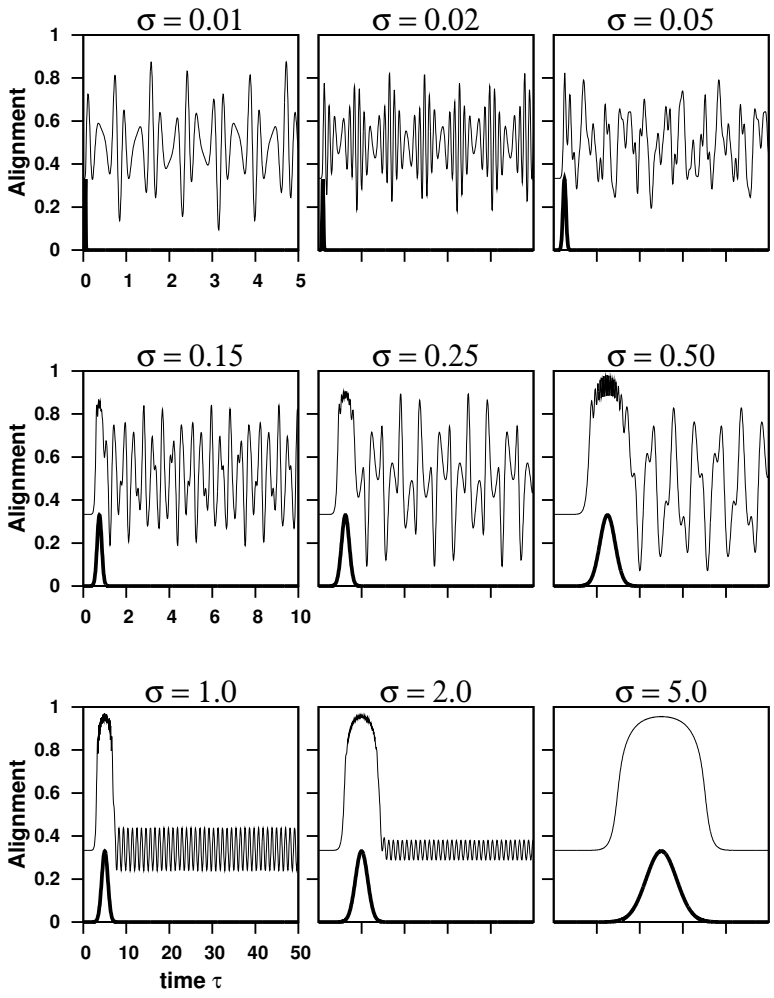

Figure 3.3: Alignment ($\langle \cos^2 \theta \rangle$) of a linear rotor hit with a gaussian laser pulse (width σ, intensity $\Delta\omega = 500$) at time $\tau = 5\sigma$, for increasing widths in the non-adiabatic ($\sigma = 0.01, 0.02, 0.05$), intermediate ($\sigma = 0.15, 0.25, 0.5$), and adiabatic ($\sigma = 1, 2, 5$) regimes. Initial state is the isotropic $J = 0$ spherical harmonic, which has alignment 1/3. The gaussian laser pulse profile is shown with heavy line.

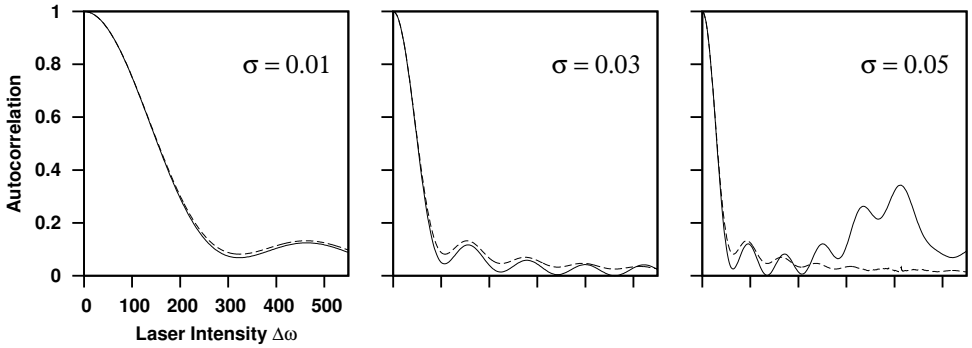

Figure 3.4: Post-pulse autocorrelation function after a gaussian laser pulse of intensity $\Delta\omega$, for three short pulse widths $\sigma = 0.01, 0.03, 0.05$. Initial state is the isotropic $J = 0$ spherical harmonic. Numerical results (solid) compared to sudden approximation (dashed).

The intermediate regime ($\sigma \approx 0.25$) molecules have maximum alignment during the pulse (like adiabatic), but alignment maxima recurrences are frequent and almost as high as the first. However, this behavior is *far* from uniform. As noted by Ortigoso [21], certain combinations of width σ and intensity $\Delta\omega$ in the intermediate regime can be found with zero post-pulse alignment, mimicing the adiabatic regime. However, these are very special cases, as shown in Figure 3.5. For the pulse width $\sigma = 0.5$ (corresponding to Ortigoso's Figure 1), the alignment after the pulse is flat for $\Delta\omega = 199.7$, but oscillates between anti-aligned and modestly aligned values for the only slightly different pulse intensities $\Delta\omega = 195$ and 205. The lesson is that in the intermediate regime, modest recurring alignment is possible, but the parameters σ and $\Delta\omega$ must be carefully screened since slightly off optimum values will produce reduced, or no, alignment.

This sentiment is roundly emphasized by Figure 3.6, which shows the autocorrelation function after laser pulses of various intensity and fixed width $\sigma = 0.25$ have hit the linear rotor and gone by. Note that the autocorrelation function is constant after the pulse has gone by. The alignment changes after the pulse is

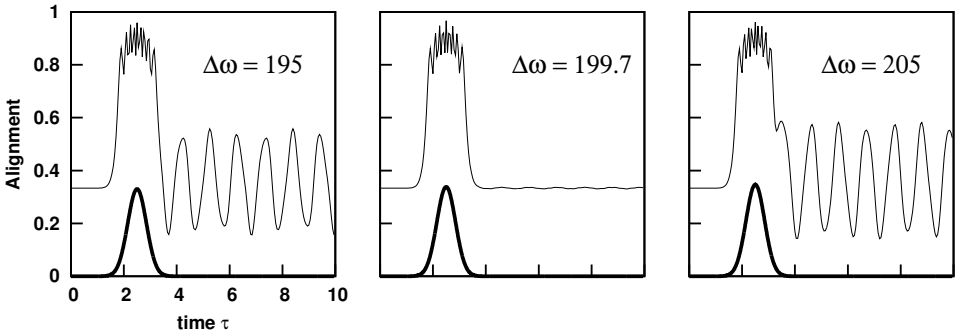

Figure 3.5: Alignment of a linear rotor after a gaussian laser pulse of width $\sigma = 0.5$, with intensity $\Delta\omega = 195, 199.7$, and 205. Pulse profile is also shown.

gone. Since the initial state in this figure is the isotropic $J = 0$ state, the autocorrelation function is a useful gauge of the alignment: if the autocorrelation function is one, alignment is necessarily 1/3 (isotropic); if it near zero, alignment is still fluctuating, likely greater than 1/3. The plot repeatedly has near-unity maxima as laser intensity increases, meaning at those special values of $\Delta\omega$ the laser pulse has had no effect on the rotor at all! There is no post-pulse alignment at those special values. If one wants field-free alignment with intermediate regime pulse width, special care must be taken to pick just the right $\Delta\omega$—not too big, not too small.

Gaussian pulse width $\sigma = 0.25$ is the most dramatic case, however. Smaller widths move more and more towards the *sudden approximation* limit, which never has such a highly recurring autocorrelation function. Bigger widths are the *adiabatic* limit, which as previously shown, always provide unity post-pulse autocorrelation function and are unsuitable for field-free alignment.

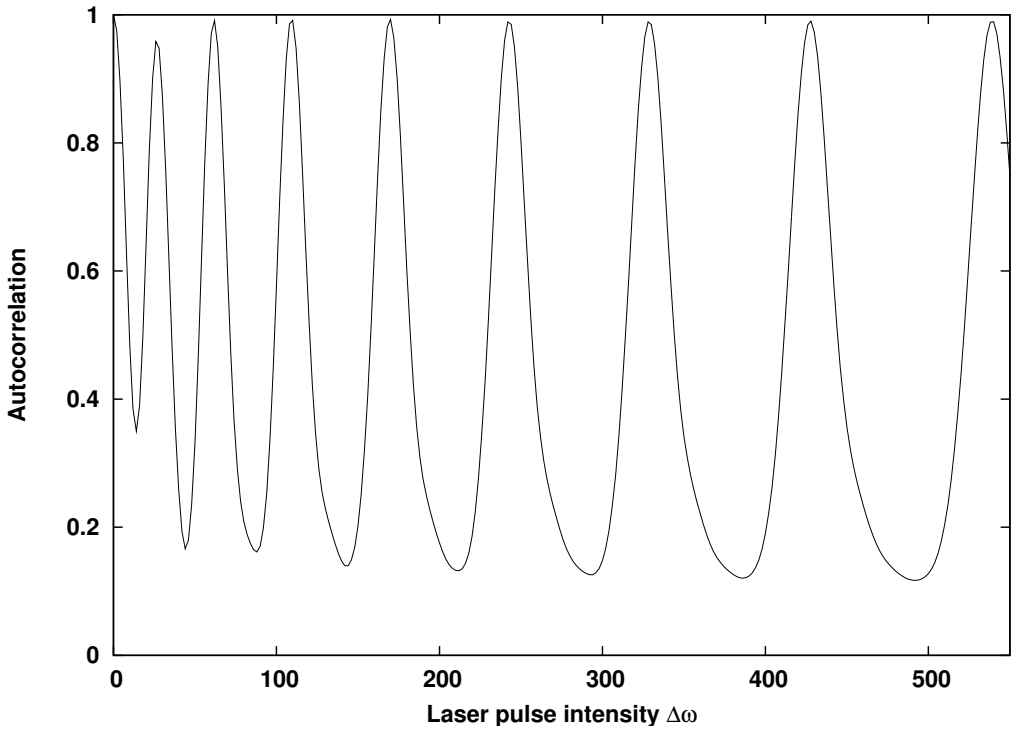

Figure 3.6: Autocorrelation function of a linear rotor after a gaussian laser pulse (width $\sigma = 0.25$) has gone by, as a function of the pulse intensity $\Delta\omega$.

Chapter 4

Energy Level Spacing Distributions

Quantum level spacing distributions for rotors in laser and static electric fields are calculated. Following a review of conceptual and historical development of this subject, the results emphasize that this approach qualitatively correlates classical chaos with purely quantum data. The analagous classical calculation is much more difficult than the quantum method presented here.

Spacing distributions (often called nearest neighbor spacing distributions) can describe many different phenomena—anything that occurs sequentially, from quantum energy levels, to roots of the Riemann zeta function, to bridges over a highway. Hayes [22] wrote an entertaining article exploring this facet. Haake [23] wrote a useful technical book connecting level spacing distributions with time reversal symmetry and random matrix theory, which is the basis for much of the material presented here. Gutzwiller [24, Ch. 16] has a nice overview.

A condensed version of this chapter has been published as Section V of ref. [25].

4.1 Avoided Crossings and Classical Chaos

It all starts with avoided crossings. They have long been studied by semiclassical methods since they present the challenge of being superficially purely a quantum phenomenon. But for those looking for further facets of the classical-quantum correspondence, the eigenstates during an avoided crossing behave analogously to classical invariant torii breaking by a nonintegrable perturbation.

Figure 4.1 shows an isolated avoided crossing in an energy correlation diagram

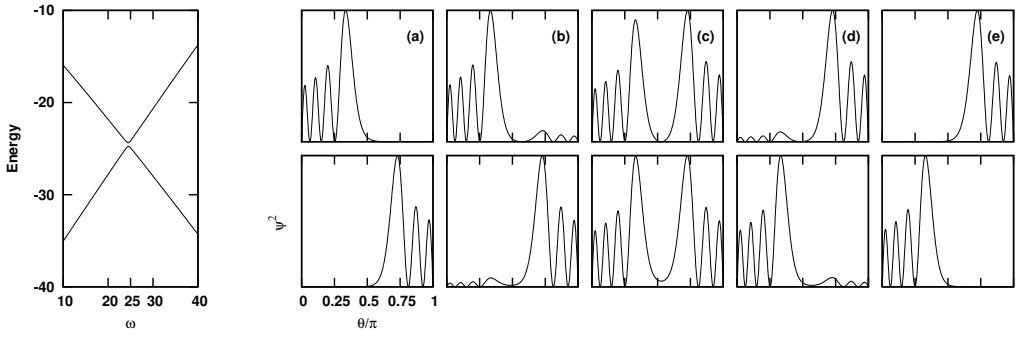

Figure 4.1: Avoided crossing of sixth (bottom) and seventh (top) eigenstates of a linear rotor in collinear fields, $\Delta\omega = 150$, $M = 0$ with energy correlation diagram at left and probability distributions at right (a)-(e) $\omega = 20$, 24, 24.5, 25, 30.

and corresponding probability distributions of the sixth and seventh eigenstates of a linear rotor with $\Delta\omega = 150$, $\beta = 0$, $M = 0$ and several close values of ω. At $\omega = 20$ the states have different character, two nodes in the right-hand well versus three nodes in the left-hand well. The states start to noticeably obtain each others character at $\omega = 24$. The states are almost identical, except the higher energy one has a node in the middle, at $\omega = 24.5$ which just about corresponds to the sharply avoided crossing in the energy correlation diagram in the Figure. For further increases in ω, the states fully exchange character—thus the state with two nodes in the right hand well becomes the one with higher energy.

During the avoided crossing each wave function occupies more of coordinate space through delocalization. When a classical system is perturbed, typically some invariant torii break to form stochastic layers visible in a surface of section. A stochastic layer or region is formed, in principle, by one trajectory which wanders through more of coordinate space than it did when it was constrained to a torus. Thus in both quantum avoided crossings and classical irregularities, the

system occupies more space. This is the physical connection that suggests avoided crossings and chaos can be quantitatively linked.

Let's approach the connection from the quantum side. Avoided crossings can be hard to spot in a correlation diagram. Some are easy to to spot, such as in Figure 4.1. Others may be so close to crossing they appear to truly cross. Some may be so widely avoided you couldn't guess that the states are significantly mixing. Some avoided crossings may involve more than two states, producing behavior not usually considered in simple theories. In short, this is a complicated business.

A way out is to statistically analyze the energy level spacings. A higher average level spacing througout a spectrum should mean more chaos in the related classical phase space. One way this connection has been explored is with nearest neighbor spacing distributions.

4.2 Definition and History

The spacing distribution $P(s)$ is the probability of finding a spacing s between two adjacent energy levels in a small interval centered at s. In practice, level spacings from calculation or experiment are sorted into a histogram, whose bar heights approximate a smooth $P(s)$. In theory, the limits of no level repulsion and linear level repulsion are known exactly. Heuristic derivations* of these forms follow.

A spacing s is formed if there are levels at x and $x+s$ with none in the interval $I = (x, x+s)$. Also define an infinitesimal interval $\mathrm{d}I = (x+s, x+s+\mathrm{d}s)$. The probability there is exactly one level in dI given no levels in I is defined as $\mu(s)$.

*This derivation is from Bohigas and Giannoni [26] who credit Wigner [27], but I could only find a puzzling sketch of this derivation in that article. A later article by Wigner [28] derives these distributions with differential equations.

Thus the probability $P(s)$ that given a level at x the next level is in $\mathrm{d}I$ is

$$\begin{aligned} P(s) &= (\text{prob. no level in } I) \times (\text{one level in } \mathrm{d}I \text{ given no level in } I) \\ &= \left(1 - \int_0^s P(s')\,\mathrm{d}s'\right) \times \mu(s) \\ &= \left(\int_s^\infty P(s')\,\mathrm{d}s'\right) \mu(s) \end{aligned}$$

This simple integral equation has the solution

$$P(s) = C\mu(s) \exp\left(-\int^s \mu(s')\,\mathrm{d}s'\right)$$

where C is a normalization constant. In the first case, suppose $\mu(s)$ is constant, meaning the next level may occur anywhere after x regardless of s. Then there is no correlation between levels. In the second case, suppose $\mu(s) \propto s$, meaning the next level cannot be at $s \approx 0$. The corresponding forms of the spacing distribution are[†]

$$P(s) = \begin{cases} \mathrm{e}^{-s} & \text{no level repulsion} \rightarrow \text{exponential, ``Poisson''} \\ \frac{\pi}{2} s \mathrm{e}^{-\pi s^2/4}. & \text{linear level repulsion} \rightarrow \text{``Wigner''} \end{cases} \tag{4.1}$$

The important difference is $P(0)$ is unity for the exponential distribution and zero for the Wigner distribution. The forms of $\mu(s)$ show that spectra with uncorrelated levels have many small spacings, while linearly repulsed levels have few small spacings. Both distributions approach zero as s becomes large because of the decreasing exponential factor, despite the forms of $\mu(s)$ being non-zero in this limit. The exponential has maximum probability at $s = 0$ while the Wigner maximum is close to $s = 1$.

[†]Schlier [29] reminds us to call this distribution exponential despite the widespread use of Poisson, since that name is widely used for a different statistical distribution.

The exponential spacing distribution results from a Poisson "process" formed by the quantum energy levels. Normally one thinks of a Poisson process as any sequence of events in which occurrences after any given time are independent of occurrences before that time—as with individual radioactive decays. This directly implies the exponential law governing first order kinetics. In terms of energy levels, the appearance of each level after the previous does not depend on how much energy range has been passed since the previous level. Many call such a spectrum "random" or "uncorrelated" since it obeys this law, and $P(s) = \mathrm{e}^{-s}$ must be the corresponding spacing distribution.

Wigner developed his distribution (the "Wigner surmise") while studying nuclear spectra. [28] He discovered that the statistics of nuclear spectra are the same as the eigenvalue statistics of random matrices. That is, a set of random hermitian matrices (the Gaussian Orthogonal Ensemble) taken as Hamiltonians provided eigenvalues with exactly the same spacing distribution as the experimental nuclear spectra. Porter [30] collected important articles that reflect the state in 1965.

Perhaps the first connection of classical dynamics to quantum level spacing distribution was given by Percival [31] in 1973. He qualitatively showed how there should be a quantum-classical correspondence between regular/irregular spectra and regular/irregular dynamics. Gradually, people began calculating spacing distributions for model systems, like harmonic oscillators [32] and Sinai billiards [33]. In sum, various authors did numerical work that verified regular and fully chaotic systems provide exponential and Wigner spacing distributions, respectively. Bohigas and Giannoni [26] provide a review of work done to 1984.

The most important work of these early years was furthering semi-classical understanding of the spacing distributions analytically and numerically. Berry

and Robnik [34] derived a distribution of quantum spacings starting from a generic classical system that has a mixed phase space with one connected chaotic region and an arbitrary number of isolated regular regions. This formula is never used. Instead, the simplest case with one regular region is always used. This is sometimes the case when it is applied; often this constraint is ignored. The distribution has one adjustable parameter that interpolates between exponential ($q = 0$) and Wigner ($q = 1$). Intermediate values of q correlate to the fraction of chaotic phase space in the classical system. The Berry-Robnik distribution is

$$P_{\mathrm{BR}}(s) = (1-q)^2 e^{-(1-q)s} \operatorname{erfc}\left[\frac{\sqrt{\pi}}{2} qs\right] + \left[2q(1-q) + \frac{\pi}{2} sq^3\right] e^{-(1-q)s - \frac{\pi}{4} s^2 q^2}. \quad (4.2)$$

In 1981, Brody *et. al* [35] published a review article on statistical theories of nuclear spectra. They included a distribution that empirically interpolates between exponential and Winger. That is, there is no theoretical basis at all for the formula. They termed q the "repulsion parameter" since it measured repulsion between energy levels. The Brody distribution is

$$P_{\mathrm{Brody}}(s) = (1+q)\beta x^q \exp\left(-\beta x^{1+q}\right) \quad (4.3)$$
$$\beta = \left[\Gamma\left(\frac{q+2}{q+1}\right)\right]^{q+1}.$$

The Brody and Berry-Robnik distributions are both used to estimate the fraction of chaotic classical phase space using only quantum energies. Berry-Robnik has a rigorous semi-classical foundation while Brody does not.

Later, researchers began studying systems relevant to atomic and molecular physics. For instance, level spacing distributions of hydrogen atom in a magnetic field [36] and combined electric and magnetic fields with arbitrary mutual orientation [37] have been calculated to study the transition from irregular to regular

classical dynamics. In all studies of this sort, Brody or Berry-Robnik parameters serve as a guide for determining or confirming classical phase space structure.

Several people have worked on rotor problems specifically. Grozdanov and McCarroll [38] calculated level spacing distributions of an asymmetric rotor in a static electric field. They divided a spectrum of 1300 levels into three sections and showed how the spacing distribution evolves from Wigner to exponential with increasing energy, suggesting the classical phase space evolves from chaos to regularity. Manfredi and Salasnich published [39], and then corrected [40], an assertion that free asymmetric rotor energies formed the anomalous distribution peaked at $s = 1$ seen by Berry [32] for harmonic oscillators. There were mistaken because they reduced the fully three dimensional asymmetric rotor system to one dimension (all levels corresponding to changing one good quantum number) which is guaranteed to yield the anomalous distribution. (This is discussed fully below, Section 4.3.) Lastly, Marchesan *et. al.* [41] calculated spacing distributions using experimental data and show coupling between internal and total rotation of methanol, based on transition from exponential to Wigner spacing distribution.

4.3 Interpreting Nearest Neighbor Spacing Distributions

The basic effect producing Wigner behavior, *i.e.* $P(s) \to 0$ as $s \to 0$, in the spacing distribution is level repulsion. This should only arise when the system has coupled degrees of freedom and chaotic phase space. When either of these conditions are not fulfilled, we expect exponential behavior, *i.e* $P(s) \to 1$ as $s \to 0$, in the spacing distribution.

First, a one DOF system has a Dirac delta spacing distribution peaked at $s = 1$. This is obviously true for the harmonic oscillator, which has equispaced

levels. But after the unfolding process (Section 4.4), one DOF spectra, such as the anharmonic oscillator spectrum, are transformed and resemble the harmonic oscillator spectrum. Some pathological one DOF systems yielding a Wigner spacing distribution may be constructed, [42] but they are certainly not germane to models studied here.

A n DOF separable system (trivially completely regular) decomposes into n one-dimensional problems, producing a completely uncorrelated spectrum and an exponential spacing distribution. Each energy level of the full system is a n-fold sum of energy levels, one from each separate one DOF spectrum. The individual spectra are not correlated with each other, and thus the full spectrum is uncorrelated. The spacing distribution is exponential, corresponding to completely regular dynamics.

A $n > 1$ DOF coupled (nonseparable) system will have some, perhaps small, degree of chaos. A chaotic trajectory breaks away from an unperturbed n-torus and samples more than n dimensions of phase space. The corresponding quantum effect is an avoided crossing, where two states mix and occupy previously unaccessed configuration space while the energies repel (Section 4.1). Thus a spectrum with many avoided crossings corresponds to chaotic classical dynamics, and the level spacing distribution $P(s) \to 0$ as $s \to 0$, quite unlike the exponential distribution. A spectrum corresponding to mixed phase space, with both regular and irregular regions, will provide $P(0)$ between zero and one, intermediate between Wigner and exponential behavior.

Also, any two uncorrelated spectra, no matter the internal correlations, will combine to form an exponential spacing distribution. Thus when a Wigner spacing distribution is found, we can be confident the underlying dynamical mechanism

is classical chaos and not an artifact. If a combined spectrum is exponential, it could be that all underlying spectra are exponential, or that (in a four DOF system with two separate chaotic subsystems) two separate spectra with Wigner spacing distributions have been combined. In the first case, regular dynamics truly support the exponential spacing distribution. In the second irregular dynamics falsely support an exponential spacing distribution.

Harmonic oscillators form the single known exception to this discussion. Berry [32] explored various incommensurate two DOF harmonic oscillators and found spacing distributions peaked away from $s = 0$. This is apparently an artifact of the exactly equal level spacings of the underlying one DOF harmonic oscillators. This effect can cause confusion if the spectrum contains some harmonic oscillator-like equispaced levels. The equal spacings support a spacing distribution peak at $s = 1$, which appears to be signature Wigner character to the untrained eye.

4.4 How to Obtain a Nearest Neighbor Spacing Histogram

The basic idea is to take adjacent energy levels in a spectrum and calculate their differences ("spacings"), and then sort them into histogram bins. However, some laborious procedures are needed to work around a few problems.

First, many Hamiltonians have discrete symmetries leading to trivially uncorrelated spectra. The linear rotor-tilted fields Hamiltonian has reflection plane (σ_{XZ}) symmetry. The full Hamiltonian matrix can be block diagonalized through a basis transformation into two sub-blocks. The new basis functions are eigenfunctions of the symmetry operator. Each sub-block can be independently diagonalized to produce a sub-spectrum. In our case, two sub-blocks produce two independent spectra associated with states having positive and negative parity with respect

to reflection plane symmetry. As the two spectra are independent and will produce exponential nearest neighbor spacing distributions when the full spectrum is analyzed, we must consider one symmetry species at a time.

Second, we want to compare different systems which may have inherently different energy scales and level densities, so that a raw energy spacing in one spectrum is not directly comparable to a spacing from a different system. In particular for rotational spectra, different energy regions of a single spectrum can have different local level densities. These barriers are surmounted by reducing all spectra to unit mean level density by "unfolding" them. The spacings in the unfolded spectra are histogrammed.

Here is how the unfolding process works. A given spectrum $\{E_i\}$ has raw spacings $\{E_{i+1} - E_i\}$, which are not suitable for histogramming as just discussed. To remedy the problem of varying level density between systems we want to compare, we might try to use the staircase function $N(E)$, defined as the number of energy levels with $E_i \leq E$. $N(E)$ maps the spectrum to one with exactly unit level spacings and thus exactly unit level density, no matter the original spectrum . (The graph of $N(E)$ resembles a jagged staircase over the entire spectrum, each step having height one at each eigenenergy E_i.) The new spectrum $\{N(E_i)\}$ contains no information about the original raw spacings since all spacings have been mapped to unity: the new spacings $\{N(E_{i+1}) - N(E_i)\}$ are all identically one, by definition. But if the jagged staircase $N(E)$ is replaced with a smooth low-order polynomial approximation $\bar{N}(E)$, some useful spectral fluctuations are reintroduced. Whereas with $N(E)$ the average level spacing was exactly one, with $\bar{N}(E)$ the average spacing $\bar{N}(E_{i+1}) - \bar{N}(E_i)$ is approximately unity because the individual spacings now fluctuate about unity by construction. In other words, the

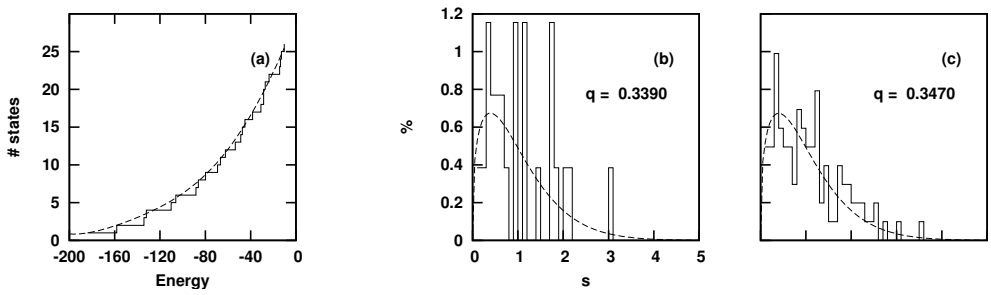

Figure 4.2: (a) Staircase $N(E)$ and polynomial fit $\bar{N}(E)$ of the lowest 25 energy levels for a linear rotor in collinear fields $\omega = 60, \Delta\omega = 150$ with (b) corresponding histogram of smoothed spacings and fitted Brody distrubtion with shown q. (c) Histogram of smoothed spacings for lowest 100 levels.

"smoothed spectrum" $\{\bar{N}(E_i)\}$ has average level density of one. The "smoothed spacings" $\{s_i\} = \{\bar{N}(E_{i+1}) - \bar{N}(E_i)\}$ are on average unity and populate the nearest neighbor spacing histogram. Apparently, the smoothed spacings still encode information about the original quantum level spacings. Thus, *unfolding* is this process of mapping a spectum to another spectrum with approximately unit level density, such that the essential information about the original dynamics is intact.

Figure 4.2 shows the staircase $N(E)$ and smoothed staircase $\bar{N}(E)$ for the lowest 25 states in a spectrum and the corresponding histogram of smoothed unfolded spacings. Notice that the histogram for 100 states, also shown, is closer to the fitting function but still signficantly rough.

A problem specific to the rotor-in-fields system (and most molecular problems) is that at physically typical field strengths, the spectra contain few levels—at most several hundred. Schlier [29] conclusively demonstrated that at least several thousand energy levels are required before the Brody fitting parameter q is meaningful. One rotational spectrum from our model cannot possibly satisfy this criterion. Thus we build a proper histogram by compiling histograms from spectra across a

correlation diagram. The compiled histogram characterizes a region of parameter space and not just one physical system, but nonetheless we can assign a number to the extent of classical chaos using only quantum mechanical results.

The compiled histogram is typically built from several hundred spectra taken uniformly in a continuous region of parameter space. Each spectrum is smoothed and histogrammed as outlined above. The individual histograms are then compiled into one histogram (with appropriate renormalization). The compiled histogram is finally fitted with the one-parameter Berry-Robnik or Brody distrubtion.

After the histogram is finally constructed, the one-parameter Berry-Robnik or Brody distribution is fit to it, the fitting parameter q being the quantitative measure of chaos in the classical phase space, as previously discussed. Figure 4.3 is the final product.

Bohigas *et. al.* [33] compiled spectra for the same reason and warned about using spectra too close in parameter space to ensure "independent information." For qualitative purposes, we have shown this consideration to be irrelevant—the q parameters do change but not by much. One could use as few as twenty spectra in the calculation of Figure 4.3 and obtain a plot with roughly the same features. Using three hundred spectra provides a smoother graph.

There are several somewhat arbitrary parameters of the NNS calculation that must be set in order to compute a histogram. Different sensible values can produce different results, so we state our methods clearly.

- The positive parity (with respect to reflection plane symmetry in the linear rotor-tilted fields Hamiltonian) spectrum is used to compute spacings; negative parity could be used, but it makes no difference.

- Raw spectrum fitted with $\bar{N}(E)$ a quintic polynomial; the usual result is a

slightly non-parabolic quintic.

- Histogram bins have width $\Delta = 0.10$; smaller values are feasible, and larger values have been used but this seems like a good compromise between sorting accuracy and histogram smoothness.

- The Berry-Robnik or Brody distribution is fitted to the final histogram at the righthand bin edge, *i.e.* at $s = 0.1, 0.2, \ldots$ not at $s = 0$, 0.1, ... Trials using the latter points produced sloping results when the former results trended flat. Also, it seems that putting a fit point right at $s = 0$ which would inaccurately reflect the range of spacings sorted into that bin, since the ultimate difference between exponential and Wigner behavior of $P(s)$ is the value at $s = 0$. Apparently our value of histogram bin width keeps this calculation under control.

4.5 Results

We studied linear rotors in collinear and tilted fields with nearest neighbor spacing histograms. For each compiled histogram, the fitted Brody parameter quantifies the extent of classical chaos.

Figure 4.3 shows compiled spacing histograms for a linear rotor in collinear fields of strength $\omega = 60, \Delta\omega = 150 \rightarrow 300$ (increments of 0.5, for a total of 301 spectra). The three presented histograms use the lowest N energies in each spectrum for $N = 25, 50$, and 100. The calculation uses 400 states at each point in the correlation diagram, starting at the ground state. The energies for $\omega = 60, \Delta\omega = 150$ are in $(-184, 724)$ with thirty bound states. When $\omega = 60, \Delta\omega = 300$ the energies are in $(-325, 670)$ with sixty bound states.

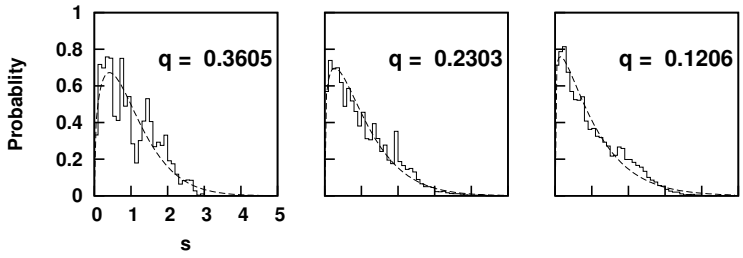

Figure 4.3: Compiled nearest neighbor spacing histograms for a linear rotor in collinear fields, $\omega = 60, \Delta\omega = 150 \rightarrow 300$ (increments of 0.5), using the N lowest levels in each spectrum: (left) $N = 25$, (center) $N = 50$, (right) $N = 100$. The Brody distribution is fit to the histograms with shown q.

The important point is that even though we know the classical phase space is entirely regular (no chaotic regions) the spacing distributions indicate significant irregularity if too few spacings are used. We expect Brody parameter $q = 0$. From these plots, 25×301 produces a jagged histogram with a medium Brody parameter $q = 0.36$. However, using 100×301 yields a smoother histogram with low, but not zero, Brody parameter $q = 0.12$. Clearly this method is not foolproof and will only safely produce qualitative results.

Let us briefly review the classical phase space structure of linear rotors in tilted fields. Figure 4.4 shows surfaces of section at several tilt angles and energies well below, just below, and well above the rotational barrier. Clearly the classical structure is regular at all energies when $\beta = 0$. At tilt angle $\beta = \pi/4$ and $\pi/2$, there is little if any chaos at high and low energy but is rife at intermediate energy. One might naively estimate the chaotic fraction of phase space to be 70% for (e). But different sections may show different relative chaotic volumes. Certainly a $\theta = 4\pi/5$ section corresponding to (e) would not have any regular regions associated with the stable wells which are rigorously θ-localized elsewhere. Calculating chaotic

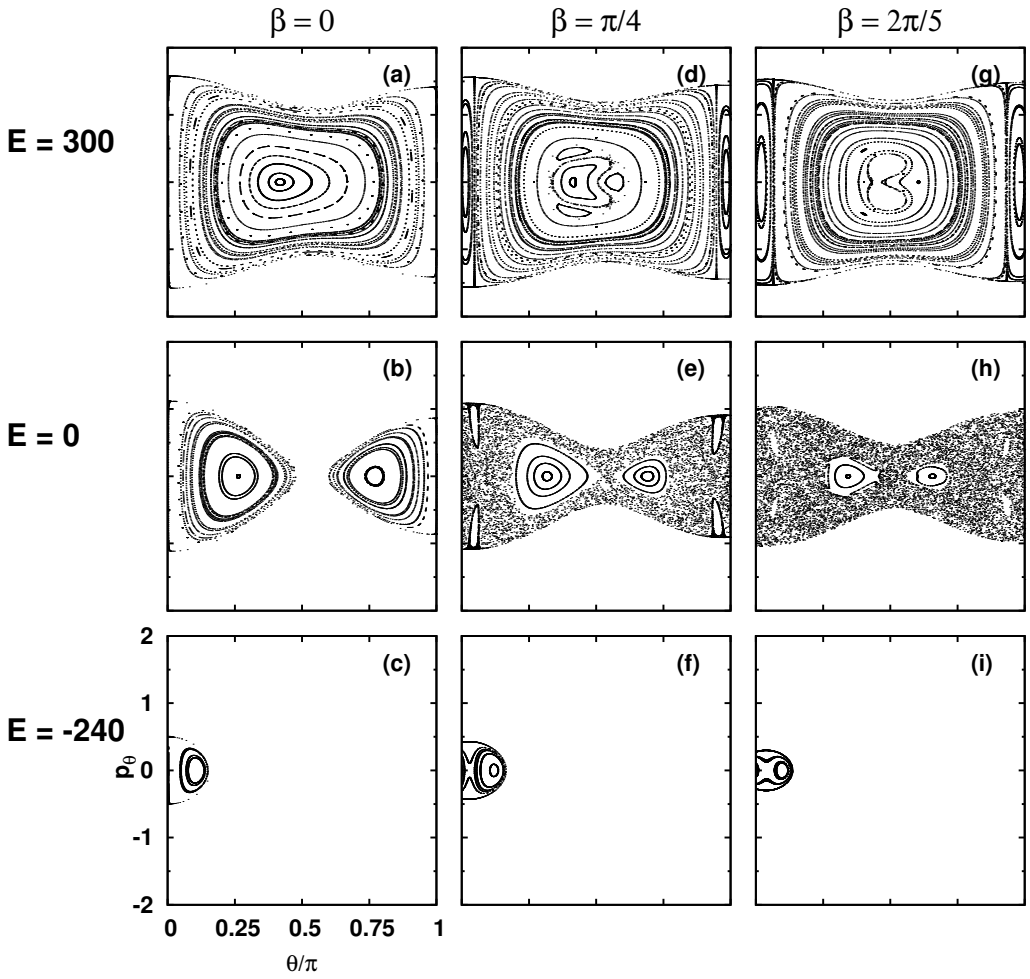

figure

Figure 4.4: Surfaces of section ($p_\theta - \theta, \phi = 0, p_\phi > 0$) for linear rotors in fields $\omega = 60, \Delta\omega = 240$, and (a)-(c) $\beta = 0$, (d)-(f) $\beta = \pi/4$, and (g)-(i) $\beta = 2\pi/5$. The top, middle, and bottom rows contain sos at energy $E = 300, 0, -240$ (well above, just below, and well below the rotational barrier).

volume exactly is difficult.

Next we examine how the Brody parameter changes with energy. We selectively sample the energy landscape by picking small stacks of adjacent levels from the spectra, which should measure the varying extent of chaos as a function of energy.

For small $N = 25$, initially only localized bound states (low energy) are sampled, but this gradually shifts to the barrier region and then free rotor as the base state increases in Figure 4.5. Such a small N produces erratic behavior in (a). The oscillating graph at high base state (high energy) occurs because the levels appear in near-degenerate clumps evolved from the same free rotor J. The clumped levels have small energy spacings, and the regions between clumps have large spacings, yielding sharp dips and peaks in the q plot. The Brody calculation is qualitatively incorrect here. These are practically free rotors with regular classical dynamics, and some unrelated quantum spectrum structure is assumed to be a widely avoided crossing.

At lower energy we expect the value of q to reflect the bound state dynamics. Note that as N increases the same features exist, but the graphs are smoother simply because much less data is changing in the calculation from each point left to right in the plot. Notably, at $N = 100$ (c) shows the baseline Brody parameter value is about 0.1 when the fields are not tilted—a case where classical phase space is completely regular, and we expect $q = 0$.

Tilting the fields induces chaotic classical dynamics which is reflected in Figure 4.5 (d)-(i) by a prominent hump in the Brody plots at low energy. We expect chaos and an obvious increase in the quantum Brody parameter at low energy. The comparison for tilt angle $\beta = \pi/4$ and $\beta = 2\pi/5$ suggests the latter system is more chaotic than the former, which would be a difficult result to obtain classically. The graphs eventually settle down to near-collinear behavior since the high-energy system is approaching free rigid rotor regularity.

The chaotic fraction of phase space as a function of tilt angle β can also be determined using energy versus β correlation diagrams, at fixed field strengths.

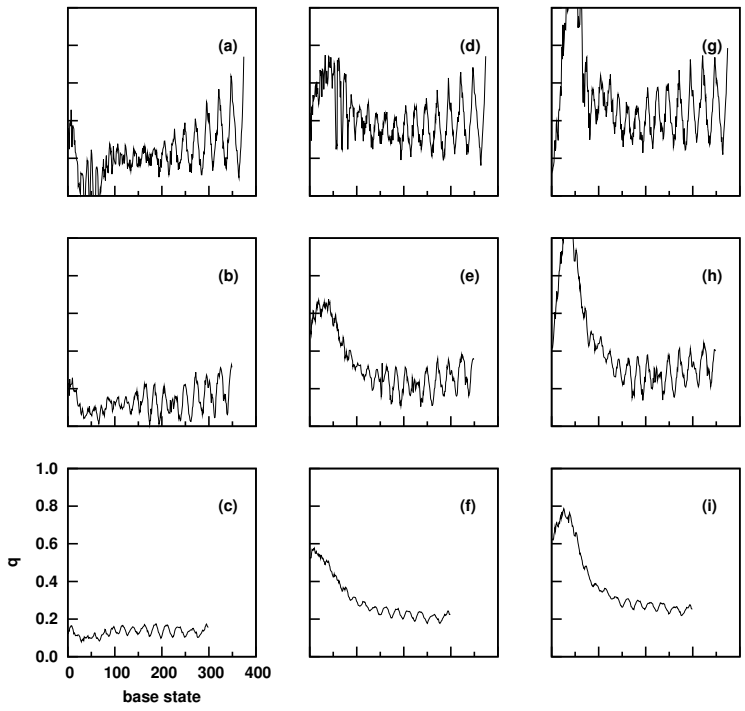

Figure 4.5: Brody parameter fitted to compiled nearest neighbor spacing histograms of a linear rotor in fields $\omega = 60$, $\Delta\omega = 150 \rightarrow 300$ (increments of 0.5) using N levels, as a function of the base state where the N levels begin. (a)-(c) $\beta = 0$, (d)-(f) $\beta = \pi/4$, (g)-(i) $\beta = 2\pi/5$. $N = 25, 50, 100$ down each column.

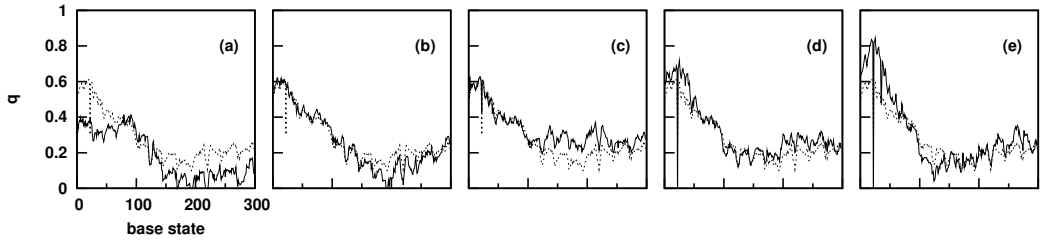

Figure 4.6: Brody parameter fitted to compiled nearest neighbor spacing histograms of a linear rotor in fields $\omega = 60$, $\Delta\omega = 240$, and $\beta/\pi =$ (a) $0 \rightarrow 0.1$, (b) $0.1 \rightarrow 0.2$, (c) $0.2 \rightarrow 0.3$, (d) $0.3 \rightarrow 0.4$ and (e) $0.4 \rightarrow 0.5$ (increments of 0.001) using $N = 100$ levels, as a function of the base state. Each plot is overlayed with aggregate q for $\beta/\pi = 0 \rightarrow 0.5$, the entire tilt angle range studied.

Figure 4.6 shows the Brody parameter fitted to level spacing histograms compiled as β changes, for a linear rotor in fields $\omega = 60$ and $\Delta\omega = 240$. Panel (a) corresponds to the tilt angle region closest to collinearity, $\beta = 0 \rightarrow 0.1\pi$. Also plotted is the aggregate Brody parameter corresponding to levels collected over the whole $\beta = 0 \rightarrow 0.5\pi$ domain. (This is reproduced in all five panels.) Thus panel (a) reveals a lower chaotic fraction in the near-collinear region than over the whole domain, which is sensible. The next panel (b) for $\beta/\pi = 0.1 \rightarrow 0.2$ shows almost identical behavior relative to the aggregate. The further panels (c), (d), and (e) each show increasing Brody parameter relative to the aggregate, particularly in the low energy (low base state N) regime, suggesting chaos is most important at energies near the rotational barriers when $\beta/\pi \sim 0.4$ or 0.5. This is in accord with Figure 4.5.

Chapter 5

Other Semi-Quantum Approaches

Here several other semi-quantum techniques are developed and applied to the rigid rotor in fields model. Illustrations of the classical-quantum correspondence seen here are mostly conceptual and qualitative. Nonetheless, they are interesting and may serve as starting points for future quantitative work. Certainly periodic orbits [24] have long been used in other systems, and the modern topic of monodromy [43] has yet to find a great application.

5.1 Monodromy

The basic goal of any physics problem is to solve the equations of motion. This is only analytically possible for a few simple models. In classical mechanics this means solving for action-angle variables, one pair for each degree of freedom. In quantum mechanics this means obtaining formulas for eigenenergies and eigenstates, which always result from separating Schrödinger's equation for n DOF into n ordinary differential equations. There is no obvious way to *a priori* know whether a given system is analytically solvable, but existence of monodromy necessarily forbids an analytic solution.

Monodromy ("once around") existence can be determined using a simple diagram of relative equilibria, whose construction is now explained in terms of our linear rotor in collinear fields problem. This model has cylindrical symmetry corresponding to the angular momentum projection M being a good quantum number. That is, the motion in azimuthal angle ϕ has successfully been separated and analytically solved. The motion in polar angle θ has yet to be solved. But by

calculating the extrema of the classical effective potential energy surface

$$V_{\text{eff}}(\theta; m) = \frac{m^2}{\sin^2 \theta} + V(\theta)$$

(where m is the classical analog of quantized M) some features of the system are revealed. The solutions of $\frac{\partial V_{\text{eff}}(\theta;m)}{\partial \theta} = 0$ are called *relative equilibria*, as opposed to global equilibria, because for nonzero m the system is actually moving but θ is constant. The potential energy of the classical relative equilibria are plotted as a function of m, forming an energy vs. m picture. The quantum energy levels can be superimposed, and they nest nicely inside the classical lines, as evident in Figure 5.1 for a linear rotor in a static electric field $\omega = 60$. Now monodromy is illustrated as follows.

Pick a quantum level in the figure, and then join it to an adjacent state. This serves as a local definition of quantum number, and by logical extension of your line segment a global definition of the quantum number should be established. This would be a handy definition to use so as to completely classify a spectrum. The process is pictured by parallel transport of a "cell" of adjacent quantum states. Transport carries this cell around an isolated unstable equilibrium at $m = 0$. At every stage the obvious extension of the local definition is made, but after going once around the unstable equilibrium the cells do not match. Apparently the local definition has changed. In other words, no global definition of the the quantum numbers is possible, meaning the Schrödinger equation cannot be analytically solved for this system. The classical analog is that no global set of action-angle variables can be analytically found.

Figure 5.2 shows energy vs. M diagrams for linear rotors in collinear fields. The left and right panels display systems with monodromy, corresponding to a linear rotor in static and collinear fields. For the static field, cell parallel transport

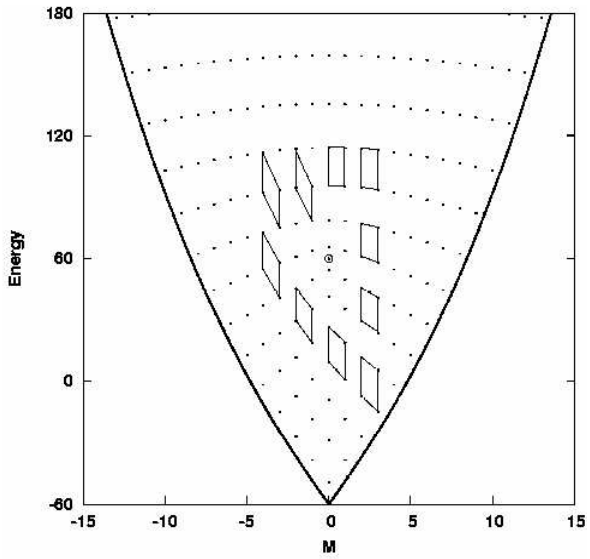

Figure 5.1: Energy vs. M monodromy diagram for a linear rotor in a static electric field $\omega = 60$. Superimposed on the quantum levels (represented by circles) is the parallel transport of a "cell" formed by connecting levels with locally adjacent quantum numbers.

around the isolated unstable classical equilibrium at $M = 0$ does not preserve the cell shape. Similarly for collinear fields, but one must transport around the central leaf.

Note that the quantum level structure inside the leaf is qualitatively different from that outside. The leaf interior corresponds to the asymmetric double well potential energy region where both wells are accessible but below the rotational barrier. Here we expect the quantum levels to split into tunneling doublets. No such doublets exist outside the leaf, since only one well exists in those regions of the figure.

The center panel of figure 5.2 does not have monodromy since no parallel transport around a barrier is possible—cell parallel transport cannot cut through the line dividing top and bottom.

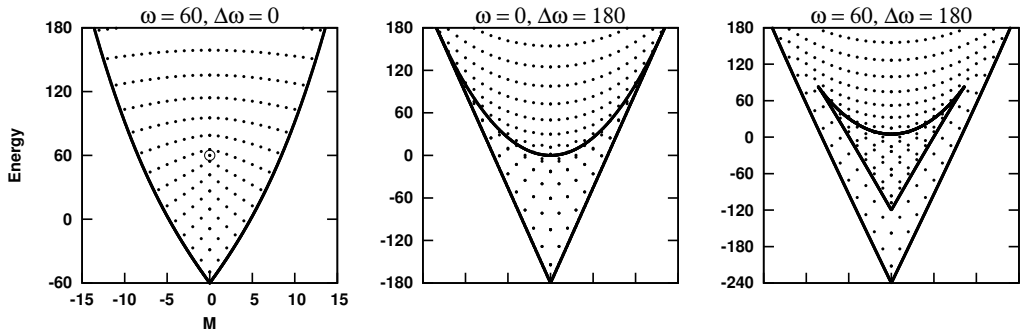

Figure 5.2: Energy vs. M monodromy diagrams for a linear rotor in collinear fields (left) $\omega = 60, \Delta\omega = 0$ (center) $\omega = 0, \Delta\omega = 180$ and (right) $\omega = 60, \Delta\omega = 180$. The quantum eigenstates (dots) are plotted with classical relative equilibria (lines). One isolated unstable classical equilibrium is in the middle of the left figure.

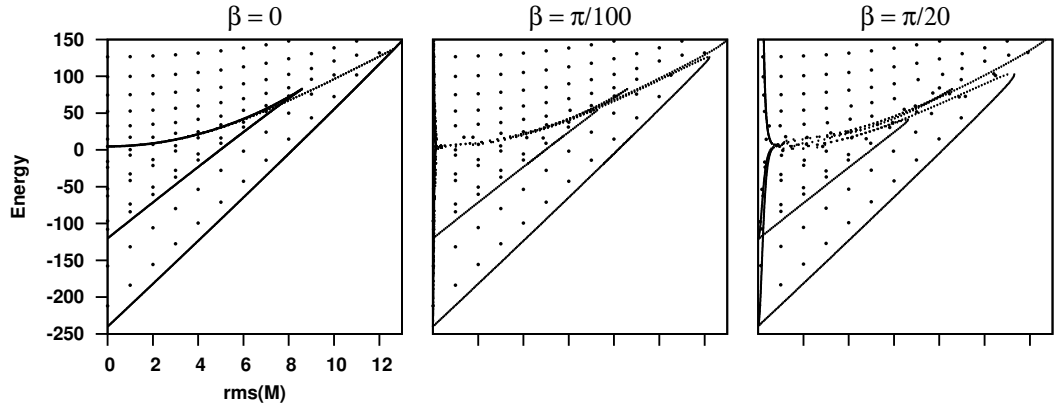

Figure 5.3: Energy vs. root mean square M monodromy diagrams for a linear rotor in tilted fields with $\omega = 60, \Delta\omega = 180$ and tilt angle (left) $\beta = 0$ (center) $\beta = \pi/100$ and (right) $\beta = \pi/20$. Plotted are quantum energies and classical periodic orbits.

Tilting the fields results in a non-integrable system, and the transition is shown in Figure 5.3 through E vs. M diagrams. Since increasing the tilt angle β from zero causes M to no longer be a good quantum number (classically, m is no longer a constant of the motion) the plots are now versus the root-mean-square expectation value of M in each quantum eigenstate. The left panel is exactly the right panel of Figure 5.2, except an extra line of classical points corresponding to low order periodic orbits is also included. As the tilt angle increases, the integrable structure breaking is seen as the quantum grid deforming exactly along the (higher energy) classical features.

Lastly, monodromy diagrams for a prolate symmetric top in collinear fields are shown in Figure 5.4. The quantum levels in each panel are calculated at fixed M as the molecular frame angular momentum projection K varies. Monodromy exists in the $M = 0$ case but disappears as M increases.

5.2 Husimi Distributions

Husimi distributions are constructed for linear rotor eigenstates in collinear fields. We modified a recent definition of rotational coherent states [44] to construct them.

A coherent state is a quantum state fixed by classical phase space variables, whose values specify where the wave function is localized in phase space. Although the usual definition is somewhat abstract, the desired properties of a coherent state are that the average position and momentum obey classical dynamics, and the state has minimum uncertainty. For example, the gaussian wave packet bound as a harmonic oscillator satisfies both properties. Such a wave function is the closest possible to a classical state.

Apropos a technique based on classical mechanics, free rotor action-angle vari-

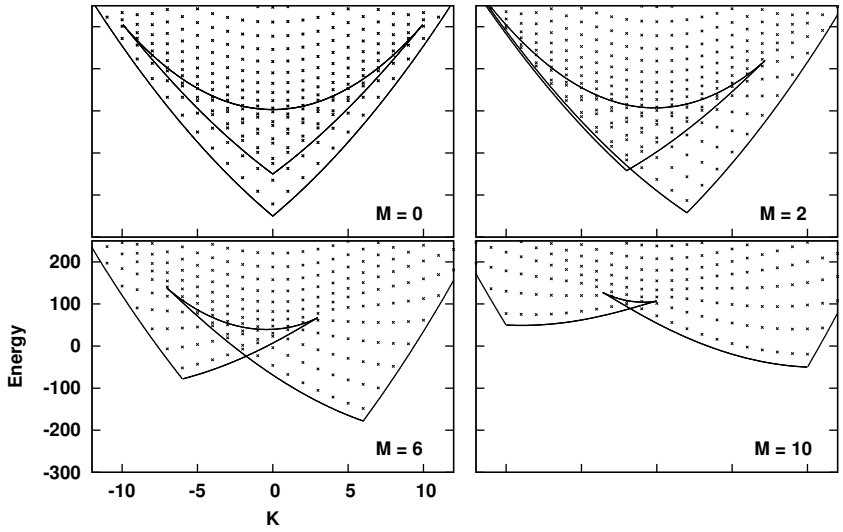

Figure 5.4: Energy vs K monodromy diagrams for a prolate symmetric rotor (rotational constants $a = 2$, $c = 1$) in collinear fields $\omega = 50$, $\Delta\omega = 200$ for $M = 0, 2, 6, 10$.

ables (j, q_j, m, q_m) are used. [17] But the quantum rotational wave functions are parameterized by Euler angles (ϕ, θ, χ). Using the assignment $(\phi, \theta, \chi) := (q_j, \bar{\theta}, q_m)$ between the two systems, with $\cos\bar{\theta} = m/j$, incorporates all of the action-angle variables appropriately obeying the angular bounds. Thus the common definition of the Wigner rotation matrix* D^J by a rotation operator, [14, §3.5]

$$\hat{R}(\phi,\theta,\chi)\,|JM\rangle = \sum_{M'} D^J_{M'M}(\phi,\theta,\chi)\,|JM'\rangle \equiv \sum_{M'} d^J_{M'M}(\theta)\mathrm{e}^{-\mathrm{i}M'\phi}\mathrm{e}^{-\mathrm{i}M\chi}\,|JM'\rangle$$

is now written, for specific $M = J$ and $M' \to M$:

$$|J\,q_j\,\bar{\theta}\,q_m\rangle := \hat{R}(q_j,\bar{\theta},q_m)\,|JJ\rangle = \sum_{M} d^J_{MJ}(\bar{\theta})\mathrm{e}^{-\mathrm{i}Mq_m}\mathrm{e}^{-\mathrm{i}Jq_j}\,|JM\rangle\,.$$

*The structure of the Wigner rotation matrices and rotational wave functions is discussed in Appendix A.3.

This is a rotated $M = J$ angular momentum eigenstate, which is still an eigenstate of $\boldsymbol{j}^2$ with eigenvalue $J(J+1)$, with classical action-angle variables as additional parameters but not as good quantum numbers. The key result of Morales *et. al.* [44] is that properly superimposing these states in J provides a rotational coherent state:

$$|j\, q_j\, m\, q_m\rangle := \mathrm{e}^{-j/2} \sum_J \frac{j^{J/2}}{\sqrt{J!}} \left|J\, q_j\, \bar{\theta}\, q_m\right\rangle .$$

The *Husimi distribution* is the squared overlap of a coherent state and a quantum wave function. Here, we use the rotational coherent state and an eigenstate of a linear rotor in collinear fields quantum Hamiltonian. When the fields are collinear, m is a constant of the motion, and the conjugate angle q_m is arbitrary. The Husimi distribution is only a function of j and q_j, resembling a classical phase space distribution. In fact, the analogous classical structure is an energy contour of the collinear fields Hamiltonian in action-angle variables: [17]

$$h = j^2 - \omega \cos q_j \sqrt{1 - m^2/j^2} - \Delta\omega \left(1 - m^2/j^2\right) \cos^2 q_j .$$

(Energy contours are the one-dimensional simplification of a surface of section. There is only one relevant degree of freedom for a linear rotor in collinear fields.)

All eigenstates are superpositions of angular momentum eigenstates (spherical harmonics) $|\psi\rangle = \sum_{JM} c_{JM}\, |JM\rangle$. The Husimi distribution is the the modulus square of S:

$$S = \langle j\, q_j\, m\, q_m|\psi\rangle = \mathrm{e}^{-j/2} \sum_{JM} \frac{j^{J/2}}{\sqrt{J!}}\, \mathrm{e}^{\mathrm{i}Mq_m}\, \mathrm{e}^{\mathrm{i}Jq_j}\, c_{JM}\, d^J_{MJ}(\bar{\theta}).$$

When M is a good quantum number (collinear fields) the sum over M is unnecessary. The trivial classical variables are set to $m = M$ and $q_m = 0$. The Husimi distribution is then plotted as contours of $|S|^2$ on the $j - q_j$ grid.

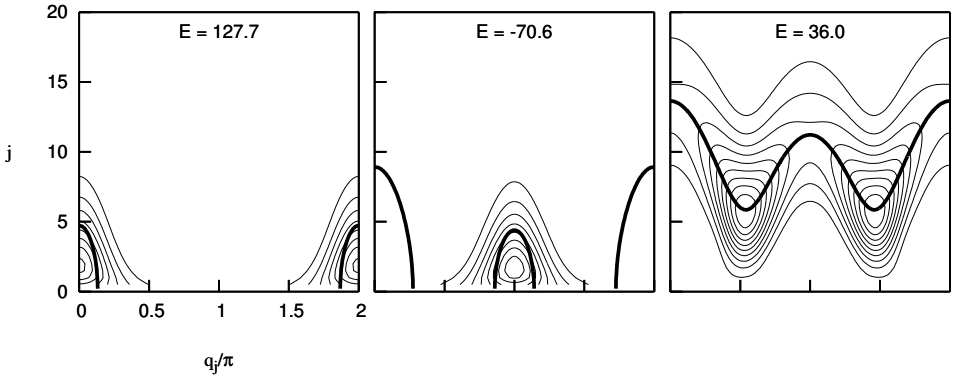

Figure 5.5: Husimi distributions of collinear fields eigenstates with $\omega = 30, \Delta\omega = 120, M = 0$. First, third, and tenth lowest energies from left to right. Heavy line is classical Hamiltonian contour at shown quantum eigenenergy.

Figure 5.5 shows several Husimi distributions of collinear fields eigenstates. First let us relate these pictures to the asymmetric double well potential energy surface reviewed in Section 1.6. The angle variable q_j is directly related to the Euler angle θ by [17]

$$q_j = \pi/2 - \arcsin \frac{j \cos\theta}{\sqrt{j^2 - m^2}} \mod 2\pi.$$

The PES extrema occur roughly at $\theta = 0, \pi$ (wells) and $\theta = \pi/2$ (barrier). This corresponds to wells at $q_j = 0, \pi$ (for $m = 0$) and barriers at $q_j = \pi/2, 3\pi/2$. (Multiple values of arcsin must be properly used.)

Thus the left panel of Figure 5.5, the Husimi distribution of the collinear fields ground state, shows classical phase space distribution localized in the more stable well. The center panel corresponds to an eigenstate of energy above both minima but below the barrier, and it happens to be localized in the high-lying well. Note that the heavy line is the corresponding classical Hamiltonian contour and shows accessible phase space in both wells, but the Husimi distribution is clearly confined

to one well in this picture, as is the corresponding quantum eigenstate. The right panel is the Husimi distribution for an an above barrier eigenstate. The contours reflect accessible free rotation in q_j at high j values but probability density maxima for low j at the barrier. This is correct, since a classical particle with energy just above a barrier slows down as it passes over due to energy conservation. Slowing over a barrier means the particle is increasingly likely to be found (thus more contours) at corresponding q_j, albeit at lower momentum j.

Unfortunately, developing Husimi distributions for tilted fields is harder. When M is not a good quantum number, the classical m is not conserved. The appropriate quantum analogue to the classical surface of section is not straightforward.

5.3 Periodic Orbits

Periodic orbits have long played a role in studying classical mechanics because phase space tends to organize around them. For example, in the classical surfaces of section Figure 4.4 the stable resonance zones are centered at a point, which reveals the existence of a periodic orbit that pierces the surface only at that point. The immediate phase space neighborhood consists of a dense set of quasi-periodic orbits that revolve around the true periodic orbit.

It hardly suffices to just say it, but periodic orbits have played a major role in semiclassical theories throughout the last thirty years. Certainly a high point are the trace formulas [24, Ch. 17] that equate a quantum density of states to a classical expression summed over periodic orbits.

We'll leave it at that, and note that we have calculated eigenstates for the linear rotor in tilted fields that nicely match classical periodic orbits, both stable (Figure 5.6) and unstable (Figure 5.7).

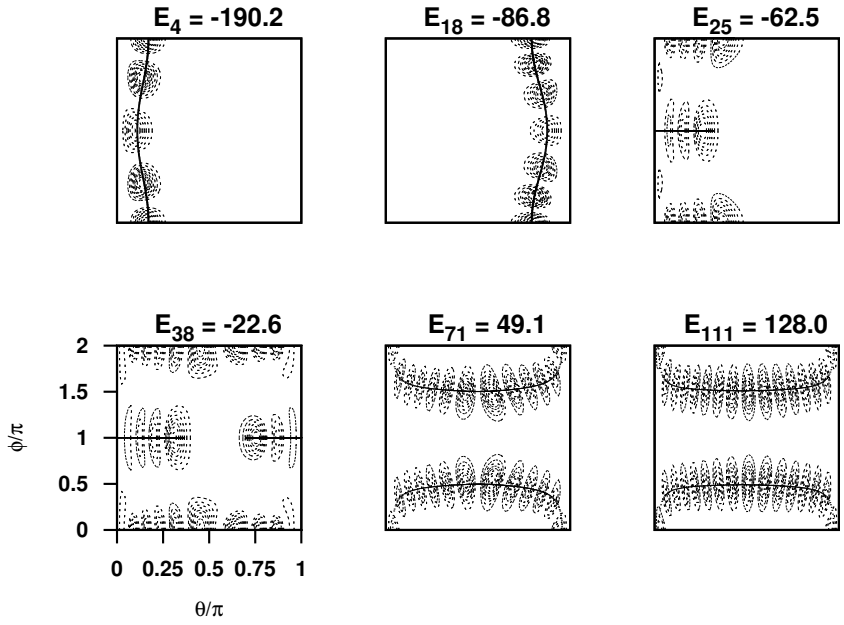

Figure 5.6: Stable periodic orbits superimposed on quantum probability distributions of eigenstates from $\omega = 60$, $\Delta\omega = 240$, and $\beta = \pi/4$.

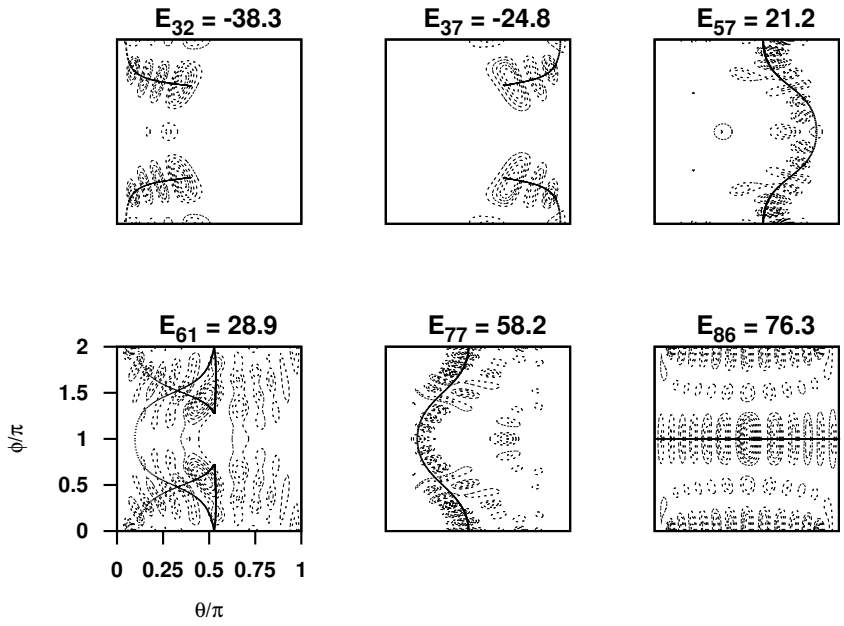

Figure 5.7: Unstable periodic orbits superimposed on quantum probability distributions of eigenstatesfrom $\omega = 60$, $\Delta\omega = 240$, and $\beta = \pi/4$.

Chapter 6

Summary and Future Work

Software has been developed to calculate all the important quantities of rigid rotating molecules in static electric and intense nonresonant laser fields, either alone or combined at arbitrary tilt angle using quantum mechanics. Primarily, this means energy levels and eigenstate probability distributions. The physically prescient alignment and orientation parameters were also calculated. Furthermore, arbitrary wave functions were numerically propagated under these Hamiltonians, including the presently important area of rotors in pulsed laser fields.

In particular we have reproduced the basic quantum calculations presented by Friedrich and Herschbach [4] for linear rotors in collinear fields. We extended their results by tilting the fields apart and calculating the same quantities as in the collinear case. The purpose was to investigate the quantum-classical correspondence of a rotational model when the classical dynamics is irregular.

The software also simulates symmetric and asymmetric rotors in static and intense nonresonant laser fields, although these results have not been presented here.

The quantum propagation of a linear rotor in a pulsed, intense nonresonant laser reproduced results from the literature; for instance, Ortigoso *et. al.* [21] We have emphasized the importance of pulse width relative to the rotational period regarding the post-pulse state and field-free alignment, as is well known, but also how the pulse intensity delicately affects the outcomes.

Some aspects of the quantum-classical correspondence for rotors in fields were developed. The main method was energy level spacing distributions for linear ro-

tors in tilted fields, which attempts to quantify the percentage of classical chaotic phase space using only quantum mechanical energy levels. The method was fully explained, including a technique for combining the data from spectra with too few levels into one set, which was necessary for better statistics. Indeed, the fundamental problem confronted here was that relevant molecular models have, at most, about one hundred levels in their spectrum which is too few for reliable results. Nevertheless, qualitative agreement was found. For instance, our prediction for the percentage of classical chaos necessarily increased as the fields tilted away from collinearity. Furthermore, the perhaps nontrivial result of greater chaos at $\beta \sim 0.4\pi$ than $\beta \sim 0.25\pi$ was found.

The other, purely conceptual, aspects of the quantum-classical corresondence illustrated were monodromy, Husimi distributions, and periodic orbits.

Quantum monodromy was shown to exist for a linear rotor in a static field and for a linear rotor in collinear static and laser fields. The perserverance of the correspondence between classical and quantum structure was shown in the energy-momentum diagrams as the fields were tilted. Also, quantum monodromy existence for symmetric rotors in collinear fields was illustrated.

Husimi distributions, which represent quantum eigenstates in terms of classical action-angle variables, for a linear rotor in collinear fields were calcuated. This required modifying a definition of a rotational quantum coherent state.

Lastly, classical periodic orbits that follow quantum eigenstates in this model were found.

Every section of the work presented here can be extended. The most basic step is to complete the catalog of correlation diagrams and wave functions of rotors in fields. The focus should be on nonlinear rotors, which have not been fully explored

because so many physical parameters are required to specify the inertial tensor and field configuration.

Quantum propagation of rotors in pulsed nonresonant laser fields needs to be extended to include nonlinear rotors. This will be in line with results for iodobenzene alignment. [5] Then further modifications of the pulse shape and sequence can be explored to optimize alignment (preferably field-free alignment). For example, some recent work [45] showed theoretical results for aligning all axes of ethene using several different pulse configurations, including a single elliptically polarized pulse, and two separate linearly polarized pulses. Also, Floquet analysis could be used to find periodic pulse sequences that leave the rotor in a *persistent* aligned state, unlike all the previous techniques which only have a periodically recurring alignment. Software developed for the present research can be adapted to calcuate Floquet states and quasi-energies.

The semi-quantum energy level spacing distribution calculations can be refined. Schlier [29] proposed the *maximum likelihood* method to replace histogramming of level spacings, which introduces an arbitrary histogram bin width parameter into the calculation. The maximum likelihood method may improve accuracy.

We used level spacing distributions to calculate the chaotic fraction of classical phase space using only quantum mechanics. The analagous classical calculation is difficult but would provide a quantitative check on the quantum-classical correspondence. This would involve determining the Lyapunov exponent for a representative sample of trajectories in phase space.

We only applied level spacing distributions to linear rotors. It would be easy to also use this technique for nonlinear rotors, and we could compare with Grozdanov and McCarroll's results [38] for an asymmetric rotor in a static electric field.

Husimi distributions should be extended to include tilted field configurations for linear rotors. The resulting picture would be a "quantum surface of section" that corresponds to a classical surface of section for the associated nonseparable two degree of freedom system.

Appendix A

Calculating the Basis Functions

This appendix details the algorithms used to calculate the basis functions in this thesis, namely the associated Legendre functions for linear rotors and symmetric top eigenstates (equivalently, Wigner rotation matrices) for nonlinear rotors. Also, a useful formula for calculating probability distributions is derived.

A.1 Spherical Harmonics and Associated Legendre Functions

Here are the essential formulas (A.6) used to calculate normalized associated Legendre functions $\mathcal{P}_J^M$, which in turn support the bases and eigenstates used in calculations throughout this work. These definitions are widely, but not universally, used. See Arfken's text. [18] The route starts with unnormalized ALFs, derives formulas with the correct form, and then expresses them in terms of normalized ALFs.

The basic definitions are:

Legendre Polynomials (Rodrigues's Formula) $J = 0, 1, 2, \ldots$

$$P_J(x) := \frac{1}{2^J J!} \left(\frac{\mathrm{d}}{\mathrm{d}x} \right)^J (x^2 - 1)^J \tag{A.1a}$$

Associated Legendre Functions, $|M| \leq J$

$$P_J^M(x) := (1 - x^2)^{M/2} \left(\frac{\mathrm{d}}{\mathrm{d}x} \right)^M P_J(x) \tag{A.1b}$$

Spherical Harmonics

$$Y_J^M(\theta, \phi) := N_J^M P_J^M(\cos\theta) \mathrm{e}^{\mathrm{i}M\phi} \tag{A.1c}$$

$$N_J^M := (-1)^M \sqrt{\frac{2J+1}{4\pi} \frac{(J-M)!}{(J+M)!}} \tag{A.1d}$$

Note that the spherical harmonics Y_J^M use the Condon-Shortley phase $(-1)^M$, and N_J^M is the normalization coefficient, defined separately for convenience.

Orthogonality:

$$\int_{-1}^{1} P_{J'}^{M}(x) P_{J}^{M}(x)\,\mathrm{d}x = \frac{2}{2J+1}\frac{(J+M)!}{(J-M)!}\delta_{JJ'}$$

$$\int_{-1}^{1} P_{J}^{M'}(x) P_{J}^{M}(x)(1-x^2)^{-1}\,\mathrm{d}x = \frac{(J+M)!}{M(J-M)!}\delta_{MM'}$$

$$\langle J'M'|JM\rangle = \int_0^{2\pi}\int_0^{\pi} Y_{J'}^{M'*}(\theta,\phi) Y_{J}^{M}(\theta,\phi)\sin\theta\,\mathrm{d}\theta\,\mathrm{d}\phi = \delta_{JJ'}\delta_{MM'}$$

Recurrence Relations:

$$(2J+1)xP_J^M = (J+M)P_{J-1}^M + (J-M+1)P_{J+1}^M \tag{A.3}$$

$$\begin{aligned}(2J+1)(1-x^2)^{1/2}P_J^M &= P_{J+1}^{M+1} - P_{J-1}^{M+1} \\ &= (J+M)(J+M-1)P_{J-1}^{M-1} \\ &\quad - (J-M+1)(J-M+2)P_{J+1}^{M-1}\end{aligned}$$

The relation between the normalized and unnormalized ALFs is

$$\mathcal{P}_J^M(x) = \sqrt{\frac{2J+1}{2}\,\frac{(J-M)!}{(J+M)!}}\,P_J^M(x). \tag{A.4}$$

There are several possible schemes for calculating associated Legendre functions P_J^M. [46] However, the most sensible, and reportedly the most numerically stable scheme is based on the second-order recurrence relation on index J, Eqn. (A.3) (M fixed). But two initial values are still needed to start the recurrence, and another equation is needed when $M < 0$. The scheme is illustrated in Figure A.1. These four formulas could require calculation of large factorials. This is neatly avoided by switching to normalized ALFs $\mathcal{P}_J^M$. The four formulas are derived here and listed as Eqns. (A.6).

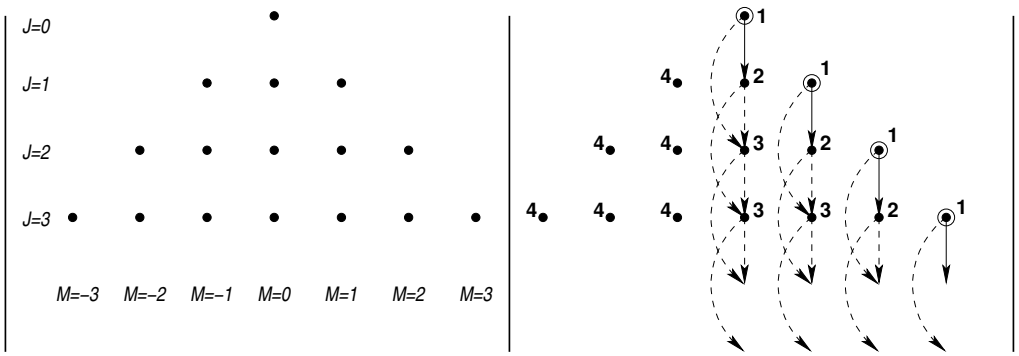

Figure A.1: Associated Legrendre Function pyramid. Left shows the JM quantum numbers applied to this schematic; right shows the recurrence relations, with 1–4 corresponding to the numerical scheme suggested by Eqns. (A.6). Arrows representing the last step are not shown.

The first step

Starting with Rodrigues's formula (A.1a) and (A.1b),

$$
\begin{aligned}
P_J^M(x) &= \frac{1}{2^J J!}(1-x^2)^{M/2}\left(\frac{\mathrm{d}}{\mathrm{d}x}\right)^{J+M}(x^2-1)^J \\
P_J^J(x) &= \frac{1}{2^J J!}(1-x^2)^{J/2}\left(\frac{\mathrm{d}}{\mathrm{d}x}\right)^{2J}(x^2-1)^J = \frac{1}{2^J J!}(1-x^2)^{J/2}(2J)! \\
&= \frac{1}{J!}(1-x^2)^{J/2}\left[\frac{2J}{2}\times(2J-1)\times\frac{2J-2}{2}\times(2J-3)\times\cdots\times 3\times\frac{2}{2}\times 1\right] \\
&= \frac{1}{J!}(1-x^2)^{J/2}\left[(2J-1)(2J-3)\ldots(3)(1)\right]\left[J(J-1)\ldots(2)(1)\right] \\
&= (1-x^2)^{J/2}(2J-1)!!.^{\dagger}
\end{aligned}
$$

Using the normalization relation (A.4) yields

$$\mathcal{P}_J^J = \left(\frac{2J+1}{2}\,\frac{(2J-1)!!^2}{(2J)!}\right)^{1/2}(1-x^2)^{1/2}$$
$$= \left(\frac{(2J+1)!!}{2}\,\frac{(2J-1)!!}{(2J)!}\right)^{1/2}(1-x^2)^{J/2} = \left(\frac{(2J+1)!!}{2(2J)!!}\right)^{1/2}(1-x^2)^{J/2}$$
$$\mathcal{P}_J^J(x) = \sqrt{\frac{1}{2}\prod_{k=1}^{J}\frac{2k+1}{2k}}\,(1-x^2)^{J/2}$$

The second step

Starting again with Rodrigues's formula,

$$P_{J+1}^J(x) = \frac{1}{2^{J+1}(J+1)!}(1-x^2)^{J/2}\left(\frac{\mathrm{d}}{\mathrm{d}x}\right)^{2J+1}(x^2-1)^{J+1}. \tag{A.5}$$

The derivative is the $(2J+1)$th derivative of a $(2J+2)$th order polynomial with only even powers of x. The only nonzero term results from differentiation of x^{2J+2}, namely $x(2J+2)!$:

$$P_{J+1}^J(x) = \frac{(2J+2)!}{2^{J+1}(J+1)!}(1-x^2)^{J/2}x$$
$$= \frac{(2J+2)(2J+1)}{2(J+1)}x\left[\frac{(2J)!}{2^J J!}(1-x^2)^{J/2}\right]$$
$$= (2J+1)xP_J^J(x)$$

Using the normalization relation on both sides yields

$$\mathcal{P}_{J+1}^J = (2J+1)x\left(\frac{2J+3}{2J+1}\,\frac{(2J)!}{(2J+1)!}\right)^{1/2}\mathcal{P}_J^J\mathcal{P}_{J+1}^J(x) \quad = x\sqrt{2J+3}\,\mathcal{P}_J^J(x).$$

[†]Notation (double factorial): $N!! := N(N-2)(N-4)\ldots(4 \text{ or } 3)(2 \text{ or } 1)$.

The third step

The corresponding recurrence relation for unnormalized ALFs, Eqn. (A.3), is available, so one needs only to rearrange slightly and use the normalization relation:

$$
\begin{aligned}
P_J^M &= \frac{1}{J-M}\left[(2J-1)xP_{J-1}^M - (J+M-1)P_{J-2}^M\right] \\
\mathcal{P}_J^M &= \frac{1}{J-M}\left(\frac{2J+1}{2}\frac{(J-M)!}{(J+M)!}\right)^{1/2}\left[(2J-1)x\left(\frac{2}{2J-1}\frac{(J+M-1)!}{(J-M-1)!}\right)^{1/2}\mathcal{P}_{J-1}^M\right. \\
&\qquad\qquad \left. - (J+M-1)\left(\frac{2}{2J-3}\frac{(J+M-2)!}{(J-M-2)!}\right)^{1/2}\mathcal{P}_{J-2}^M\right] \\
&= \frac{1}{J-M}\left[x(2J-1)\left(\frac{J-M}{J+M}\frac{2J+1}{2J-1}\right)^{1/2}\mathcal{P}_{J-1}^M\right. \\
&\qquad\qquad \left. - (J+M-1)\left(\frac{(J-M)(J-M-1)}{(J+M)(J+M-1)}\frac{2J+1}{2J-3}\right)^{1/2}\mathcal{P}_{J-2}^M\right] \\
&= x\sqrt{\frac{(2J-1)(2J+1)}{(J+M)(J-M)}}\mathcal{P}_{J-1}^M - \sqrt{\frac{(J-M-1)(J+M-1)}{(J+M)(J-M)}\frac{2J+1}{2J-3}}\mathcal{P}_{J-2}^M \\
\mathcal{P}_J^M &= \frac{1}{\sqrt{J^2-M^2}}\left[x\sqrt{4J^2-1}\,\mathcal{P}_{J-1}^M - \sqrt{\frac{2J+1}{2J-3}\left((J-1)^2-M^2\right)}\,\mathcal{P}_{J-2}^M\right]
\end{aligned}
$$

The fourth step

A standard formula relates a $M<0$ ALF to the ALF with the same $|M|$ and J. Then use the normalization relation:

$$
\begin{aligned}
P_J^{-M} &= (-1)^M\frac{(J-M)!}{(J+M)!}P_J^M \\
\mathcal{P}_J^{-M} &= (-1)^M\frac{(J-M)!}{(J+M)!}\left(\frac{(J+M)!(J+M)!}{(J-M)!(J-M)!}\right)^{1/2}\mathcal{P}_J^M\mathcal{P}_J^{-M} \qquad = (-1)^M\mathcal{P}_J^M.
\end{aligned}
$$

The four formulas are listed here for convenience:

$$\mathcal{P}_J^J = \sqrt{\frac{1}{2}\prod_{k=1}^{J}\frac{2k+1}{2k}}\,(1-x^2)^{J/2} \tag{A.6a}$$

$$\mathcal{P}_{J+1}^J = x\sqrt{2J+3}\,\mathcal{P}_J^J \tag{A.6b}$$

$$\mathcal{P}_J^M = \frac{1}{\sqrt{J^2-M^2}}\left[x\sqrt{4J^2-1}\,\mathcal{P}_{J-1}^M - \sqrt{\frac{2J+1}{2J-3}\,((J-1)^2-M^2)}\,\mathcal{P}_{J-2}^M\right] \tag{A.6c}$$

$$\mathcal{P}_J^{-M} = (-1)^M\,\mathcal{P}_J^M. \tag{A.6d}$$

Note that the coefficient of (A.6a) reflects how it is calculated: as a sequential product of numbers between one and two, which will never cause numerical overflow as may occur if organized another way.

Also, using normalized ALFs simplifies the spherical harmonic definition (A.1c) to

$$Y_J^M(\theta,\phi) = \frac{(-1)^M}{\sqrt{2\pi}}\mathcal{P}_J^M(\cos\theta)\mathrm{e}^{\mathrm{i}M\phi}. \tag{A.7}$$

A.2 Probability Distributions

The full probability distribution $P(\theta,\phi)$ is easily calculated for each point on a (θ,ϕ) grid, but a few tricks let it be calculated more efficiently. Each eigenvector $\psi(\theta,\phi) = \sum_{JM} c_J^M Y_J^M(\theta,\phi)$ is given by a set of coefficients $\{c_J^M\}$. Recall that any complex function can be written as a sum of real and imaginary parts:

$$\begin{aligned}
\psi(\theta,\phi) &= \frac{1}{\sqrt{2\pi}}\sum_{JM} c_J^M(-1)^M\mathcal{P}_J^M(\cos\theta)\mathrm{e}^{\mathrm{i}M\phi} \\
&= \frac{1}{\sqrt{2\pi}}\sum_{JM} c_J^M(-1)^M\mathcal{P}_J^M(\cos\theta)\cos M\phi \\
&\qquad + \mathrm{i}\frac{1}{\sqrt{2\pi}}\sum_{JM} c_J^M(-1)^M\mathcal{P}_J^M(\cos\theta)\sin M\phi \\
&\equiv \mathrm{Re}\,[\psi] + \mathrm{i}\,\mathrm{Im}\,[\psi]\,.
\end{aligned}$$

Then the probablity distribution is simplified (the Jacobian for this coordinate system is $\sin\theta$):

$$\begin{aligned} P(\theta,\phi) &= \psi^*\psi \sin\theta \\ &= \sin\theta(\mathrm{Re}\,[\psi] - \mathrm{i}\,\mathrm{Im}\,[\psi])(\mathrm{Re}\,[\psi] + \mathrm{i}\,\mathrm{Im}\,[\psi]) \\ &= \sin\theta(\mathrm{Re}\,[\psi]^2 + \mathrm{Im}\,[\psi]^2). \end{aligned}$$

Note that $P(\theta,\phi)$ has a reflection plane at $\phi = \pi$ so only half of the coordinate grid is actually used in the computations. This formula is the best way to calculate $P(\theta,\phi)$ since the real and imaginary parts of the wave function have the difficult parts in common and are calculated just once.

When M is a good quantum number, the (two-dimensional) probability distribution becomes uniform with respect to ϕ. Thus a full plot of $P(\theta,\phi)$ is unnecessary and even masks information. A *reduced probability distrubition* $P_\theta(\theta)$ is determined by integrating P over the polar angle ϕ:

$$\begin{aligned} P_\theta &= \int_0^{2\pi} \psi^*\psi \sin\theta \,\mathrm{d}\phi \\ &= \frac{1}{2\pi}\int_0^{2\pi} \left[(-1)^{M'} c_{J'}^{M'} \mathcal{P}_{J'}^{M'}(\cos\theta)\mathrm{e}^{-\mathrm{i}M'\phi}(-1)^{M} c_{J}^{M} \mathcal{P}_{J}^{M}(\cos\theta)\mathrm{e}^{\mathrm{i}M\phi}\right] \sin\theta \,\mathrm{d}\phi \\ &= \frac{1}{2\pi}\int_0^{2\pi} (-1)^{M+M'} c_{J'}^{M'} c_{J}^{M} \mathcal{P}_{J'}^{M'} \mathcal{P}_{J}^{M} \sin\theta \,(\cos(M'-M)\phi + \mathrm{i}\,\sin(M'-M)\phi)\,\mathrm{d}\phi \end{aligned}$$

where the implied sum is over all allowed quantum number pairs J', M' and J, M. The only ϕ dependence is in the complex exponential. Note that $M - M'$ is always an integer. Integrating a sine or cosine function over an integer number of cycles yields zero. The exception is when $M' - M = 0$: the cosine integral is $2\pi\delta_{MM'}$. So

$$P_\theta = c_{J'}^{M} c_{J}^{M} \mathcal{P}_{J'}^{M}(\cos\theta)\mathcal{P}_{J}^{M}(\cos\theta),$$

where the sum is now restricted to those quantum number pairs with $|M| \le J$ and $|M| \le J'$. The sum can be reorganized by separating $J = J'$ terms from $J \neq J'$

terms:

$$P_\theta = \sum_{JM} \left[c_J^M \mathcal{P}_J^M(\cos\theta)\right]^2 + \sum_{J' \neq J, M} c_{J'}^M c_J^M \mathcal{P}_{J'}^M(\cos\theta)\mathcal{P}_J^M(\cos\theta). \tag{A.8}$$

The latter sum has pair structure: each term with a given (J', J) is exactly equal to, and counted again as, the term for (JJ'). A factor of two can be extracted upon specifying summation indices:

$$P_\theta(\theta) = \sum_{J=0}^{\infty} \sum_{M=-J}^{J} \left[c_J^M \mathcal{P}_J^M(\cos\theta)\right]^2 + 2\sum_{J=0}^{\infty} \sum_{J'=J+1}^{\infty} \sum_{M=-J}^{J} c_{J'}^M c_J^M \mathcal{P}_{J'}^M(\cos\theta)\mathcal{P}_J^M(\cos\theta). \tag{A.9}$$

This a computationally useful form. Of course, in practice the infinite upper bounds are replaced by $J_{\max}$ fixed by the basis size.

A.3 Symmetric Rotor Eigenstates and Jacobi Polynomials

Symmetric top eigenstates form the orthonormal basis for the Hamiltonian matrix when we study symmetric and asymmetric rotors (tops) in fields. First I review their basic properties and definition in terms of Jacobi polynomials (equivalently, reduced rotation matrix elements). Then I discuss the algorithm for calculating these special functions.

Symmetric top eigenstates are determined by three quantum numbers J, M, K satisfying

$$\boldsymbol{J}^2 \left|JMK\right\rangle = J(J+1) \left|JMK\right\rangle$$

$$J_Z \left|JMK\right\rangle = M \left|JMK\right\rangle$$

$$J_z \left|JMK\right\rangle = K \left|JMK\right\rangle$$

with J^2, J_Z, J_z as the square of the total angular momentum operator, the operator for projection of angular momentum on a lab-fixed axis Z, and the operator for

projection of angular momentum on a body-fixed axis z, all measured in multiples of $\hbar$. The symmetric top eigenstates in terms of the Euler angles (ϕ, θ, χ) are

$$\langle \phi\, \theta\, \chi | JMK \rangle = D^{J*}_{MK}(\theta, \phi, \chi) = \sqrt{\frac{2J+1}{8\pi^2}}\, \mathrm{e}^{\mathrm{i}M\phi} d^J_{MK}(\theta) \mathrm{e}^{\mathrm{i}K\chi}$$

with

$$d^J_{MK}(\theta) = \sqrt{\frac{(J+K)!(J-K)!}{(J+M)!(J-M)!}} \left(\sin\frac{\theta}{2}\right)^{K-M} \left(\cos\frac{\theta}{2}\right)^{K+M} P^{(K-M,K+M)}_{J-K}(\cos\theta).$$

The special function $d^J_{MK}(\theta)$ is the *reduced rotation matrix*, which is further expressed in terms of *Jacobi polynomials* $P^{(\alpha,\beta)}_n(x)$.* These are well known special functions that are a generalization of Legendre polynomials. Jacobi polynomials are orthogonalized over $-1 \le x \le 1$ with weighting function $(1-x)^\alpha(1+x)^\beta$, while Legendre polynomials are the special case $\alpha = \beta = 0$. In fact, when the symmetric rotor reduces to a linear rotor ($K = 0$) the eigenstates reduce to spherical harmonics, as they should.

*Using $\alpha = K - M, \beta = K + M, n = J - K, x = \cos\theta$. The α, β, n notation is normally used in the classical mathematics context for Jacobi polynomials. The J, M, K, θ notations is used for quantum wavefunctions.

Basic properties of the Jacobi polynomials are:

$$\text{orthogonality} \qquad \int_{-1}^{1} P_m^{(\alpha,\beta)}(x) P_n^{(\alpha,\beta)}(x)\,(1-x)^\alpha (1+x)^\beta \,\mathrm{d}x$$
$$= \frac{2^{\alpha+\beta+1}}{2n+\alpha+\beta+1} \frac{\Gamma(n+\alpha+1)\Gamma(n+\beta+1)}{\Gamma(n+\alpha+\beta+1)n!}\delta_{mn}$$

$$\text{recurrence} \qquad 2(n+1)(n+\alpha+\beta+1)(2n+\alpha+\beta) P_{n+1}^{(\alpha,\beta)}(x) \tag{A.10}$$
$$= [(2n+\alpha+\beta+1)(\alpha^2-\beta^2) + (2n+\alpha+\beta)_3 x] P_n^{(\alpha,\beta)}(x)$$
$$- 2(n+\alpha)(n+\beta)(2n+\alpha+\beta+2) P_{n-1}^{(\alpha,\beta)}(x)$$

$$\text{Rodrigues} \qquad P_n^{(\alpha,\beta)}(x) := \frac{(-1)^n}{2^n n!}(1-x)^{-\alpha}(1+x)^{-\beta}\frac{\mathrm{d}^n}{\mathrm{d}x^n}\left[(1-x)^{\alpha+n}(1+x)^{\beta+n}\right] \tag{A.11}$$

$$\text{alt. definition} \qquad P_n^{(\alpha,\beta)}(x) := (n+\alpha)!(n+\beta)! \sum_s \frac{\left(\frac{x-1}{2}\right)^{n-s}\left(\frac{x+1}{2}\right)^s}{s!(n+\alpha-s)!(\beta+s)!(n-s)!} \tag{A.12}$$

where the sum in the last formula is over all s such that the factorials have nonnegative argument.

Strictly speaking, Jacobi polynomials defined by the Rodrigues formula are valid only for $\alpha, \beta > -1$ to ensure the weighting function $(1-x)^\alpha(1+x)^\beta$ does not cause divergent integrals.[†] But $\alpha = K - M \le -1$ and $\beta = K + M \le -1$ are physically permissible and we need to use the corresponding wave functions. Several adjunct formulas are used to relate negative α or β (or both) Jacbobi polynomials to those with postive α or β:

$$\alpha < 0 \quad P_n^{(\alpha,\beta)}(x) = \frac{(n+\alpha)!(n+\beta)!}{n!(n+\alpha+\beta)!}\left(\frac{x-1}{2}\right)^{-\alpha} P_{n+\alpha}^{(-\alpha,\beta)}(x) \tag{A.13}$$
$$\beta < 0 \quad P_n^{(\alpha,\beta)}(x) = \frac{(n+\alpha)!(n+\beta)!}{n!(n+\alpha+\beta)!}\left(\frac{x+1}{2}\right)^{-\beta} P_{n+\beta}^{(\alpha,-\beta)}(x)$$
$$\alpha,\beta < 0 \quad P_n^{(\alpha,\beta)}(x) = \left(\frac{x-1}{2}\right)^{-\alpha}\left(\frac{x+1}{2}\right)^{-\beta} P_{n+\alpha+\beta}^{(-\alpha,-\beta)}(x)$$

[†]In particular, *Mathematica* produces strange results when using `JacobiP[]` with negative α, β.

These formulas can be derived from the alternate definition (A.12), which is valid for negative α, β. For instance, when $\alpha < 0$,

$$P_n^{(-\alpha,\beta)}(x) = (n-\alpha)!(n+\beta)! \sum_s \frac{\left(\frac{x-1}{2}\right)^{n-s}\left(\frac{x+1}{2}\right)^s}{s!(n-\alpha-s)!(\beta+s)!(n-s)!}$$

$$\frac{(n+\alpha)!(n+\beta)!}{n!(n+\alpha+\beta)!}\left(\frac{x-1}{2}\right)^{-\alpha} P_{n+\alpha}^{(-\alpha,\beta)}(x) = \frac{(n+\alpha)!(n+\beta)!}{n!(n+\alpha+\beta)!}\left(\frac{x-1}{2}\right)^{-\alpha} \times n!(n+\alpha+\beta)! \sum_s \frac{\left(\frac{x-1}{2}\right)^{n+\alpha-s}\left(\frac{x+1}{2}\right)^s}{s!(n-s)!(\beta+s)!(n+\alpha-s)!}$$

which simplifies to the (A.13) when checking the definition (A.12).

Calculating symmetric top eigenfunctions $d^J_{MK}(\cos\theta)$ hinges on calculating Jacobi polynomials $P_n^{(\alpha,\beta)}(x)$. The latter are calculated by the second-order recurrence (A.10) with seed formulas for the $n = 0$ and $n = 1$ Jacobi polynomials obtained from the Rodrigues definition (A.11):

$$P_{n=0}^{(\alpha,\beta)}(x) = 1$$
$$P_{n=1}^{(\alpha,\beta)}(x) = \frac{1}{2}\left[2(\alpha+1) + (\alpha+\beta+2)(x-1)\right].$$

For given α, β the Jacobi polynomials are thus determined. However, rotational problems usually require many different values of α, β in one calculation, corresponding to all allowed values of K and M.

When the electric fields are collinear, M is fixed and (except for symmetric rotors with fixed K) the basis contains symmetric top eigenstates of all J from zero to some maximum and all allowed K. A "pyramid" schematically represents this basis, shown in Figure A.2, analagous to the $J - M$ pyramid for spherical harmonics and linear rotors. Each column of the pyramid represents one sequence of Jacobi polynomials indexed by n bound by successive application of the recur-

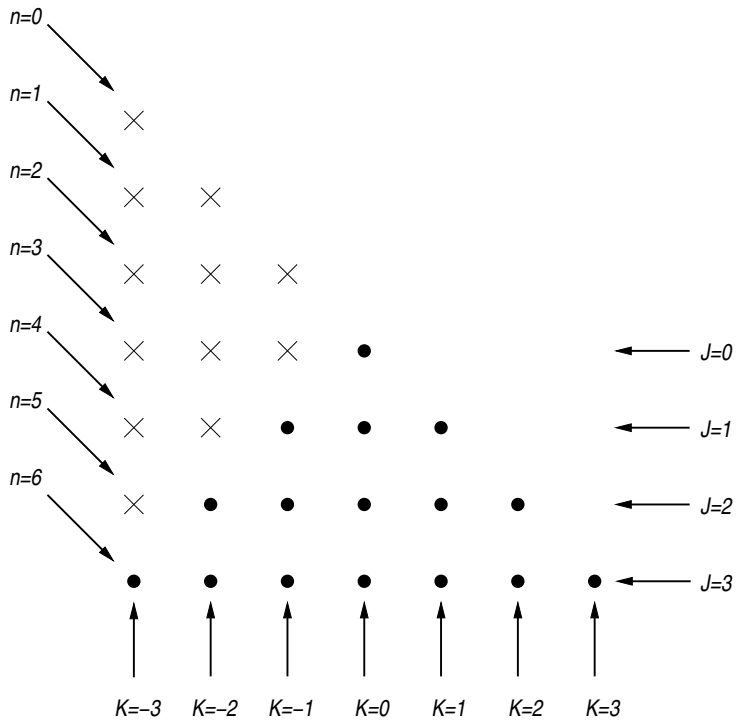

Figure A.2: J-K pyramid illustrating basis convention for symmetric top wavefunctions and the algorithm for calculating Jacobi polynomials. Circles represent physical states used in the basis, and crosses represent mathematically valid unphysical states that are calculated as part of the recurrence scheme to obtain values represented by circles below them. Pictured here is the $M = 0$ case; $|M| \geq 0$ changes circles representing invalid states $J \leq |M|$ to crosses.

rence relation, given $n = 0$ and $n = 1$ values. This determines the right half of the pyramid ($K \geq 0$).

If $K < 0$, the top index $n = J - K$ of each column is not zero ($n = 2, 4, 6, \ldots$ for $K = -1, -2, -3. \ldots$) so the full recurrence is calculated but low n polynomials are thrown out. The circles in Figure A.2 represent polynomials needed for the physical basis states, and crosses represent polynomials that get thrown out since they represent unphysical combinations of quantum numbers with $|K| \geq J$. But these thrown out values must be calculated because they form the initial part of the

recurrence sequence leading to the polynomials supporting physical basis states. At the extreme, the leftmost column at $K = -J$ only has one polynomial used as a physical basis state, and $2J$ previous recurrence results are thrown out to obtain it.

Lastly, the special case of $\alpha, \beta < 0$ is considered. The preceeding steps are all completed using $|\alpha|, |\beta|$ and then converted with the special formulas (A.13). Note that only some of the columns—tending to the left half of the pyramid—have negative α or β.

My program actually calculates normalized reduced rotation matrix elements $\bar{d}_n^{(\alpha,\beta)}(x)$ instead of $P_n^{(\alpha,\beta)}(x)$. This eliminates factorial calculations and simplifies several formulas at the expense of the recurrence relation becoming slightly more complicated. However, the process is essentially as described above. The relevant identities for $\bar{d}_n^{(\alpha,\beta)}(x)$ are:

$$\text{definition} \qquad \bar{d}_n^{(\alpha,\beta)}(x) = \sqrt{\frac{1}{2}(2n+\alpha+\beta+1)}\sqrt{\frac{(n+\alpha+\beta)!n!}{(n+\alpha)!(n+\beta)!}} \times \left[\frac{1}{2}(1-x)\right]^{\alpha/2}\left[\frac{1}{2}(1+x)\right]^{\beta/2} P_n^{(\alpha,\beta)}(x)$$

$$\text{orthonormality} \qquad \int_{-1}^{1} \bar{d}_m^{(\alpha,\beta)}(x)\bar{d}_n^{(\alpha,\beta)}(x)\,\mathrm{d}x = \delta_{mn}$$

$$\text{recurrence} \qquad \bar{d}_{n+1}^{(\alpha,\beta)} = \frac{1}{2c}\sqrt{f(c+3)(c+1)}(\alpha^2-\beta^2+c(c+2)x)\bar{d}_n^{(\alpha,\beta)}(x) - \frac{c+2}{c}\sqrt{\frac{c+3}{c-1}}\sqrt{fn(n+\alpha+\beta)(n+\alpha)(n+\beta)}\bar{d}_{n-1}^{(\alpha,\beta)}(x)$$

$$\alpha < 0, \beta \geq 0 \qquad \bar{d}_n^{(\alpha,\beta)}(x) = (-1)^{\alpha}\bar{d}_{n+\alpha}^{(-\alpha,\beta)}(x)$$

$$\alpha \geq 0, \beta < 0 \qquad \bar{d}_n^{(\alpha,\beta)}(x) = \bar{d}_{n+\beta}^{(\alpha,-\beta)}(x)$$

$$\alpha < 0, \beta < 0 \qquad \bar{d}_n^{(\alpha,\beta)}(x) = (-1)^{\alpha}\bar{d}_{n+\alpha+\beta}^{(-\alpha,-\beta)}(x)$$

using $c = 2n+\alpha+\beta$ and $f = 1/(n+1)(n+\alpha+1)(n+\beta+1)(n+\alpha+\beta+1)$.

Appendix B

Hamiltonian Matrix Element Derivations

B.1 Matrix Elements in Spherical Harmonic Basis

Matrix elements for the various linear rotor Hamiltonians in the spherical harmonic basis are derived here.

Static field matrix elements

$$
\begin{aligned}
&\langle J'\, M' \,|\cos\theta|\, JM\rangle \\
&\quad = N_J^M N_{J'}^{M'} \left[\int_0^{2\pi} \mathrm{e}^{-\mathrm{i}(M'-M)\phi}\,\mathrm{d}\phi\right]\left[\int_0^{\pi} P_{J'}^{M'}(\cos\theta) P_J^M(\cos\theta)\cos\theta\sin\theta\,\mathrm{d}\theta\right] \\
&\quad = N_{J'}^{M'} N_J^M\,[2\pi\delta_{MM'}]\left[\int_{-1}^{1} x P_{J'}^M(x) P_J^M(x)\,\mathrm{d}x\right]
\end{aligned}
$$

$$
\begin{aligned}
&\langle J'\, M \,|\cos\theta|\, JM\rangle \\
&\quad = \frac{2\pi}{2J'+1} N_{J'}^M N_J^M \int_{-1}^{1} \left[(J'+M)P_{J'-1}^M + (J'-M+1)P_{J+1}^M\right] P_J^M\,\mathrm{d}x
\end{aligned}
$$

By orthogonality, this is nonzero only when $J' = J \pm 1$. Take $J' = J+1$:

$$
\begin{aligned}
\langle J+1\; M \,|\cos\theta|\, JM\rangle &= \frac{2\pi}{2(J+1)+1} N_J^M N_{J+1}^M \times (J+M+1)\frac{2}{2J+1}\frac{(J+M)!}{(J-M)!} \\
&= \left[\frac{(J+M+1)(J-M+1)}{(2J+1)(2J+3)}\right]^{1/2} \\
\langle J+1\; M \,|\cos\theta|\, JM\rangle &= \left[\frac{(J+1)^2 - M^2}{(2J+1)(2J+3)}\right]^{1/2}.
\end{aligned}
$$

Note that the result for $J' = J-1$ is directly recoverable from this formula: simply apply hermiticity and a dummy substitution $J \to J-1$ on both sides.

And when the fields are tilted, the X component of the static field requires:

$$\begin{aligned}\langle J'\, M'\, |\cos\phi\sin\theta|\, JM\rangle &= N_{J'}^{M'} N_J^M \left[\int_0^{2\pi} \mathrm{e}^{-\mathrm{i}(M'-M)\phi}\cos\phi\,\mathrm{d}\phi\right] \\ &\qquad \times \left[\int_0^{\pi} P_{J'}^{M'}(\cos\theta)\sin\theta P_J^M(\cos\theta)\sin\theta\,\mathrm{d}\theta\right] \\ &= N_{J'}^{M'} N_J^M \left[\pi\delta_{M\pm1\,M'}\right]\left[\int_{-1}^{1} P_{J'}^{M'}(x)(1-x^2)^{1/2}P_J^M(x)\,\mathrm{d}x\right].\end{aligned}$$

The two cases $M' = M \pm 1$ will be calculated separately. Take $M' = M + 1$:

$$\begin{aligned}&\langle J'\, M+1\, |\cos\phi\sin\theta|\, JM\rangle \\ &\quad = \pi N_{J'}^{M+1} N_J^M \int_{-1}^{1} P_{J'}^{M+1}(x)(1-x^2)^{1/2}P_J^M(x)\,\mathrm{d}x \\ &\quad = \frac{\pi N_{J'}^{M+1} N_J^M}{2J'+1}\int_{-1}^{1}\left[(J'+M+1)(J'+M)P_{J'-1}^M\right. \\ &\qquad\qquad \left. -\,(J'-M)(J'-M+1)P_{J'+1}^M\right]P_J^M\,\mathrm{d}x\end{aligned}$$

and using orthgonality and taking $J' = J + 1$ leaves

$$\begin{aligned}&\langle J+1\, M+1\, |\cos\phi\sin\theta|\, JM\rangle \\ &\quad = \frac{\pi N_{J+1}^{M+1} N_J^M}{2J+3}(J+M+2)(J+M+1)\frac{2}{2J+1}\frac{(J+M)!}{(J-M)!} \\ &\quad = -\frac{1}{2}\left[\frac{(J+M+2)(J+M+1)}{(2J+1)(2J+3)}\right]^{1/2}.\end{aligned}$$

Now with $M' = M - 1$:

$$\begin{aligned}\langle J'\, M-1\, |\cos\phi\sin\theta|\, JM\rangle &= \pi N_{J'}^{M-1} N_J^M \int_{-1}^{1} P_{J'}^{M-1}(x)(1-x^2)^{1/2}P_J^M(x)\,\mathrm{d}x \\ &= \frac{\pi N_{J'}^{M-1} N_J^M}{2J'+1}\int_{-1}^{1}\left[P_{J'+1}^M - P_{J'-1}^M\right]P_J^M\,\mathrm{d}x\end{aligned}$$

and using orthgonality and taking $J' = J + 1$ leaves

$$\begin{aligned}\langle J+1\, M-1\, |\cos\phi\sin\theta|\, JM\rangle &= \frac{-\pi N_{J+1}^{M-1} N_J^M}{2J+3}\,\frac{2}{2J+1}\frac{(J+M)!}{(J-M)!} \\ &= \frac{1}{2}\left[\frac{(J-M+2)(J-M+1)}{(2J+1)(2J+3)}\right]^{1/2}.\end{aligned}$$

It is amazing that the two results for $M' = M \pm 1$ are so similar, yet one cannot be derived from the other (by using the hermiticity-dummy substitution method). This is possible for one index (J) but not both indices simultaneously. Thus,

$$\langle J+1\ M \pm 1 \left|\cos\phi \sin\theta\right| JM\rangle = \mp\frac{1}{2}\left[\frac{(J \pm M + 2)(J \pm M + 1)}{(2J+1)(2J+3)}\right]^{1/2}. \qquad \text{(B.1)}$$

Laser field matrix elements

The laser field matrix elements are $\langle J'M' \left|\cos^2\theta\right| JM\rangle$. Since calculation of the static field element $\langle J'M' \left|\cos\theta\right| JM\rangle$ required using the second order recurrence in J once, the laser field element requires using this recurrence relation twice. This leads to two independent elements: J is increased twice, or it is increased and then decreased for no net change. The matrix element is:

$$\begin{aligned}
&\left\langle J'M' \left|\cos^2\theta\right| JM\right\rangle \\
&\quad = N_{J'}^{M'} N_J^M \left[\int_0^{2\pi} \mathrm{e}^{-\mathrm{i}(M'-M)\phi}\,\mathrm{d}\phi\right]\left[\int_0^{\pi} P_{J'}^{M'}(\cos\theta)\cos^2\theta P_J^M(\cos\theta)\sin\theta\,\mathrm{d}\theta\right] \\
&\quad = N_{J'}^{M'} N_J^M \left[2\pi\delta_{MM'}\right]\left[\int_{-1}^{1} P_{J'}^{M'}(x)x^2 P_J^M(x)\,\mathrm{d}x\right] \\
&\left\langle J'M \left|\cos^2\theta\right| JM\right\rangle \\
&\quad = 2\pi N_{J'}^M N_J^M \frac{1}{2J'+1}\int_{-1}^{1}\left[(J'+M)P_{J'-1}^M + (J'-M+1)P_{J'+1}^M\right] xP_J^M\,\mathrm{d}x \\
&\quad = \frac{2\pi N_{J'}^M N_J^M}{2J'+1}\left\{(J'+M)\int_{-1}^{1} xP_{J'-1}^M P_J^M\,\mathrm{d}x + (J'-M+1)\int_{-1}^{1} xP_{J'+1}^M P_J^M\,\mathrm{d}x\right\} \\
&\quad = \frac{2\pi N_{J'}^M N_J^M}{2J'+1}\left\{\frac{J'+M}{2(J'-1)+1}\int_{-1}^{1}\left[(J'-1+M)P_{J'-2}^M + (J'-M)P_{J'}^M\right]P_J^M\,\mathrm{d}x\right. \\
&\qquad\quad \left. + \frac{J'-M+1}{2(J'+1)+1}\int_{-1}^{1}\left[(J'+1+M)P_{J'}^M + (J'-M+2)P_{J'+2}^M\right]P_J^M\,\mathrm{d}x\right\}.
\end{aligned}$$

One of three nonzero terms appears by using one of $J' = J$ or $J' = J \pm 2$. The latter two yield the same information. $J' = J$ could also be calculated, but this

matrix element will be determined by other means. Take $J' = J + 2$:

$$\begin{aligned}
&\left\langle J+2\ M \left|\cos^2\theta\right| JM\right\rangle \\
&\quad = \frac{2\pi N_{J+2}^M N_J^M}{2J+5}\left[\frac{(J+M+2)(J+M+1)}{2J+3}\times\frac{2}{2J+1}\frac{(J+M)!}{(J-M)!}\right] \\
&\quad = \frac{(J+M+2)!}{(2J+1)(2J+3)(2J+5)(J-M)!}\left[\frac{(2J+1)(J-M)!}{(J+M)!}\,\frac{(2J+5)(J-M+2)!}{(J+M+2)!}\right]^{1/2} \\
&\quad = \frac{1}{2J+3}\left[\frac{(J+M+1)(J+M+2)(J-M+2)(J-M+1)}{(2J+1)(2J+5)}\right]^{1/2}
\end{aligned}$$

or

$$\left\langle J+2\ M \left|\cos^2\theta\right| JM\right\rangle = \frac{1}{2J+3}\left[\frac{((J+1)^2-M^2)}{2J+1}\,\frac{((J+2)^2-M^2)}{2J+5}\right]^{1/2}.$$

The matrix element $\langle JM\,|\cos^2\theta|\,JM\rangle$ can be calculated by inserting a completeness relation and using the static field matrix element $\langle J+1\ M\,|\cos\theta|\,JM\rangle$:

$$\begin{aligned}
\left\langle JM \left|\cos^2\theta\right| JM\right\rangle &= \left\langle JM \left|\cos\theta\,\hat{\mathbf{1}}\,\cos\theta\right| JM\right\rangle \\
&= \left\langle JM \left| \cos\theta \sum_{J'M'} |J'M'\rangle\langle J'M'| \right| JM \right\rangle \\
&= \sum_{J'M'} \langle JM\,|\cos\theta|\,J'M'\rangle\,\langle J'M'\,|\cos\theta|\,JM\rangle\,.
\end{aligned}$$

The sum has two nonzero terms: when $J' = J \pm 1$ and $M' = M$. Each term is the square of the matrix element (B.2b); the first term is from $J' = J + 1$ and the second from $J' = J - 1$:

$$\left\langle JM \left|\cos^2\theta\right| JM\right\rangle = \frac{(J+1)^2-M^2}{(2J+1)(2J+3)} + \frac{J^2-M^2}{(2J-1)(2J+1)}.$$

Note that a slight complication can be overlooked. If $J = 0$ one must neglect the $J' = J - 1$ term since -1 is not an allowed value for the quantum number J. Similarly, if $M = \pm J$ then the $J' = J - 1$ term should be omitted since $|M| > J$ is

not allowed. But in those cases the offending term evaluates to zero, so no special cases need to be cited.

The nonzero matrix element expressions are (for allowed combinations of J and M):

$$\left\langle JM \left| \boldsymbol{j}^2 \right| JM \right\rangle = J(J+1) \tag{B.2a}$$

$$\langle J+1\ M \left|\cos\theta\right| JM\rangle = \left[\frac{(J+1)^2 - M^2}{(2J+1)(2J+3)}\right]^{1/2} \tag{B.2b}$$

$$\langle J+1\ M\pm 1 \left|\cos\phi\sin\theta\right| JM\rangle = \mp\frac{1}{2}\left[\frac{(J\pm M+2)(J\pm M+1)}{(2J+1)(2J+3)}\right]^{1/2}$$

$$\left\langle JM \left|\cos^2\theta\right| JM\right\rangle = \frac{1}{2J+1}\left[\frac{J^2-M^2}{2J-1} + \frac{(J+1)^2-M^2}{2J+3}\right] \tag{B.2c}$$

$$\left\langle J+2\ M \left|\cos^2\theta\right| JM\right\rangle = \frac{1}{2J+3}\left[\frac{((J+1)^2-M^2)}{2J+1}\frac{((J+2)^2-M^2)}{2J+5}\right]^{1/2}.$$

B.2 Symmetrized Spherical Harmonics

There are several different convenient basis sets to use for the linear rotor in fields problem. Spherical harmonics $Y_J^M(\theta,\phi)$ are the first choice, since the matrix elements are easy to calculate, as are the functions themselves. When the fields are collinear, M is a good quantum number and a basis can be restricted to spherical harmonics with given common M. When the fields are tilted (M is not fixed), one could use all spherical harmonics as a basis, but that would be roughly twice as large as necessary.

The basis can be reduced by using symmetry. The tilted fields Hamiltonian for linear rotors always has reflection plane XZ symmetry in the lab frame. The symmetry operator σ_{XZ} ($\phi \to -\phi, \theta \to \theta$) commutes with all linear rotor Hamiltonians H used here and has two eigenvalues, $p = \pm 1$. Each energy eigenfunction can be labeled with the parity p with respect to reflection. Since the Hamiltonian

does not mix basis states of different parity, only basis states of common p need be used to set up the Hamiltonian matrix. Basis size is cut by half over using all spherical harmonics, so the matrix diagonalization is faster. Also, in some applications (such as nearest neighbor spacing distributions) all states must belong to the same symmetry class, *i.e.* they all transform the same way under the symmetry operations that leave the Hamiltonian invariant.

The symmetrized basis is constructed as follows. Since

$$\sigma_{XZ} Y_J^M(\theta,\phi) = Y_J^M(\theta,-\phi) = Y_J^{M^*}(\theta,\phi) = (-1)^M Y_J^M(\theta,\phi),$$

define new kets

$$|JMp\rangle := [2(1+\delta_{M0})]^{-1/2} \left(|JM\rangle + p(-1)^M \, |J \, -M\rangle \right) \tag{B.3}$$

with the provision $J \geq M \geq 0$, and when $M = 0$, only $p = +1$ is allowed. These states are orthonormal. Symmetric (even) states have $p = 1$, and antisymmetric (odd) states have $p = -1$. The formation used here should be familiar; the symmetrized states are the real and imaginary parts of the spherical harmonics and are used to depict $s, p, d, f, \ldots$ orbitals of one electron atoms as purely real functions:

$$\langle \phi\, \theta | JMp \rangle = \begin{cases} \frac{(-1)^M}{\sqrt{\pi}} \mathcal{P}_J^M(\cos\theta) \cos M\phi & , \quad M > 0, p = 1 \\ \mathrm{i}\frac{(-1)^M}{\sqrt{\pi}} \mathcal{P}_J^M(\cos\theta) \sin M\phi & , \quad M > 0, p = -1 \\ \frac{1}{\sqrt{2\pi}} \mathcal{P}_J^M(\cos\theta) & , \quad M = 0, p = 1. \end{cases}$$

The Hamiltonian matrix elements corresponding to ϕ-independent terms are not different in this basis. The only ϕ-dependent term (1.12) is $\sin\beta \sin\theta \cos\phi$ from the static electric field X component interacting with the permanent dipole. All nonzero linear rotor matrix elements are shown below for completeness. There are three cases for $\sin\theta\cos\phi$ since the basis definition changes from $M = 0$ to $M > 0$.

The linear rotor Hamiltonian matrix elements in the symmetrized basis (B.3) are

$$\begin{aligned}
\left\langle J'M'p' \left| j^2 \right| JMp \right\rangle &= J(J+1)\delta_{J'J}\delta_{M'M}\delta_{p'p} \\
\left\langle J'M'p' \left| \cos\theta \right| JMp \right\rangle &= \left\langle J'M' \left| \cos\theta \right| JM \right\rangle \delta_{p'p} \\
\left\langle J'M'p' \left| \cos^2\theta \right| JMp \right\rangle &= \left\langle J'M' \left| \cos^2\theta \right| JM \right\rangle \delta_{p'p} \\
\left\langle J+1\, M'p' \left| \sin\theta\cos\phi \right| JMp \right\rangle &= \\
= \begin{cases} \left\langle J+1\, M' \left| \sin\theta\cos\phi \right| JM \right\rangle \delta_{p'p} & , \quad M'>0, M>0 \\ \sqrt{2}\left\langle J+1\, M' \left| \sin\theta\cos\phi \right| JM \right\rangle \delta_{p'p} & , \quad M'=1(0), M=0(1), p(p')=1. \end{cases}
\end{aligned}$$

All of the matrix elements in the symmetrized basis are in terms of the matrix elements in the spherical harmonics basis. This is how they are programmed.

B.3 Matrix Elements in Symmetric Top Basis

Matrix elements of the various symmetric and asymmetric rotor in fields Hamiltonians in the symmetric top basis $|JMK\rangle$ are easy to calculate. First the kinetic energy matrix elements are derived, followed by the potential energy matrix elements using the Wigner-Eckart theorem.

The kinetic energy matrix elements are widely derived in angular momentum texts. The free asymmetric rotor Hamiltonian is Equation (1.4),

$$\begin{aligned}
T &= AJ_y^2 + BJ_z^2 + CJ_x^2 \\
T &= \frac{1}{2}(A+C)\boldsymbol{J}^2 + \frac{1}{2}(A-C)\left[J_y^2 + \kappa J_z^2 - J_x^2\right]
\end{aligned} \tag{B.4}$$

with the asymmetry parameter $\kappa = \frac{2B-(A+C)}{A-C}$ and $T(\kappa) := J_y^2 + \kappa J_z^2 - J_x^2$ is used below. (Recall that we use a peculiar rotational constant convention described in

Section 1.2.) We will calculate matrix elements of the squared angular momentum components and then piece together the full kinetic energy matrix elements.

The easiest way is to recall the ladder operator approach to angular momentum theory. In the molecular frame, the ladder operators $J^{\pm} = J_x \pm \mathrm{i}J_y$ act on symmetric top kets as [7, §3.4]

$$\begin{aligned} J^{\pm} \left|JMK\right\rangle &= \sqrt{(J \pm K)(J \mp K + 1)} \left|JMK \mp 1\right\rangle \\ &= \sqrt{J(J+1) - K(K \mp 1)} \left|JMK \mp 1\right\rangle \end{aligned}$$

where J^+ and J^- are actually the *lowering* and *raising* operators in the molecular frame, changing the eigenstate within a J-block by decrementing and incrementing K. Since $J_x = \frac{1}{2}(J^+ + J^-)$ and $J_y = \frac{1}{2\mathrm{i}}(J^+ - J^-)$,

$$\begin{aligned} J_x^2 &= \frac{1}{4}\left(J^{+^2} + J^{-^2} + J^+J^- + J^-J^+\right) \\ J_y^2 &= -\frac{1}{4}\left(J^{+^2} + J^{-^2} - J + J^- - J^-J^+\right). \end{aligned}$$

The free asymmetric rotor selection rules $\Delta J = 0, \Delta K = 0, \pm 2$ follow immediately, since J^{+^2} lowers K by two, J^{-^2} raises K by two, and J^+J^-, J^-J^+ do not change K. The matrix elements of J_x^2 are

$$\begin{aligned} \left\langle JK \pm 2 \left| J_x^2 \right| JK \right\rangle &= \frac{1}{4}\sqrt{J(J+1) - K(K \pm 1)}\sqrt{J(J+1) - (K \pm 1)(K \pm 2)} \\ \left\langle JK \left| J_x^2 \right| JK \right\rangle &= \frac{1}{2}J(J+1) - \frac{1}{2}K^2. \end{aligned}$$

The matrix elements of J_y^2 are

$$\begin{aligned} \left\langle JK \pm 2 \left| J_y^2 \right| JK \right\rangle &= -\frac{1}{4}\sqrt{J(J+1) - K(K \pm 1)}\sqrt{J(J+1) - (K \pm 1)(K \pm 2)} \\ \left\langle JK \left| J_y^2 \right| JK \right\rangle &= \frac{1}{2}J(J+1) - \frac{1}{2}K^2. \end{aligned}$$

Finally, J_z^2 has the simplest nonzero matrix element with selection rule $\Delta J = 0, \Delta K = 0$:

$$\left\langle JK \left| J_z^2 \right| JK \right\rangle = K^2.$$

Note that when summing these matrix elements $\boldsymbol{J}^2 = J_x^2 + J_y^2 + J_z^2$ as in Equation (B.4), the $\Delta K = \pm 2$ elements exactly cancel. Only the diagonal matrix element is nonzero, $\langle JK \left|\boldsymbol{J}^2\right| JK\rangle = J(J+1)$, identical to a linear rotor. This is the first part of the free asymmetric rotor kinetic energy.

The second part of the asymmetric rotor kinetic energy, $T(\kappa)$, has $\Delta K = 0, \pm 2$ nonzero matrix elements pieced together from the above squared angular momentum component matrix elements:

$$\langle JK \pm 2 \left|T(\kappa)\right| JK\rangle = -\frac{1}{2}\sqrt{J(J+1) - K(K \pm 1)}\sqrt{J(J+1) - (K \pm 1)(K \pm 2)}$$

$$\langle JK \left|T(\kappa)\right| JK\rangle = \kappa K^2$$

Recall that we use the dimensionless kinetic energy $T/B\hbar^2$, so dimensionless rotational constants $a := A/B$, $c := C/B$ are used. The full kinetic energy matrix elements, combining the first and second parts of Equation (B.4), are

$$\langle JK \pm 2 \left|T\right| JK\rangle = \frac{1}{4}(c-a)\sqrt{J(J+1) - K(K \pm 1)} \times \sqrt{J(J+1) - (K \pm 1)(K \pm 2)} \tag{B.5}$$

$$\langle JK \left|T\right| JK\rangle = \frac{1}{2}(a+c)J(J+1) + \frac{1}{2}(a-c)\kappa K^2. \tag{B.6}$$

The potential energy matrix elements are derived using the Wigner-Eckart theorem, which separates the matrix element of any function in the rotation matrix (1.7) into one dynamic and two geometric pieces.

Recall that the molecular frame is xyz, and the lab frame is XYZ. First rank irreducible spherical tensor (ladder) operators, also known as vector operators, in the lab frame are $\mathsf{c}_\mp = c_X \mp \mathsf{i}c_Y$, and in the molecular frame are $\mathsf{c}^\pm = \mathsf{c}_x \pm \mathsf{i}\mathsf{c}_y$. Whatever direction cosine matrix element you want is formed by

$$\langle J'M'K' \left|\mathsf{C}_{iI}\right| JMK\rangle = \langle J' \left|\left|\mathsf{C}\right|\right| J\rangle \langle J'K' \left|\mathsf{c}_i\right| JK\rangle \langle J'M' \left|\mathsf{c}_I\right| JM\rangle \tag{B.7}$$

Table B.1: Rotation matrix C elements in symmetric top basis, as reduced by the Wigner-Eckart theorem. Compare to Kroto [7, Table 4.1]. (The $J' = J - 1$ column is redundant.) The molecular frame is xyz, and the lab frame is XYZ. First rank spherical tensor ladder operators in the lab frame are $\mathsf{c}_\mp = c_X \mp \mathsf{i}c_Y$, and in the molecular frame are $\mathsf{c}^\pm = \mathsf{c}_x \pm \mathsf{i}\mathsf{c}_y$.

	$J' = J + 1$	$J' = J$
$\langle J' \Vert \mathsf{C} \Vert J \rangle$	$\frac{1}{(J+1)\sqrt{(2J+3)(2J+1)}}$	$\frac{1}{J(J+1)}$
$\langle J'K \vert \mathsf{c}_z \vert JK \rangle$	$\sqrt{(J+K+1)(J-K+1)}$	K
$\langle J'K \mp 1 \vert \mathsf{c}^\pm \vert JK \rangle$	$\pm\sqrt{(J\mp K+2)(J\mp K+1)}$	$\sqrt{(J\mp K+1)(J\pm K)}$
$\langle J'M \vert \mathsf{c}_Z \vert JM \rangle$	$\sqrt{(J+M+1)(J-M+1)}$	M
$\langle J'M \mp 1 \vert \mathsf{c}_\mp \vert JM \rangle$	$\pm\sqrt{(J\mp M+2)(J\mp M+1)}$	$\sqrt{(J\mp M+1)(J\pm M)}$

using factors read from Table B.1.

Thus the matrix elements, in the symmetric top basis, of any element of C are found by multiplying the correct three terms in Table B.1. The table implies all quantum numbers change by ± 1 or 0 under perturbations listed in the rotation matrix C (1.7). For instance, the static electric field contributes the term $\cos\theta = \mathsf{C}_{zZ}$ to the Hamiltonian, and a diagonal matrix element

$$\langle JMK \vert \cos\theta \vert JMK \rangle = \langle J \Vert \mathsf{C} \Vert J \rangle \langle JK \vert \mathsf{c}_z \vert JK \rangle \langle JM \vert \mathsf{c}_Z \vert JM \rangle$$

which becomes

$$\langle JMK \vert \cos\theta \vert JMK \rangle = \frac{1}{J(J+1)} KM.$$

For the Hamiltonians used here (Table 1.3) we need matrix elements of three functions in the rotation matrix: $\cos\theta = \mathsf{C}_{zZ}$, $\sin\theta\cos\phi = \mathsf{C}_{zX}$, and $\sin\theta\sin\chi =$

C_{yZ}. The results for all nonzero matrix elements derived in this way are:

$$\langle J+1\, MK\, |\cos\theta|\, JMK\rangle = \frac{\sqrt{(J+K+1)(J-K+1)(J+M+1)(J-M+1)}}{(J+1)\sqrt{(2J+3)(2J+1)}} \tag{B.8}$$

$$\langle JMK\, |\cos\theta|\, JMK\rangle = \frac{KM}{J(J+1)} \tag{B.9}$$

$$\langle J+1\, M\pm 1\, K\, |\sin\theta\cos\phi|\, JMK\rangle = \mp\frac{\sqrt{(J\pm M+2)(J\pm M+1)(J+K+1)(J-K+1)}}{2(J+1)\sqrt{(2J+3)(2J+1)}}$$

$$\langle JM\pm 1\, K\, |\sin\theta\cos\phi|\, JMK\rangle = \frac{K\sqrt{(J\pm M+1)(J\mp M)}}{2J(J+1)}$$

$$\langle J+1\, MK\pm 1\, |\sin\theta\sin\chi|\, JMK\rangle = \frac{\sqrt{(J\pm K+2)(J\pm K+1)(J+M+1)(J-M+1)}}{2\mathrm{i}(J+1)\sqrt{(2J+3)(2J+1)}}$$

$$\langle JMK\pm 1\, |\sin\theta\sin\chi|\, JMK\rangle = \mp\frac{M\sqrt{(J\pm K+1)(J\mp K)}}{2\mathrm{i}J(J+1)}.$$

These basic results are used to build up the matrix elements for squares of functions in the rotation matrix. The squares are needed for laser terms in the Hamiltonians, namely, $\cos^2\theta$ and $\sin^2\theta\sin^2\chi$. Just by inserting a completeness relation, an abstract expression for the desired matrix element appears. For instance, the $\cos^2\theta$ matrix element can be written as

$$\left\langle J'M'K'\left|\cos^2\theta\right|JMK\right\rangle = \sum_{''}\left\langle J'M'K'\,|\cos\theta|\,J''M''K''\right\rangle\left\langle J''M''K''\,|\cos\theta|\,JMK\right\rangle. \tag{B.10}$$

The factors in the sum are known from Equations (B.8) and (B.9). Using the

selection rules for these building blocks, you can find three possible "paths" that lead to nonzero matrix elements. The selection rules for $\cos^2\theta$ are $\Delta J = 0, \pm 1, \pm 2$, $\Delta M = 0$, $\Delta K = 0$. For a term that changes K as well as J, such as $\sin^2\theta \sin^2\chi$, the nonzero terms are plentiful and have several terms each. In this case, an equation like (B.10) is explicitly programmed by selection rules picking the right path over sums of pair-multiplied underlying functions.

B.4 Symmetrized Asymmetric Rotor Basis

Using the full complement of symmetric rotor basis functions (fixed M) for the asymmetric rotor is excessive. When the asymmetric rotor is free, the Hamiltonian is invariant under the operations of the D_2 point group. These operations also do not change the Hamiltonian of an asymmetric rotor in the laser field. When an asymmetric rotor is immersed in collinear static and laser fields, the Hamiltonian is invariant only under the operations of the C_2 point group. We want to develop symmetrized basis sets in these two cases to reduce the size of the matrix diagonalizations. The symmetrized basis for the totally symmetric representation is coded in each case.

The D_2 point group (in the molecular frame) consists of the identity and two-fold rotation about each molecular axis. The coordinate changes corresponding to each operation are [14, Ch. 6]

$$\begin{aligned}
C_2(x): &\quad \phi \to \pi + \phi & \theta \to \pi - \theta & \quad \chi \to -\chi \\
C_2(y): &\quad \phi \to \pi + \phi & \theta \to \pi - \theta & \quad \chi \to \pi - \chi \\
C_2(z): &\quad \phi \to \phi & \theta \to \theta & \quad \chi \to \pi + \chi
\end{aligned}$$

None of these operations change the asymmetric rotor kinetic energy Hamiltonian:

they just rotate angular momentum component J_i to $-J_i$, which is squared for the kinetic energy $AJ_y^2 + BJ_z^2 + CJ_x^2$. Likewise, the laser potential energy terms $\sin^2\theta \sin^2\chi$ and $\cos^2\theta$ are invariant.

The symmetric rotor states are changed:

$$C_2(x)\,|JMK\rangle = (-1)^{-J}\,|JM\ -K\rangle$$
$$C_2(y)\,|JMK\rangle = (-1)^{-J-K}\,|JM\ -K\rangle$$
$$C_2(z)\,|JMK\rangle = (-1)^{K}\,|JMK\rangle$$

Since the symmetric rotor kets are not eigenkets of x and y two-fold rotation, but they transform $K \rightarrow -K$, the symmetrized basis is defined as

$$|JMKs\rangle := [2(1+\delta_{K0})]^{-1/2}\,(|JMK\rangle + s\,|JM\ -K\rangle)\,, \tag{B.11}$$

where $K \geq 0$ for $s = 1$ and $K > 0$ for $s = -1$. Note the similarity to the symmetrized spherical harmonics Equation (B.3).

This is a properly symmetrized basis, since they are eigenkets of all D_2 operations:

$$C_2(x)\,|JMKs\rangle = (-1)^{-J}s\,|JMKs\rangle$$
$$C_2(y)\,|JMKs\rangle = (-1)^{-J-K}s\,|JMKs\rangle$$
$$C_2(z)\,|JMKs\rangle = (-1)^{K}\,|JMKs\rangle\,.$$

However, the symmetry is a little tricky. The values of (J, K, s) being (even/odd, even/odd, $+1/-1$) in any of eight combinations determine which of the four D_2 point group irreducible representations the state $|JMKs\rangle$ belongs to. The answers are summarized in the extended character table of the D_2 point group, Table B.2. The right hand columns show how the symmetrized basis quantum numbers

Table B.2: Chacter table of D_2 point group. Extended to include correspondence between asymmetric rotor symmetrized basis quantum numbers and D_2 irreducible representations.

D_2	E	$C_2(x)$	$C_2(z)$	$C_2(y)$	J	K	s
A	1	1	1	1	odd even	even even	-1 +1
B_x	1	1	-1	-1	odd even	odd odd	-1 +1
B_z	1	-1	1	-1	odd even	even even	+1 -1
B_y	1	-1	-1	1	odd even	odd odd	+1 -1

correspond to each of the irreducible representations. For instance, if (J, K, s) are (odd, even, -1), that symmetrized basis state belongs to the totally symmetric A irreducible representation. However, symmetrized basis states with (J, K, s) as (even, even, $+1$) also belong to the A representation. When only one symmetry class of eigenstates of these Hamiltonians is desired, then pick symmetric rotor basis states with values of J, K, s corresponding to the desired symmetry class, according to the table.

When an asymmetric rotor is in collinear laser and static fields, the relevant symmetry group is reduced to C_2, with $C_2(z)$ the remaining symmetry operation in the molecular frame. The symmetric rotor basis is already symmetrized with respect to the C_2 operations; the two symmetry classes A, B are separated by K being even or odd (*i.e.* no matter the J value, and s is not needed). The totally symmetric A representation contains all of the K even symmetric rotor states.

Appendix C

Propagation Derivations

C.1 Formal Correspondance of Quantum and Classical Dynamics

Gray & Verosky [47] provide the basic ideas of the formal classical-quantum correspondence and of symplectic integration used here. The time dependent Schrödinger equation is

$$\mathrm{i}\hbar \frac{\mathrm{d}}{\mathrm{d}t} |\psi(t)\rangle = \hat{H}(t) |\psi(t)\rangle \tag{C.1}$$

The Hamiltonian is generally time dependent, so we need to numerically solve the TDSE. As a first step we reduce the dimensionless TDSE (3.1) to a coupled set of ordinary differential equations. The time-dependent state ket written in the spectral representation $|\psi(t)\rangle = \sum_n c_n(t) |n\rangle$ facilitates this. Noting the basis kets are time independent,

$$\mathrm{i}\hbar \sum_n \dot{c}_n(t) |n\rangle = \sum_n c_n(t) \hat{H}(t) |n\rangle .$$

The matrix element of this equation with $\langle m |$ yields a new form of the TDSE,

$$\mathrm{i}\hbar \dot{c}_m(t) = \sum_n H_{mn} c_m(t) \tag{C.2a}$$

$$\mathrm{i}\hbar \dot{\boldsymbol{c}}(t) = \mathsf{H}\boldsymbol{c}(t). \tag{C.2b}$$

The former Equation (C.2a) is explicitly in terms of individual coefficents c_m and dimensionless hamiltonian matrix elements H_{mn}. The latter Equation (C.2b) has the same content, but explicitly shows how the TDSE has been reduced to matrix-vector multiplication. Propagating wave functions using these equations is convenient since Hamiltonian matrix elements in the free rotor eigenbasis are simple

analytical results previously needed when calculating correlation diagrams; formulas are in Appendix B. (The time dependence in the problems treated here is a simple envelope factor of the model field terms, a gaussian-attenuated laser pulse.) Equation (C.2a) is just a set of coupled homogeneous ordinary differential equations in c_m, which could be numerically integrated by standard methods such as fourth-order Runge-Kutta. [46]

However, we use a method called *symplectic integration*, which is specially tailored for integrating classical trajectories. Since we do quantum propagation, first we show a formal equivalence between quantum and classical dynamics. [47] Then symplectic integration is used to accurately calculate "classical trajectories" and then translate them back to quantum wave functions.

Given quantum superposition coefficients $\boldsymbol{c}(t)$ and Hamiltonian matrix H, define position $\boldsymbol{q}$, momentum $\boldsymbol{p}$, and scalar function $H(\boldsymbol{q},\boldsymbol{p},t)$,

$$\begin{aligned}
\boldsymbol{q}(t) &:= \sqrt{2\hbar}\,\mathrm{Re}\,[\boldsymbol{c}(t)] \\
\boldsymbol{p}(t) &:= \sqrt{2\hbar}\;\mathrm{Im}\,[\boldsymbol{c}(t)] \\
H(\boldsymbol{q},\boldsymbol{p},t) &:= \frac{1}{2\hbar}(\boldsymbol{q}^T - \mathrm{i}\boldsymbol{p}^T)\mathsf{H}(\boldsymbol{q}+\mathrm{i}\boldsymbol{p}) \equiv \boldsymbol{c}^\dagger(t)\mathsf{H}\boldsymbol{c}(t) \equiv \langle\hat{H}\rangle.
\end{aligned}$$

We now show that Hamilton's equations for these classical variables

$$\dot{\boldsymbol{q}} = \frac{\partial H}{\partial p}, \qquad\qquad \dot{\boldsymbol{p}} = -\frac{\partial H}{\partial q},$$

is equivalent to Schrödinger's equation (C.2b). Substitute, differentiate,* and find

*Differentiating the vector and matrix products is easy; just treat $\boldsymbol{q}^T\mathsf{H}\boldsymbol{q}$ as quadratic in $\boldsymbol{q}$, for example. You can also use subscript-summation notation and find the same result.

$$H = \frac{1}{2\hbar}\left(\boldsymbol{q}^T \mathsf{H}\boldsymbol{q} + \boldsymbol{p}^T \mathsf{H}\boldsymbol{p} + \mathrm{i}\boldsymbol{q}^T \mathsf{H}\boldsymbol{p} - \mathrm{i}\boldsymbol{p}^T \mathsf{H}\boldsymbol{q}\right)$$

$$\dot{\boldsymbol{q}} = \frac{\partial H}{\partial p} = \frac{1}{2\hbar}(2\mathsf{H}\boldsymbol{p} + \mathrm{i}\mathsf{H}\boldsymbol{q} - \mathrm{i}\mathsf{H}\boldsymbol{q}) = \mathsf{H}\boldsymbol{p}/\hbar \tag{C.3a}$$

$$-\dot{\boldsymbol{p}} = \frac{\partial H}{\partial q} = \frac{1}{2\hbar}(2\mathsf{H}\boldsymbol{q} + \mathrm{i}\mathsf{H}\boldsymbol{p} - \mathrm{i}\mathsf{H}\boldsymbol{p}) = \mathsf{H}\boldsymbol{q}/\hbar. \tag{C.3b}$$

Testing Equation (C.2b) verifies

$$\mathrm{i}\hbar\dot{\boldsymbol{c}} = \frac{\mathrm{i}\hbar}{\sqrt{2\hbar}}(\dot{\boldsymbol{q}} + \mathrm{i}\dot{\boldsymbol{p}}) = \frac{1}{\sqrt{2\hbar}}\mathsf{H}(\boldsymbol{q} + \mathrm{i}\boldsymbol{p}) = \mathsf{H}\boldsymbol{c}.$$

The TDSE in vector form has been recovered. All steps here are reversible, so equivalency between quantum (Schrödinger's equation) and classical (Hamilton's equations) dynamics given these definitions is proved. We translate our quantum wavefunctions into classical positions and momenta and use classical symplectic integration to propagate wavefunctions.

C.2 Symplectic Integrators

Symplectic integration is a numerical integration technique built specially for calculating classical trajectories. It automatically conserves the Poincaré integral invariants. [48, §8.3] We know analytically that any classical canonical transformation, such as classical time evolution, must preserve these integral invariants. Obviously, it is advantageous to propagate classical trajectories with an algorithm that guarantees their invariance. Standard algorithms, such as Runge-Kutta, do not conserve the integral invariants.

Recall that the Poincaré invariants are a hierarchy of quantities, properties of all trajectories taken together, that are rigorously conserved in Hamiltonian

systems. The last invariant in the hierarchy is the best known: phase space volume, conservation of which is known as Liouville's theorem.

To start, let's employ symplectic notation for Hamilton's equations. For N degrees of freedom, define $\boldsymbol{z} := (\boldsymbol{q}, \boldsymbol{p})$ as a $2N$-vector, but for the present formalism we can use just one degree of freedom $z = (q, p)$. Then Hamilton's equations can be written using the Poisson bracket

$$\dot{z} = \{z, H(z)\} := \frac{\partial z}{\partial q}\frac{\partial H}{\partial p} - \frac{\partial z}{\partial p}\frac{\partial H}{\partial q}.$$

Further, the Poisson bracket can be thought of as a differential operator D_H, called the *Liouvillian*,

$$D_H z := \left[\frac{\partial H}{\partial p}\frac{\partial}{\partial q} - \frac{\partial H}{\partial q}\frac{\partial}{\partial p}\right] z \equiv \left[\dot{q}\frac{\partial}{\partial q} + \dot{p}\frac{\partial}{\partial p}\right] z \equiv \{\cdot, H\} z. \tag{C.4}$$

Classical mechanics is now cast in terms of two operators; let us call them A and B for the following abstract treatment, with $A = \frac{\partial H}{\partial p}\frac{\partial}{\partial q}$ and $B = -\frac{\partial H}{\partial q}\frac{\partial}{\partial p}$.

Of course, a formal solution of Hamilton's equation (C.4) in terms of D_H is $z(t) = \exp(tD_H)z(0) = \exp[t(A + B)]z(0)$ (assuming the Hamiltonian is time independent). This has exactly the same interpretation, and is the classical counterpart of, the familiar quantum propagator $\hat{U}(t, 0) = \exp(-it\hat{H}/\hbar)$. In both cases, the exponential operator propagates the state function at time zero into the state function at time t.

We know how A and B individually propagate the state, since their exponentials are defined by Taylor series. For example, a propagator term e^{tA} is approximated by $1 + tA = 1 + \frac{\partial H}{\partial p}\frac{\partial}{\partial q}$. Each term (except zeroth order) in the operator expansion first differentiates z with respect to q. Only the position component survives differentiation, which is then increased by $t\frac{\partial H}{\partial p}$. The propagator e^{tA} propagates the position q by time t but does not affect the momentum p since it does not remain

after differentiation with respect to q. Using the classical-quantum correspondence outlined above, classical propagation by e^{tA} corresponds to multiplying the quantum Hamiltonian matrix and "momentum" vector for the position increment, according to Equation (C.3a).

However, propagating the full Hamiltonian $\mathrm{e}^{t(A+B)}$ is in general intractable since A and B do not commute and the exponential cannot be factored. However, a simple approximation is widely known (lowest order Trotter factorization) and derived in Appendix C.3:

$$D_{H,2}(t) = \mathrm{e}^{At/2}\mathrm{e}^{Bt}\mathrm{e}^{At/2}. \tag{C.5}$$

This propagator is second-order in the time step. It is interpreted as follows, as an operator from right to left: first advance the position by a half time step, then the momenta by a full time step, then position by another half time step. This is a simple idea dressed in operator finery. This algorithm is also known as *position Verlet* [49] (the same idea as *velocity Verlet*, with A and B switched) and *symplectic leapfrog*. [47]

Via the classical-quantum correspondence, classical symplectic integration corresponds to repeated matrix-vector multiplications and vector additions.

The fact $D_{H,2}$ is actually a symplectic transformation is proved in Appendix C.4. I also prove that the simple Euler method is not symplectic. The key element of propagator (C.5) that guarantees conservation of the integral invariants is how the momentum increment in each symplectic integration step depends on the position calculated in the first half time step.

Second-order symplectic integration can be used for time-dependent Hamiltonians. The algorithm is almost the same as that for time-independent Hamiltonians. The formulas are derived in Appendix C.5.

The integration routine should also obey time reversal symmetry, from which we see no odd order symplectic integration routines exist. By time reversal symmetry we mean that after propagating a system by time t, further propagating by time $-t$ returns the system to its original state. This is another classical property, in addition to preservation of the Poincaré invariants, that the integration routine satisfies. The symmetric construction guarantees this.

C.3 Deriviation of the SI2 Coefficients

Yoshida [50] nicely frames the problem: for desired order n and number of steps k, an approximation to

$$\mathrm{e}^{t(A+B)} = \prod_{i=1}^{k} \mathrm{e}^{c_i t A} \mathrm{e}^{d_i t B} + O(t^{n+1}) \tag{C.6}$$

can be found by determining coefficients $\{c_i, d_i\}, i = 1, \ldots, k$.

First we want a second-order propagator with two steps (each operator A and B can act twice). That is, solve for c_1, d_1, c_2, d_2 that satisfy

$$\mathrm{e}^{t(A+B)} = \mathrm{e}^{c_1 t A} \mathrm{e}^{d_1 t B} \mathrm{e}^{c_2 t A} \mathrm{e}^{d_2 t B} + O(t^3). \tag{C.7}$$

Now expand each exponential in a second-order Taylor series (which defines the

exponential of an operator) and multiply the result:

$$
\begin{aligned}
1 + t(A+B) + \frac{1}{2}t^2(A+B)^2 = & \\
&= (1 + c_1 tA + \frac{c_1^2}{2}t^2A^2)(1 + d_1 tB + \frac{d_1^2}{2}t^2B^2) \\
&\quad + (1 + c_2 tA + \frac{c_2^2}{2}t^2A^2)(1 + d_2 tB + \frac{d_2^2}{2}t^2B^2) + O(t^3) \\
&= 1 + t(c_1A + d_1B + c_2A + d_2B) \\
&\quad + \frac{t^2}{2}(c_1^2A^2 + d_1^2B^2 + c_2^2A^2 + d_2^2B^2 + 2c_1d_1AB + 2d_1c_2BA \\
&\qquad + 2d_1d_2B^2 + 2c_1c_2A^2 + 2c_1d_2AB + 2c_2d_2AB) + O(t^3) \\
&= 1 + t[(c_1 + c_2)A + (d_1 + d_2)B] \\
&\quad + \frac{t^2}{2}[(c_1 + c_2)^2A^2 + (d_1 + d_2)^2B^2 + 2(c_1d_1 + c_1d_2 + c_2d_2)AB \\
&\qquad + 2d_1c_2BA] + O(t^3).
\end{aligned}
$$

Matching operator coefficients in terms of same order in t on left and right provides restricting conditions on these coefficients. To first order, $c_1+c_2 = d_1+d_2 = 1$ must hold. To second order, two additional conditions must hold: $c_1d_1 + c_1d_2 + c_2d_2 = 1/2$, and $d_1c_2 = 1/2$. Actually, the last of these four constraints is redundant, since the first three can be combined to create the fourth. Thus there are four unknowns and three constraints, leaving one coefficient arbitrary—choose $d_2 = 0$. Then the coefficients that define this two step, second order propagator are $c_1 = c_2 = 1/2, d_1 = 1, d_2 = 0$.

C.4 Proof that the Integrators are Symplectic

This propagator is symplectic—it automatically preserves the Poincaré invariants. As an example, consider the ultimate invariant, phase space volume. It is proved invariant if the Jacobian determinant of the coordinate change represented by time

evolution is one, since the Jacobian determinant is the ratio of volumes contained by infinitesimal boxes in two different coordinate systems. I use the quantum notation from the classical-quantum correspondence of Equation (C.3),

$$\dot{\boldsymbol{q}} = \frac{\partial H}{\partial p} = \mathsf{H}\boldsymbol{p}/\hbar$$
$$-\dot{\boldsymbol{p}} = \frac{\partial H}{\partial q} = \mathsf{H}\boldsymbol{q}/\hbar,$$

where H is the quantum Hamiltonian matrix and $\boldsymbol{q}, \boldsymbol{p}$ are valid classical position and momenta. Using shorthand $x = \mathsf{H}t/\hbar$, one sub-step of a symplectic integration step is written as

$$\boldsymbol{q} = \boldsymbol{q}_0 + cx$$
$$\boldsymbol{p} = \boldsymbol{p}_0 - dx\boldsymbol{q} = \boldsymbol{p}_0 - dxq_0 - cdx^2\boldsymbol{p}_0.$$

In matrix notation, this reads as a simple linear transformation

$$\begin{pmatrix} \boldsymbol{q} \\ \boldsymbol{p} \end{pmatrix} = \begin{pmatrix} 1 & cx \\ -dx & 1 - cdx^2 \end{pmatrix} \begin{pmatrix} \boldsymbol{q}_0 \\ \boldsymbol{p}_0 \end{pmatrix}$$

with determinant equal to one. Thus the phase space volume is conserved under the symplectic integration step. Using exactly the same notation but limited to any subset of the degrees of freedom proves conservation of the other Poincaré invariants, which are the volume element projected onto any of the $2, 4, 6, \ldots, 2n-2$ hyperplanes of $2n$ dimensional phase space. They key facet that guarantees invariance is how the momentum increment in each symplectic integration step depends on the position calculated in the same step.

In contradistinction, the simple Euler method appears as

$$\begin{pmatrix} \boldsymbol{q} \\ \boldsymbol{p} \end{pmatrix} = \begin{pmatrix} 1 & cx \\ -dx & 1 \end{pmatrix} \begin{pmatrix} \boldsymbol{q}_0 \\ \boldsymbol{p}_0 \end{pmatrix},$$

whose transformation matrix has nonunity Jacobian determinant. One should expect inaccuracies, perhaps only after long times, when using such numerical integration algorithms.

C.5 Time-dependent Hamiltonians

The above derivation assumed the Hamiltonian was time independent, leaving pulsed laser fields from consideration. However, a very simple trick common in classical mechanics allows easy quantum propagation with time-dependent Hamiltonians. This was reported by Sanz-Serna and Portillo [51] in different notation.

The time-independent Hamiltonian formal solution is $z(t) = \mathrm{e}^{tD_H} z(0)$, but this is not valid for a time-dependent Hamiltonian. Using this proposed solution with $H = H(t)$ in the equation of motion (C.4) yields

$$\begin{aligned} \dot{z}(t) &= \mathrm{e}^{tD_H} \left(D_H + t\dot{D}_H \right) z(0) \\ &= D_H z(t) + t\mathrm{e}^{tD_H} \dot{D}_H z(0) \end{aligned}$$

which is certainly not the original differential equation.

The classical trick is using extended phase space to formally hide the time dependence. When the Hamiltonian $H(t)$ is a function of time, formally consider time t as a degree of freedom. There are now $n+1$ position variables, $q_1, q_2, \ldots, q_n, t$. Define the extended Hamiltonian $\bar{H}(q, p, t, -E) := H(q, p, t) - E$. The extended Hamiltonian is explicitly time-independent, since the "time" here is a new variable denoted τ. The equations of motion for the four independent variables $(q, p, t, -E)$

are

$$\dot{q} = \frac{\partial \bar{H}}{\partial p} = \frac{\partial H}{\partial p} \qquad \dot{t} = \frac{\partial \bar{H}}{\partial(-E)} = 1$$
$$\dot{p} = -\frac{\partial \bar{H}}{\partial q} = -\frac{\partial H}{\partial q} \qquad -\dot{E} = -\frac{\partial \bar{H}}{\partial t} = -\frac{\partial H}{\partial t}$$

with "dot" now meaning total derivative with respect to τ. Now a proper formal solution is $z(\tau) = \exp(\tau D_{\bar{H}})z(0)$, with Liouvillian

$$D_{\bar{H}} = \frac{\partial H}{\partial p}\frac{\partial}{\partial q} - \frac{\partial H}{\partial q}\frac{\partial H}{\partial p} + \frac{\partial}{\partial t} - \frac{\partial H}{\partial t}\frac{\partial}{\partial(-E)}.$$

Now form the second-order symplectic integrator for this Liouvillian. Defining shorthand as $D_{\bar{H}} =: A + B + C + D$, note that the time-independent second-order formula (C.5) can be applied stepwise:

$$\begin{aligned}
D_{\bar{H}}(\tau) &= \mathrm{e}^{\tau(A+B+C+D)} \\
D_{\bar{H},2}(\tau) &= \mathrm{e}^{\tau D/2}\mathrm{e}^{\tau(A+B+C)}\mathrm{e}^{\tau D/2} + O(\tau^3) \\
&= \mathrm{e}^{\tau D/2}\left(\mathrm{e}^{\tau C/2}\mathrm{e}^{\tau(A+B)}\mathrm{e}^{\tau C/2}\right)\mathrm{e}^{\tau D/2} + O(\tau^3) \\
&= \mathrm{e}^{\tau D/2}\left(\mathrm{e}^{\tau C/2}\mathrm{e}^{\tau(A+B)}\mathrm{e}^{\tau C/2}\right)\mathrm{e}^{\tau D/2} + O(\tau^3) \\
&= \mathrm{e}^{\tau D/2}\mathrm{e}^{\tau C/2}\mathrm{e}^{\tau B/2}\mathrm{e}^{\tau A}\mathrm{e}^{\tau B/2}\mathrm{e}^{\tau C/2}\mathrm{e}^{\tau D/2} + O(\tau^3).
\end{aligned}$$

Note that the D factors only propagate the momentum $-E$, which is uncoupled from the equations of motion for q, p, t. Thus the D factors can be ignored without affecting the "important" variables. Also, the C factors have such a simple associated equation, $\dot{t} = 1$, they only increase the time τ by $\tau/2$ before the remaining propagators are applied. Thus the only new feature of time-dependent SI2, relative to time-independent SI2, is to use the Hamiltonian matrix at one-half greater time increment when applying the A and B propagators that increase position and momentum. The underlying computer code is almost the same!

C.6 Sudden Approximation for a Short Laser Pulse

The time dependent Schrödinger equation has a formal solution for time independent Hamiltonian $\hat{H}$:

$$|\psi(t)\rangle = \exp\left(\frac{\mathrm{i}}{\hbar}\int^{t} \hat{H}\,\mathrm{d}t\right)|\psi(0)\rangle\,.$$

Substituting a time-dependent Hamiltonian is a good approximation when the time dependence is very rapid, for then the Hamiltonian is time-independent most of the time! In Section 3.3, I modeled linear rotors in pulsed laser fields using the polarizability interaction governed by a gaussian pulse envelope. The Hamiltonian in dimensionless time $\tau = B\hbar t$ is

$$\hat{h}(\tau) = \boldsymbol{j}^2 - \Delta\omega \mathrm{e}^{-\tau^2/\sigma^2}\cos^2\theta$$

with corresponding approximate propagator

$$\exp\left(-\mathrm{i}\int^{\tau} \hat{h}(\tau')\,\mathrm{d}\tau'\right).$$

If the time τ is well after the short pulse has gone by, then the standard gaussian integral formula can be used leaving the approximate propagated state

$$|\psi(\tau)\rangle = \exp\left(-\mathrm{i}\tau\boldsymbol{j}^2 + \mathrm{i}\Delta\omega\sigma\sqrt{\pi}\cos^2\theta\right)|\psi(0)\rangle\,.$$

Generally, the time-evolved state can be written as a spherical harmonic superposition, with time dependent coefficients and phase factors rotating at the field-free frequencies:

$$|\psi(\tau)\rangle = \sum_{JM} c_{JM}(\tau)\mathrm{e}^{-\mathrm{i}\tau J(J+1)}\,|JM\rangle\,.$$

These two expressions equated, using the isotropic $J = M = 0$ spherical harmonic as the ground state, and "splitting" the Hamiltonian (a simple approximation),

yield a useful formula for the superposition coefficients in time:

$$\sum_{JM} c_{JM}(\tau) \mathrm{e}^{-\mathrm{i}\tau J(J+1)} \, |JM\rangle = \mathrm{e}^{-\mathrm{i}\tau \boldsymbol{j}^2} \, \mathrm{e}^{\mathrm{i}\Delta\omega\sigma\sqrt{\pi}\cos^2\theta} \, |00\rangle$$

$$c_{JM}(\tau) \mathrm{e}^{-\mathrm{i}\tau J(J+1)} = \left\langle JM \left| \mathrm{e}^{-\mathrm{i}\tau \boldsymbol{j}^2} \, \mathrm{e}^{\mathrm{i}\Delta\omega\sigma\sqrt{\pi}\cos^2\theta} \right| 00 \right\rangle$$

$$c_{JM}(\tau) = \left\langle JM \left| \mathrm{e}^{\mathrm{i}\Delta\omega\sigma\sqrt{\pi}\cos^2\theta} \right| 00 \right\rangle .$$

The final field-free probabilities are thus determined, and they are constant post-pulse since the Hamiltonian is then constant with time.

The indicated integral is difficult to calculate analytically[†] but *Mathematica* makes short work of it for particular J, M values. Results are shown in Figure 3.4.

[†]In other related cases, the intergral reduces nicely. Persico and Van Leuven [52] use the sudden approximation for a dipole that follows the laser field oscillation (we modelled that this action was quenched by rapid oscillation). Arango [17] uses the same short laser pulse-polarizability interaction but for a rotor confined to a circle, using a plane wave basis. In each of these cases, a simple formula involving Bessel functions results, which is apparently unachievable here.

REFERENCES

[1] D. R. Lide, editor. *CRC Handbook of Chemistry and Physics*. CRC Press LLC, Boca Raton, Florida, 82nd edition, 2001.

[2] C. H. Townes and A. L. Schawlow. *Microwave Spectroscopy*. Dover Publications, Inc., New York, 1975.

[3] J. O. Hirschfelder, C. F. Curtiss, and R. B. Bird. *Molecular Theory of Gases and Liquids*. John Wiley & Sons, Inc., New York, 1954.

[4] B. Friedrich and D. Herschbach. Manipulating molecules via combined static and laser fields. *J. Phys. Chem. A*, 103:10280–10288, 1999.

[5] M. D. Poulsen, E. Péronne, H. Stapelfeldt, C. Z. Bisgaard, S. S. Viftrup, E. Hamilton, and T. Seideman. Nonadiabatic alignment of asymmetric top molecules: Rotational revivals. *J. Chem. Phys.*, 121(2):783–791, 2004.

[6] H. Li, K. J. Franks, R. J. Hanson, and W. Kong. Brute force orientation and alignment of pyridazine probed by resonantly enhanced multiphoton ionization. *J. Phys. Chem. A*, 102:8084–8090, 1998.

[7] H. W. Kroto. *Molecular Rotation Spectra*. Dover Publications, Inc., New York, 1992.

[8] D. Herschbach. Chemical physics: Molecular clouds, clusters, and corrals. *Rev. Mod. Phys.*, 71(2):S411–S418, 1999.

[9] H. J. Loesch and A. Remscheid. Brute force in molecular reaction dynamics: A novel technique for measuring steric effects. *J. Chem. Phys.*, 93(7):4779–4790, 1990.

[10] B. Friedrich and D. R. Herschbach. On the possibility of orienting rotationally cooled polar molecules in an electric field. *Z. Phys. D—Atoms, Molecules, and Clusters*, 18:153–161, 1991.

[11] B. Friedrich and D. Herschbach. Alignment and trapping of molecules in intense laser fields. *Phys. Rev. Lett.*, 74(23):4623–4626.

[12] H. Stapelfeldt and T. Seideman. *Colloquium*: Aligning molecules with strong laser pulses. *Rev. Mod. Phys.*, 75(2):543–557, 2003.

[13] S. Minemoto, H. Nanjo, H. Tanji, T. Suzuki, and H. Sakai. Observation of molecular orientation by the combination of electrostatic and nonresonant, pulsed laser fields. *J. Chem. Phys.*, 118(9):4052–4059, 2003.

[14] R. N. Zare. *Angular Momentum*. Wiley-Interscience, New York, 1988.

[15] M. P. Bogaard and B. J. Orr. Electric dipole polarisabilities of atoms and molecules. In A. D. Buckingham, editor, *MTP International Review of Science: Physical Chemistry: Molecular Structure and Properties*, volume 2 of *2*, pages 149–194. Butterworths, London, 1975.

[16] D. M. Brink and G. R. Satchler. *Angular Momentum*. Clarendon Press, Oxford, third edition, 1993.

[17] C. A. Arango. *Classical and Semiclassical Mechanics of Molecular Rotors in Tilted Fields*. PhD thesis, Cornell University, 2005.

[18] G. Arfken. *Mathematical Methods for Physicists*. Academic Press, New York, second edition, 1970.

[19] M. V. Berry and M. Wilkinson. Diabolical points in the spectra of triangles. *Proc. R. Soc. Lond. A*, 392:15–43, 1984.

[20] R. P. Feynman. Forces in molecules. *Phys. Rev.*, 56:340–343, 1939.

[21] J. Ortigoso, M. Rodríguez, M. Gupta, and B. Friedrich. Time evolution of pendular states created by the interaction of molecular polarizability with a pulsed nonresonant laser field. *J. Chem. Phys.*, 110(8):3870–3875, 1999.

[22] B. Hayes. The spectrum of riemannium. *American Scientist*, 91(4):296–300, 2003.

[23] F. Haake. *Quantum Signatures of Chaos*. Springer-Verlag, 1991.

[24] M. C. Gutzwiller. *Chaos in Classical and Quantum Mechanics*. Springer-Verlag, New York, 1990.

[25] C. A. Arango, W. W. Kennerly, and G. S. Ezra. Classical and quantum mechanics of diatomic molecules in tilted fields. *J. Chem. Phys.*, 122:184303, 2005.

[26] O. Bohigas and M. J. Giannoni. Chaotic motion and random matrix theories. In J. S. Dehesa *et. al.*, editor, *Mathematical and Computational Methods in Nuclear Physics*, volume 209 of *Lecture Notes in Physics*, pages 1–99. Springer-Verlag, 1984.

[27] E. P. Wigner. Results and theory of resonance absorption. ORNL-2309 reprinted in [30], pp. 199–211, November 1956.

[28] E. P. Wigner. Random matrices in physics. *SIAM Review*, 9(1):1–23, 1967.

[29] C. Schlier. How much can we learn from nearest neighbor distributions? *J. Chem. Phys.*, 117(7):3098–3102, 2002.

[30] C. E. Porter, editor. *Statistical Theories of Spectra: Fluctuations*. Academic Press, 1965.

[31] I. C. Percival. Regular and irregular spectra. *J. Phys. B: Atom. Molec. Phys.*, 6:L229–L232, 1973.

[32] M. V. Berry and M. Tabor. Level clustering in the regular spectrum. *Proc. R. Soc. Lond. A*, 356:375–394, 1977.

[33] O. Bohigas, M. J. Giannoni, and C. Schmit. Characterization of chaotic quantum spectra and universality of level fluctuation laws. *Phys. Rev. Lett.*, 52:1–4, 1984.

[34] M. V. Berry and M. Robnik. Semiclassical level spacings when regular and chaotic orbits coexist. *J. Phys. A: Math. Gen.*, 17:2413–2421, 1984.

[35] T. A. Brody, J. Flores, J. B. French, P. A. Mello, A. Pandey, and S. S. M. Wong. Random-matrix physics: spectrum and strength fluctuations. *Rev. Mod. Phys.*, 53:385–479, 1981.

[36] D. Wintgen and H. Friedrich. Classical and quantum-mechanical transition between regularity and irregularity in a hamiltonian system. *Phys. Rev. A*, 35(3):1464–1466, 1987.

[37] J. Main, M. Schwacke, and G. Wunner. Hydrogen atom in combined electric and magnetic fields with arbitrary mutual orientations. *Phys. Rev. A*, 57(2):1149–1157, 1998.

[38] T. P. Grozdanov and R. McCarroll. Level statistics for asymmetric-top rotors in strong electric fields. *Z. Phys. D*, 38:45–49, 1996.

[39] V. R. Manfredi and L. Salasnich. Pathological behavior in the spectral statistics of the asymmetric rotor model. *Phys. Rev. E*, 64:066201, 2001.

[40] V. R. Manfredi, V. Penna, and L. Salasnich. Spectral statistics of the triaxial rigid rotator: Semiclassical origin of their pathological behavior. *Mod. Phys. Lett. B*, 17(15):803–812, 2003.

[41] D. Marchesan, G. Moruzzi, and N. Rahman. Quantum chaotic behavior in vibro-roto-torsional levels of methanol and its isotopomers. *Chem. Phys. Lett.*, 381:556–564, 2003.

[42] H. Wu, M. Valliéres, D. H. Feng, and D. W. L. Sprung. Gaussian-orthogonal-ensemble level statistics in a one-dimensional system. *Phys. Rev. A*, 42(3):1027–1032, 1990.

[43] C. A. Arango, W. W. Kennerly, and G. S. Ezra. Quantum monodromy for diatomic molecules in combined electrostatic and pulsed nonresonant laser fields. *Chem. Phys. Lett.*, 392:486–492, 2004.

[44] J. A. Morales, E. Deumens, and Y. Öhrn. On rotational coherent states in molecular quantum dynamics. *J. Math. Phys.*, 40(2):766–786, 1999.

[45] J. G. Underwood, B. J. Sussman, and A. Stolow. Field-free three dimensional molecular axis alignment. *Phys. Rev. Lett.*, 94:143002, 2005.

[46] W. H. Press, S. A. Teukolsky, W. T. Vetterling, and B. P. Flannery. *Numerical Recipes in C: The Art of Scientific Computing*. Cambridge University Press, Cambridge, UK, second edition, 1992.

[47] S. K. Gray and J. M. Verosky. Classical hamiltonian structures in wave packet dynamics. *J. Chem. Phys.*, 100(7):5011–5022, 1994.

[48] H. Goldstein. *Classical Mechanics*. Addison-Wesley Publishing Company, Inc., Cambridge, Mass., first edition, 1950.

[49] M. Tuckerman, B. J. Berne, and G. J. Martyna. Reversible multiple time scale molecular dynamics. *J. Chem. Phys.*, 97(3):1990–2001, 1992.

[50] H. Yoshida. Construction of higher order symplectic integrators. *Phys. Lett. A*, 150(5,6,7):262–268, 1990.

[51] J. M. Sanz-Serna and A. Portillo. Classical numerical integrators for wave-packet dynamics. *J. Chem. Phys.*, 104(6):2349–2355, 1995.

[52] M. Persico and P. Van Leuven. Short-time quantum dynamics of the driven rigid rotor. *Z. Phys. D*, 41:139–141, 1997.